Sharpening the IPCC conclusions into New Climate Change Scenarios for The Netherlands

Bart van den Hurk, Albert Klein Tank, Geert Lenderink, Aad van Ulden, Geert Jan van Oldenborgh, Caroline Katsman, Henk van den Brink, Franziska Keller, Janette Bessembinder, Gerrit Burgers, Gerbrand Komen, Wilco Hazeleger and Sybren Drijfhout

Introduction

The recently presented Fourth Assessment Report (AR4) from Working Group I of the Intergovernmental Panel on Climate Change (IPCC) has been received with great interest by stakeholders in many sectors of modern society where climate change may have serious consequences. One means of dealing with the inevitable uncertainty of future climate is by constructing a suite of different discrete climate change scenarios. The present paper describes how a new set of four scenarios for The Netherlands has recently been developed, representative for the local climate conditions around the years 2050 and 2100. The method combines a range of global and regional climate model simulations and local observations in order to optimally span the major sources of climate variability and uncertainty in the region of interest. Although no explicit likelihood is assigned to any of the scenarios, the set of four enables a meaningful assessment of the impact of climate change on many sectors of society. They provide considerable additional detail to the general IPCC conclusions for the region of interest.

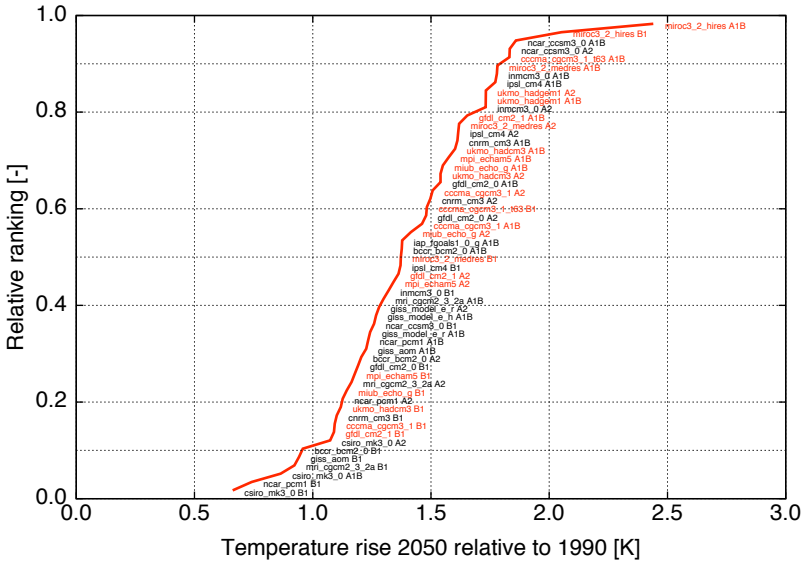

Figure 1. Cumulative frequency distribution of the model-predicted global temperature rise between 1990 and 2050 of all available GCM projections used for AR4, driven by the SRES B1, A1B and A2 emission scenarios.

A modelling chain to construct regional scenarios

In most cases regional climate scenarios are constructed from projections from a limited set of Global Climate Models (GCMS), driven by a few greenhouse gas emission scenarios, and statistically or dynamically downscaled to increase the information content at the regional scale[1,2].

The climate change scenarios for The Netherlands are constructed differently from this general approach [3]. A combination of GCM projections, Regional Climate Model (RCM) results and local observations is used, and a sophisticated set of external scaling factors is derived to cover a major portion of climate variability in the region of interest. Apart from the global mean temperature rise (ΔT_g) the (uncertain) response of the regional atmospheric circulation to global temperature change appeared to be an important external indicator.

A large number of GCM projections has been made available by the Program for Climate Model Diagnosis and Intercomparison (PCMDI) during the preparation of AR4. The (political and socio-economical) relevance of scenarios covering the full range of global temperature rise (+1.1 to +6.4°C in 2100, according to the Summary for Policy Makers (SPM)[4] is not uniform across this range. Limitation in available adaptation resources, political will and persistence of existing policy generally exclude a serious consideration of very extreme scenarios with a relatively low probability. Scenarios are developed for two values of ΔT_g in 2050 relative to 1990 (being +1 and +2 °C), which optimizes a sufficiently wide range with only a few outlying GCM projections (see Figure 1) and is consistent with previous scenarios[5]. Up to 2050, differences in GCM projections of ΔT_g are mainly associated with uncertainty about the climate sensitivity, and less with variations between greenhouse gas (GHG) emission scenarios.

In West Central Europe, variations in the frequency distribution of the seasonal mean atmospheric circulation patterns explain a major part of the variability of the seasonal mean temperature[6]. Systematic

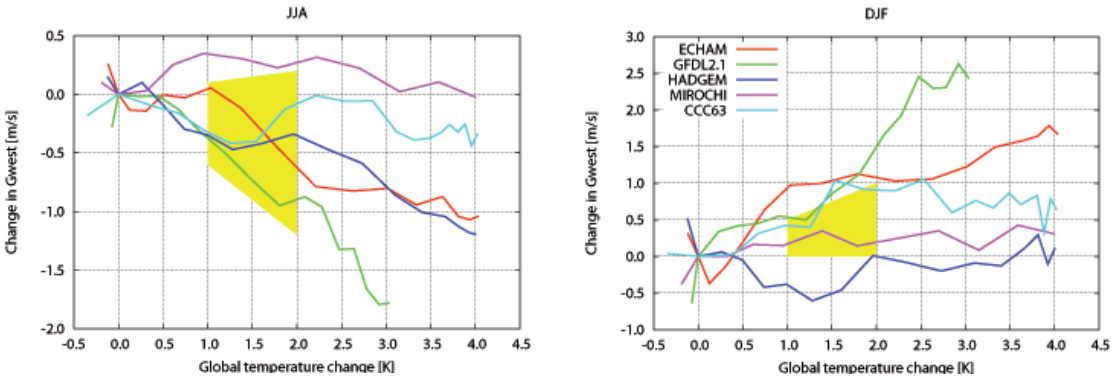

Figure 2. Change in mean westward geostrophic flow GW as function of the simultaneous change in global temperature (ΔT_g) for the five GCMs considered for (left) JJA and (right) DJF. Shown are transient A1b emission scenario simulations between 2000 and 2100. The coloured shapes span the scenario values of ΔG_w and ΔT_g.

Systematic changes in circulation, for instance, impact strongly on the likelihood of extreme dry summer conditions

changes in circulation, for instance, impact strongly on the likelihood of extreme dry summer conditions[7]. Many state-of-the-art GCMS have systematic biases in the frequency distribution of the seasonal mean westward geostrophic flow (G_w)[8]. It is highly questionable whether GCMS with a strong circulation bias over West Central Europe are able to adequately represent the circulation response to global warming. Therefore, the climate change scenarios for The Netherlands are based on a selection of GCMS that most accurately represent the present day circulation on the Northern Hemisphere. Five models passed the selection criteria (ECHAM5, HadGEM1, CGCM3.1, MIROCHI, and GFDL2.1).

The response of the regional circulation to global warming varies widely across the five selected GCMS. MIROCHI forms an example of the GCMS that show only a marginal change of the circulation statistics in both summer and winter, whereas GFDL2.1 represents a regime with a strong increase in the seasonal mean westward geostrophic flow G_w in winter and a decrease in summer (Figure 2). The local effects on precipitation and temperature induced by gradients in land-sea, topography, clouds, snow, soil moisture and vegetation are not represented well in GCMS. Also extreme events are generally not reproduced in the course resolution GCM grid size. In an ensemble of 10 selected RCM runs from the EU 5th Framework Programme PRUDENCE project[9] the desired scenario range (ΔT_g of +1 and +2°C in 2050, small or large change of ΔG_w) was not well covered[10]. In particular, projections with a small change in circulation over Western Europe were not at all present in the collection of simulations due to the limited number of driving GCMS. To extrapolate the results from the available RCM integrations to the global temperature and circulation conditions covered by the scenarios, a two-variable scaling equation was designed by Van Ulden and Van Oldenborgh[8] and Lenderink et al.[11]. The values of ΔG_w in each scenario and season (shown by the coloured shapes in Figure 2) are chosen such that the range of seasonal mean precipitation projected by the GCM ensemble is well covered by the scenarios (Figure 3). The same set of ΔT_g and ΔG_w values are used to generate all temperature and precipitation variables.

Sea level rise projections

In the SPM sea level rise (SLR) projections for 2100 are composed of a quantified contribution from thermal expansion and decreased land ice storage (in a range between 0.18 and 0.59 m), and an extra SLR associated with changes in ice cap dynamics which are too uncertain to be quantified. Like the IPCC assessment, the SLR scenarios for The Netherlands are based on the AR4 GCM archive[12]. The global mean SLR contribution from thermal expansion is derived from the AR4 GCM ensemble using a linear regression plus uncertainty bands on projected ΔT_g. However, a number of additional SLR terms are quantified.

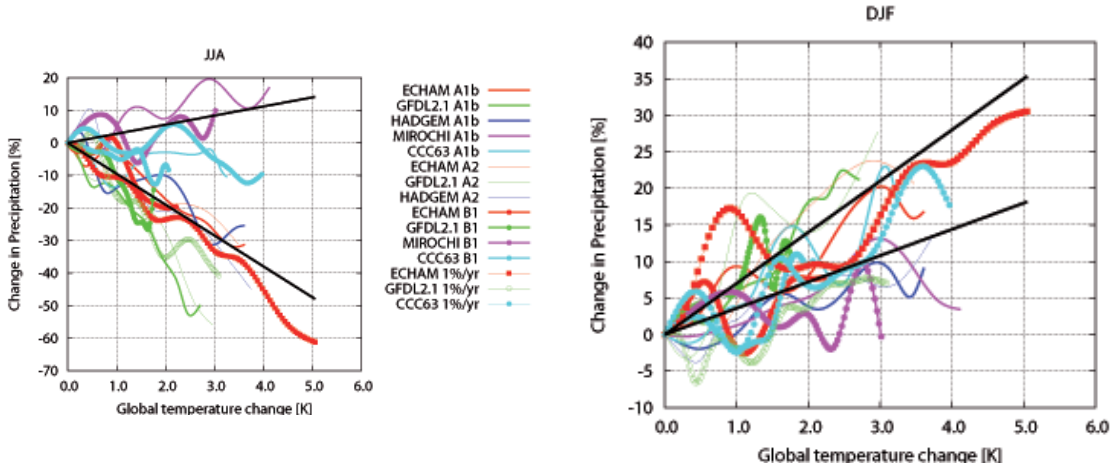

Figure 3. Smoothed projected change of seasonal mean precipitation for (left) JJA and (right) DJF in The Netherlands as function of global mean temperature rise, as simulated for the period 1990-2200 by a selection of AR4 GCM simulations. The black solid lines indicate the scaling relationships used for the two circulation regimes in the scenarios.

The impact of a relatively fast response of ice sheets to large rises in atmospheric temperature is used to determine the upper bound of the contribution to sea level rise

First, SLR in the eastern North Atlantic basin is projected to be larger than the global mean by most model simulations, which probably is a response to a weakening of the thermohaline circulation[13]. This difference and its uncertainty are assessed by assuming a linear dependence on ΔT_g, based on 25 quality-checked GCM simulations for which local data were available.

Second, a contribution of the Greenland and Antarctic ice sheets (including small glaciers and ice caps around their edges) to SLR is quantified using both model results and recent observations. Estimates of the observed present-day melt rate[14] are combined with observed and modelled dependence of the mass loss on global mean atmospheric temperature. For Antarctica, modelled[15] and observed[16] trends in mass losses are of opposite sign. Therefore the climate sensitivity of this ice sheet is assumed to be zero. For Greenland a positive relation between net mass loss and temperature is adopted. In addition, the impact of a relatively fast response of ice sheets to large rises in atmospheric temperature[17] is used to determine the upper bound of the contribution to sea level rise. As a result, the upper uncertainty band is about 4 times larger than the lower uncertainty band.

Scenarios of the wind regime

In line with the IPCC assessment, projected changes in the wind regime in the region of interest are very uncertain. Although many model projections agree in some aspects (such as the poleward shift of the storm track[18]), they differ with respect to changes of the strength and number of extra-tropical cyclones[19 vs 20]. In The Netherlands there is a need for scenarios for wind speed extremes with a very long return period (10,000 yrs), for coastal defence strategic planning. These extremes cannot be derived from the available GCM results without considerable statistical extrapolation. Instead, changes in 'moderate' wind extremes (daily mean wind exceeded once per year) are derived from the AR4 GCM archive. As for the temperature and precipitation scenarios, two regimes of circulation change are discerned, but additional downscaling with RCMs did not prove to add significant information on the variable of interest. The projected changes are small in comparison with the natural variability of the extreme wind speed.

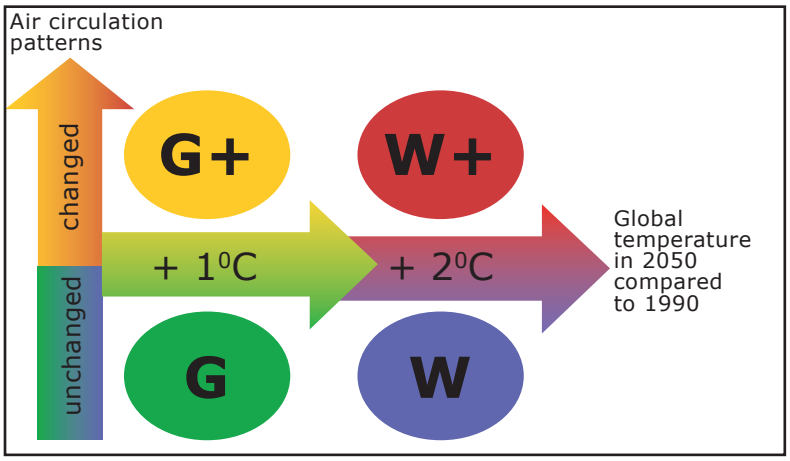

G	Moderate*	1°C temperature rise on earth in 2050 compared to 1990 no change in air circulation patterns in Western Europe
G+	Moderate +	1°C temperature rise on earth in 2050 compared to 1990 + milder and wetter winters due to more westerly winds + warmer and drier summers due to more easterly winds
W	Warm	2°C temperature rise on earth in 2050 compared to 1990 no change in air circulation patterns in Western Europe
W+	Warm +	2°C temperature rise on earth in 2050 compared to 1990 + milder and wetter winters due to more westerly winds + warmer and drier summers due to more easterly winds

Figure 4. Schematic overview of the four KNMI'06 climate scenarios. For explanation see the legend below.

		G	G+	W	W+
Global temperature rise		+1°C	+1°C	+2°C	+2°C
Change in air circulation patterns		no	yes	no	yes
Winter [3]	average temperature	+0.9°C	+1.1°C	+1.8°C	+2.3°C
	coldest winter day per year	+1.0°C	+1.5°C	+2.1°C	+2.9°C
	average precipitation amount	+4%	+7%	+7%	+14%
	number of wet days (≥ 0.1 mm)	0%	+1%	0%	+2%
	10-day precipitation sum exceeded once in 10 years	+4%	+6%	+8%	+12%
	maximum average daily wind speed per year	0%	+2%	-1%	+4%
Summer [3]	average temperature	+0.9°C	+1.4°C	+1.7°C	+2.8°C
	warmest summer day per year	+1.0°C	+1.9°C	+2.1°C	+3.8°C
	average precipitation amount	+3%	-10%	+6%	-19%
	number of wet days (≥ 0.1 mm)	-2%	-10%	-3%	-19%
	daily precipitation sum exceeded once in 10 years	+13%	+5%	+27%	+10%
	potential evaporation	+3%	+8%	+7%	+15%

Table 1. KNMI'06 scenarios for 2050.
See www.knmi.nl/climatescenarios for more details.

Conclusion

The results of the 4 scenarios are presented in Table 1. An overview of the scenario structure is given in Figure 4.

The construction of the scenarios is carried out by a considerable selection, weighing, scaling and grouping of GCM results to sharpen the broad IPCC assessment into a set of relevant, plausible and internally consistent climate change scenarios for The Netherlands. Uncertainties regarding emission scenarios, lack of understanding of the climate system, internal climate variability, and regional detail all have been included in the scenarios. Yet, a future generation of climate change scenarios may possibly be very different from the present set, since a great deal of known and (yet) unknown uncertainties (like major feedback processes involving the carbon cycle, dynamic vegetation and ice cap dynamics) are still not fully captured in the GCM results.

1) MPI-M, 2006. *Klimaprojektionen für das 21. Jahrhundert.* MPI-Report, 28 pp. available from www.mpimet.mpg.de.
2) Giorgi F., 2005. *Climate Change Prediction.* Climatic Change, **73**, 239-265.
3) Van den Hurk and 13 co-authors, 2006. *KNMI Climate Change scenarios for 2006.* KNMI Scientific Report WR 2006-01, 82 pp. available from www.knmi.nl/climatescenarios.
4) IPCC, 2007. *Climate Change 2007: The physical basis. Summary for Policy Makers.* see http://www.ipcc.ch.
5) Kors, A.G., F.A.M. Claessen, J.W. Wesseling and G.P. Können, 2000. *Scenario's externe krachten voor WB21.* WL|Delft Hydraulics; Koninklijk Nederlands Meteorologisch Instituut (KNMI) ; Ministerie van Verkeer en Waterstaat, Rijkswaterstaat, Rijksinstituut voor Integraal Zoetwaterbeheer en Afvalwaterbehandeling (RWS, RIZA) (in Dutch).
6) Oldenborgh, G.J. van and A. van Ulden, 2003. *On the relationship between global warming, local warming in The Netherlands and changes in circulation in the 20th century.* Int. J. Climatology, **23**, 1711-1723, doi:10.1002/joc.966
7) Black, E., M. Blackburn, G. Harrison, B. Hoskins and J. Methven, 2004. *Factors contributing to the summer 2003 heat wave.* Weather, **59**, 217-223.
8) Ulden, A.P. van and G.J. van Oldenborgh, 2006. *Large-scale atmospheric circulation biases and changes in global climate model simulations and their importance for climate change in Central Europe.* Atm. Chem. Phys., **6**, 863-881. www.atmos-chem-phys.net/6/863/2006/.
9) Christensen, J.H., T. Carter and F. Giorgi, 2002. *PRUDENCE employs new methods to assess European climate change.* EOS, **83**, 147.
10) Déqué, M., D.P. Rowell, D. Lüthi, F. Giorgi, J.H. Christensen, B. Rockel, D. Jacob, E. Kjellström, M. de Castro and B. van den Hurk, 2006. *An intercomparison of regional climate simulations for Europe: assessing uncertainties in model projections.* Climatic Change, in press.
11) Lenderink, G., A. van Ulden, B. van den Hurk, F. Keller and G-J van Oldenborgh, 2006. *The construction of regional climate scenarios for The Netherlands: a study on combining global and regional climate model results.* Clim. Dyn., in press.
12) Katsman, C., W. Hazeleger, S. Drijfhout, G.J. van Oldenborgh and G. Burgers, 2006. *Climate scenarios of sea level rise for the northeast Atlantic Ocean: a study on combining observations and model results.* Submitted to Climatic Change.
13) Gregory, J.M. and 17 co-authors, 2005. *A model intercomparison of changes in the Atlantic thermohaline circulation in response to increasing atmospheric CO_2 concentration.* Geophys. Res. Lett., **32**, L12703, doi:10.1029/2005GL023209
14) Rignot, E. and P. Kanagaratnam, 2006. *Changes in the Velocity Structure of the Greenland Ice Sheet.* Science, **311**, 986-990.
15) Gregory, J.M. and P. Huybrechts, 2006. *Ice sheet contributions to future sea-level change.* Phil. Trans. R. Soc. A, in press.
16) Monaghan A.J. and 15 co-authors, 2006. *Insignificant Change in Antarctic Snowfall Since the International Geophysical Year.* Science, **313,** 5788, 827-831. doi: 10.1126/science.1128243
17) Ridley, J.K. et al., 2005. *Elimination of the Greenland ice sheet in a high CO_2 climate.* J. Clim., **17**, 3409-3427.
18) Yin, J.H., 2005. *A consistent poleward shift of the storm tracks in simulations of 21st century climate.* Geophys. Res. Lett., **32**, L18701. doi:10.1029/2005GL023684
19) Lambert, S. and J.C. Fyfe, 2006. *Changes in winter cyclone frequencies and strengths simulated in enhanced greenhouse gas experiments: Results from the models participating in the IPCC diagnostic exercise.* Clim. Dyn., doi:10.1007/s00382-006-0110-3.
20) Bengtsson, L.B., K.I. Hodges and E. Roeckner, 2006. *Storm tracks and climate change.* J. Clim., **19**, 15, 3518-3543. doi:10.1175/JCLI3815.1

The Baseline Surface Radiation Network (BSRN) station at the Cabauw observatory

Wouter Knap, Jan Bijma, Yvonne Hinssen, Alexander Los, Cor van Oort, Jacques Warmer and Ed Worrell

Introduction

Radiation is the primary energy source and the ultimate energy sink for the Earth's climate system. Most climate changes are directly or indirectly related to changes in radiation. It is therefore not an overstatement to say that understanding of the climate system begins with the understanding of radiation and its interactions with the atmospheric constituents such as clouds, aerosols, and greenhouse gases. Because of the important role of radiation in the climate system, radiation measurements are indispensable for climate research. They provide the best check for the theory of radiative transfer in the Earth's atmosphere and can be used for the evaluation and improvement of models designed for weather and climate prediction. Furthermore, long-term measurements of surface radiation provide an opportunity for the detection of climate change.

The importance of accurate and precise radiation measurements for climate research was the primary reason for the joint scientific committee of the World Climate Research Programme (WCRP) to establish in 1988 the international Baseline Surface Radiation Network (BSRN)[1]. The goal was to establish a world-wide network of radiation measurements adhering to the highest achievable standards. Currently there are 39 fully operational and 8 candidate stations (Figure 1).

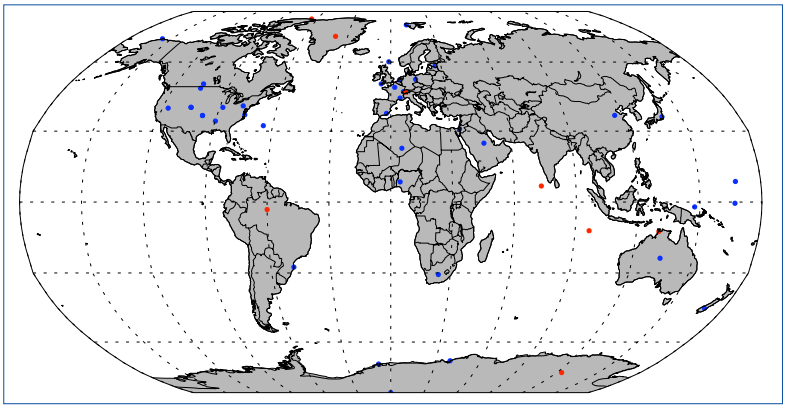

Figure 1. Global map of all stations of the Baseline Surface Radiation Network (BSRN). The blue dots indicate fully operational stations (39) whereas the red dots indicate candidate stations (8) (situation: August 2006). KNMI participates in BSRN with the radiation station at the Cabauw observatory (51.97°N, 4.93°E).

In 2004 BSRN was designated as the global baseline network for surface radiation for the Global Climate Observing System (GCOS; http://www.wmo.ch/web/gcos).

The idea for KNMI to join BSRN existed in the early 1990s but it was not until 2001 that the necessity for accurate and precise radiation measurements became urgent. A radiative closure study[2] revealed that the radiation measurements were not accurate enough to draw firm conclusions on the significance of differences between model calculations and measurements of surface radiation. After an exploratory visit to the BSRN station of Payerne, Switzerland, in 2002 it was decided to initiate the construction of a radiation site in Cabauw according to the BSRN requirements.
The organization of this chapter is as follows. First, the BSRN station in Cabauw is described in terms of instruments and measured quantities. Also, an example of measurement quality control is given. Then it is shown how the calibration of the solar radiation measurements in Cabauw is linked to the world standard of irradiance. In the following two sections, two applications of the BSRN measurements in Cabauw are presented. The first is an evaluation of different methods for the determination of sunshine duration. The Cabauw measurements allowed for a thorough evaluation of a method that is used for nation-wide estimates of sunshine duration from global radiation. The second application deals with the effect of aerosols on solar radiation in relation to the origin of the air masses arriving in the measurement area. An outlook for the future is given in the last section.

BSRN Cabauw

The field constructions for the BSRN station in Cabauw were completed by the end of 2004 (Figure 2). The data acquisition system, designed to meet the stringent BSRN requirements, and a basic set of radiation instruments were operational by early 2005. The first consistent monthly dataset of basic radiation measurements (global, direct, diffuse and downward longwave radiation) was obtained in February 2005. Since then, the station has been extended with various spectral radiation measurements (both direct

Figure 2. Photographs showing the BSRN station and the 200 m tower in Cabauw. The basic radiation measurements consist of global, direct, diffuse and downward longwave radiation. In addition, various spectral solar radiation measurements are made. Images of the sky are made using a Total Sky Imager. Photographs taken by W.H. Knap, January 2005.

and diffuse) made at different solar wavelengths. A total sky imager has been installed as well as instruments for measuring ultraviolet and photosynthetically active radiation and sunshine duration. The formal status of Cabauw as BSRN station was announced at the 9th BSRN Workshop and Scientific Review in Lindenberg, Germany, May 2006[3].

Besides the installation of constructions and instruments, considerable effort has been put into the implementation of quality control procedures and the development of a web-based system for the access to quick looks and measurements. Some of the applied quality control procedures involve the use of radiative transfer models. An example for a selection of downward longwave irradiances measured at BSRN Cabauw is shown in Figure 3. The same quantity was calculated using the radiative transfer model MODTRAN 4. The bias of 7 ± 4 W m^{-2} between model and measurements is considered to be acceptable and gives confidence in the measurements and excludes serious instrument malfunction.

International Pyrheliometer Comparison

The World Radiometric Reference[4] is the measurement standard representing the SI unit of irradiance (W m^{-2}). The WRR is realized by measurements of direct solar radiation made by a group of 15 absolute cavity radiometers – the World Standard Group (WSG) – which is situated at the Physikalisch-Meteorologisches Observatorium Davos/World Radiation Center (PMOD/WRC) in Davos, Switzerland. The WRR has been introduced to ensure worldwide homogeneity of solar radiation measurements and is in use by the meteorological community since 1981. The reference has an estimated accuracy of 0.3% and guarantees that worldwide solar radiation measurements are precise within 0.1%[4]. The dissemination of the WRR

Figure 3. Scatterplot of modelled and measured clear-sky downward longwave radiation for BSRN Cabauw. The modelled values were calculated with the radiative transfer model MODTRAN (version 4). The model underestimates the measurements by an acceptable 7 ± 4 W m^{-2}.

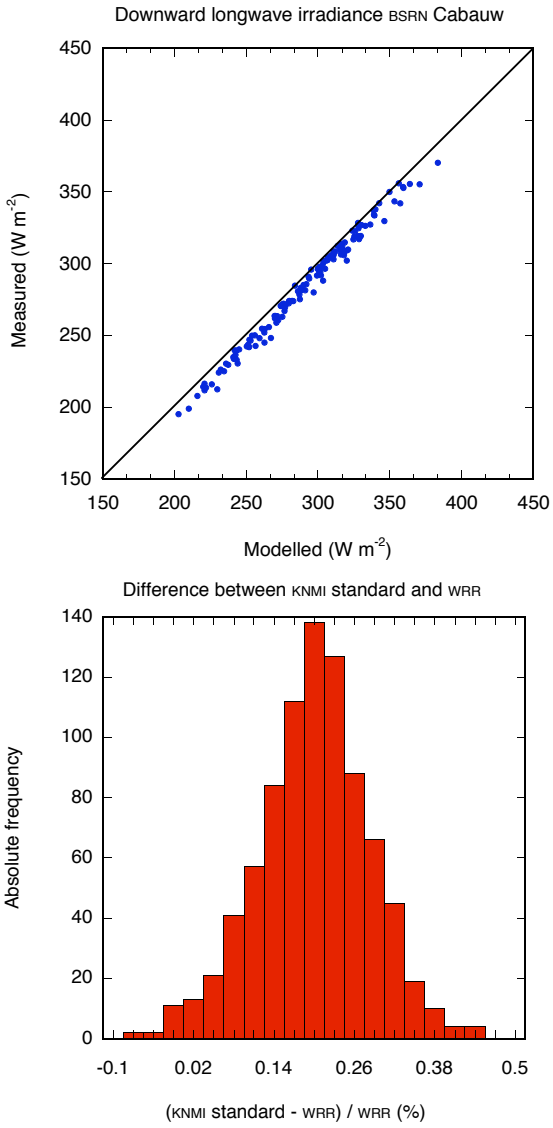

Figure 4. Left panel: KNMI instruments for the measurement of direct solar radiation present during the 10th International Pyrheliometer Comparison, Davos, Switzerland, autumn 2005. Right panel: histogram of the relative difference between the KNMI measurement standard for direct solar radiation (Eppley HF cavity radiometer) and the World Radiometric Reference (WRR).

Because of the important role of radiation in the climate system, radiation measurements are indispensable for climate research.

is realized by direct intercomparisons between pyrheliometer measurements and the WRR during the International Pyrheliometer Comparison (IPC) which is held at PMOD/WRC every five years. For BSRN stations, representing the highest standard of radiation measurements, it is essential to participate in IPCS so as to guarantee direct traceability of solar radiation measurements to the WRR.

From 26 September until 14 October 2005 KNMI participated in the 10th International Pyrheliometer Comparison (IPC-X), Davos, Switzerland[5]. It was the third time that KNMI was present in Davos; in 1990 and 1995 KNMI participated in the 7th and 8th IPC. Each time, KNMI used the same Eppley Hickey–Frieden (HF) cavity radiometer (Figure 4, left panel), which is one of the most accurate instruments for measuring direct solar irradiance. The 10th IPC was characterised by favourable weather conditions that resulted in a record number of calibration measurements. Figure 4 (right panel) shows the performance of the KNMI instrument relative to the WRR. On average the difference appeared to be as small as 0.20 ± 0.08%. The excellent agreement with the WRR will allow us to perform on site calibrations of the solar radiation instruments of the BSRN site in Cabauw, that are directly traceable to the WRR.

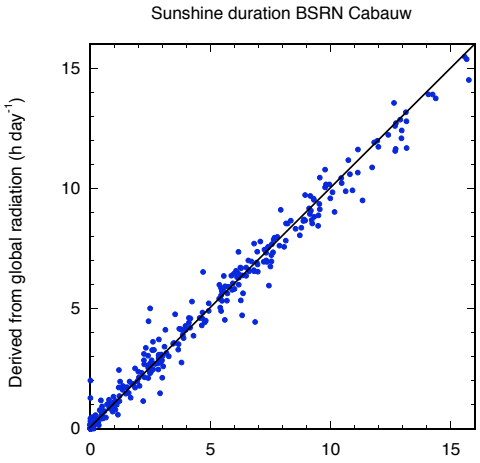

Figure 5. Scatterplot of daily sunshine durations for 2005 (in h day^{-1}) derived from measurements of global radiation (vertical axis) and direct solar radiation (horizontal axis) made at BSRN Cabauw. The first are estimates of sunshine duration based on a simple correlation algorithm and the second are values based on the WMO definition of sunshine duration.

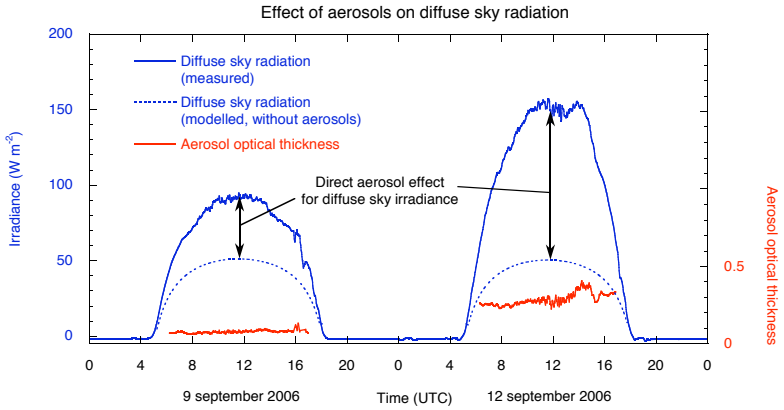

Figure 6. Measurements of diffuse sky radiation and aerosol optical thickness made at BSRN Cabauw on 9 and 12 September. Also shown are radiative transfer calculations for Rayleigh atmospheres with added water vapour. The arrows indicate the direct aerosol effect for diffuse sky irradiance.

The large variations in aerosol optical thickness that are observed in Cabauw can largely be understood by considering the origin of the air masses arriving in the measurement area

Sunshine duration

One of the first applications of the radiation measurements made in Cabauw was a detailed evaluation of different methods for the determination of sunshine duration from measurements of global radiation[6,7]. The rationale for the evaluation is the fact that sunshine duration is often estimated from global radiation instead of direct radiation because instruments for measuring direct radiation are expensive. The true sunshine duration was derived by application of the formal WMO definition of sunshine duration, which states that 'the sun shines' when the direct solar irradiance exceeds 120 W m^{-2}. The evaluation showed that relatively accurate estimates of daily sunshine duration can be made from 10-min mean observations of global irradiance, using simple correlation techniques (Figure 5). The uncertainties for daily and yearly sums appear to be typically 0.5 h day^{-1} and 0.5%, respectively.

Slob and Monna[8] developed a more complicated method for the determination of sunshine duration from global radiation, which relies on parameterized estimates of direct and diffuse radiation. An adjusted version of the method has been operational since 1992 for nation-wide estimates of sunshine duration[9]. Application of the method allows KNMI to continue the historical record of sunshine duration (dating back to 1901) as determined with the Campbell-Stokes sunshine recorder. Using the BSRN measurements for Cabauw, Hinssen and Knap[6,7] showed that the method is potentially accurate but requires extensive tuning of model parameters. They also showed that the operational algorithm significantly overestimates the sunshine duration; the cumulative number of sunshine hours for 2005 appears to be 13% too high. This is caused by the fact that the operational method is tuned to the traditional way of determining sunshine duration, which is based on the use of the Campbell-Stokes sunshine recorder (a glass sphere that burns a trace in a paper card). This instrument tends to overestimate the sunshine duration, especially during broken-cloud conditions. Hinssen[6] gives recommendations on how to improve the operational sunshine duration product.

The effect of aerosols on solar radiation

The BSRN radiation measurements made in Cabauw, together with other measurements made within the framework of the Cabauw Experimental Site for Atmospheric Research (CESAR; http://www.cesar-observatory.nl) allow us to perform detailed studies of the interaction between clouds, aerosols, and radiation. An example of the effect of aerosols on the diffuse sky radiation is shown in Figure 6, which contains cloudless measurements made in 2006 on a day with low aerosol load (9 September) and a day with high aerosol load (12 September). The aerosol optical thickness (AOT) at 500 nm, measured with the SPUV sunphotometer[10,11], ranges from 0.06 on the first day to 0.41 on the second day, which largely spans the spectrum of AOT values occurring in the Netherlands. At noon, the diffuse sky radiation on 12 September (high AOT) is about 60 W m^{-2} higher than on 9 September (low AOT), which is caused by enhanced scattering of sunlight by aerosols. Since aerosols scatter visible sunlight without a clear preference for a certain wavelength, the human eye observes this increase in diffuse sky radiation as a change in sky colour; from deep blue to whitish.

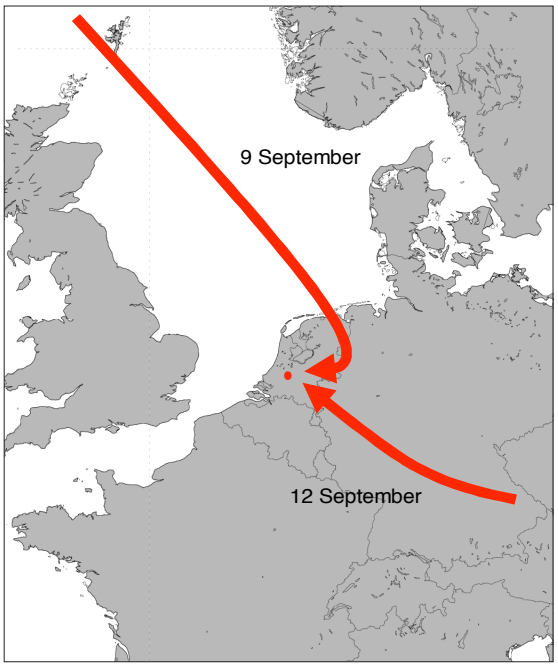

Figure 7. Schematic representation of the origin of air masses arriving in the Cabauw area on 9 and 12 September 2006, derived from trajectory analysis. The period between these days represents a transition from low to high aerosol loads.

To further analyse the relation between aerosols and radiation, radiative transfer calculations were made for a Rayleigh atmosphere (containing only the permanent atmospheric gases) with added water vapour (dotted lines in Figure 6). By substracting these calculations from the measurements of diffuse sky radiation, one is left with the direct aerosol effect for the diffuse sky radiation. On the two days mentioned above the effect appears to be at noon 40 W m^{-2} (low AOT) and as much as 100 W m^{-2} (high AOT).
The large variations in aerosol optical thickness that are observed in Cabauw can largely be understood by considering the origin of the air masses arriving in the measurement area. For 9 and 12 September, the large-scale flow was identified using a trajectory model (Figure 7). It appears that the air arriving in the Cabauw area on 9 September has travelled mainly over the Atlantic Ocean and the North Sea where several natural and most anthropogenic sources of aerosol are absent. The situation for 12 September is very different: the air was advected over land, in particular over industrialized regions in Germany, where major sources of atmospheric pollution are present. These, in combination with natural sources of aerosol, give rise to the observed high values of AOT.

Outlook

Long-term monitoring of the solar and infrared radiation components with high accuracy and precision is an indispensable activity for the climate research community. The BSRN station of Cabauw will therefore continue to be operational as the reference radiation monitoring station for the Netherlands and will make its contribution to the global network of surface radiation measurements. The station will be extended with downward facing instruments for the measurement of upward shortwave and longwave radiation. Together with the downward radiation components this addition will complete the surface radiation budget, which is one of the GCOS Essential Climate Variables.

The combination of BSRN and CESAR, the national observatory for atmospheric research, gives a unique opportunity for high-level scientific research that aims at an improved understanding of the interaction between clouds, aerosols and radiation. The construction of time series, for example of the effect of aerosols on radiation, will be an integral part of future research. These time series, which are in itself valuable for the detection of possible trends, will also be used for the evaluation of models such as KNMI's regional atmospheric model, RACMO.

Acknowledgements
We are indebted to late Wim Hovius for his contributions during the early stages of the project. We thank our colleagues of the Instrumental Department (INSA) of KNMI for their support with the construction and maintenance of the BSRN station in Cabauw. In particular we mention Bob van den Berg, Rob Cornet, and Jan-Willem Schoonderwoerd. We thank Rinus Scheele for providing us with the trajectory analyses.

1) Ohmura A. and 14 co-authors, 1998. *Baseline Surface Radiation Network (BSRN/WCRP), a new precision radiometry for climate research.* Bull. Amer. Meteor. Soc., **79**, 2115 - 2136.
2) Henzing, J.S., W.H. Knap, P. Stammes, H.M. ten Brink, G.P.A. Kos, D.P.J. Swart, A. Apituley and J.B. Bergwerff, 2004. *Effect of aerosols on the downward shortwave irradiances at the surface: measurements versus calculations with MODTRAN4.1.* J. Geophys. Res., **109**, D14204. doi:10.1029/2003JD004142
3) WCRP, 2007. *Summary report from the 9th session of the Baseline Surface Radiation Network (BSRN),* Lindenberg, Germany, 29 May – 2 June 2006. WCRP informal report No 1/2007, 54 pp.
4) Fröhlich, C. 1991. *History of Solar Radiometry and the World Radiometric Reference.* Metrologia, **28**, 111–115.
5) Finsterle, W., 2006. *WMO International Pyrheliometer Comparison IPC-X,* 26 September – 14 October 2005, Davos, Switzerland. IOM Report No. 91, WMO/TD No. 1320, 65 pp.
6) Hinssen, Y.B.L., 2006. *Comparison of different methods for the determination of sunshine duration.* KNMI Scientific Report WR-2006-06, 72 pp.
7) Hinssen, Y.B.L. and W.H. Knap, 2007. *Comparison of pyranometric and pyrheliometric methods for the determination of sunshine duration.* J. Atm. Oceanic Technol., **24**, 835–846. doi: 10.1175/JTECH2013.1
8) Slob, W.H. and W.A.A. Monna, 1991. *Bepaling van directe en diffuse straling en van zonneschijnduur uit 10-minuutwaarden van de globale straling.* KNMI Technical Report TR–136, 31 pp.
9) Bergman, U., 1993. *Het programma voor berekening van zonneschijnduur uit globale straling.* KNMI Techical Report TR–158, 16 pp.
10) Stammes, P. and J.S. Henzing, 2000. *Multispectral aerosol optical thickness at De Bilt, 1997-1999.* J. Aerosol Sci., **31**, 283–284.
11) Knap, W.H., A. Los, E. Worrell and P. Stammes. 2003. *Sunphotometry at the High Altitude Research Station Jungfraujoch.* Activity Report 2003 of the International Foundation HFSJG, 91–95.

Wind observations with Doppler weather radar

Iwan Holleman

Introduction

Weather radars are commonly employed for detection and ranging of precipitation, but radars with Doppler capability can also provide detailed information on the wind associated with (severe) weather phenomena. The Royal Netherlands Meteorological Institute (KNMI) operates two identical C-band (5.6 GHz) Doppler weather radars. One radar is located in De Bilt and the other one is located in Den Helder. Two distinctly different pulse repetition frequencies are used to extend the unambiguous velocity interval of the Doppler radars from 13 to 40 m/s[1]. In this chapter, the retrieval and quality of weather radar wind profiles are discussed. In addition the extraction of temperature advection from these profiles is presented. Finally the detection of severe weather phenomena and monitoring of bird migration for aviation are highlighted.

Retrieval of radar wind profiles

A Doppler weather radar measures the scattering from atmospheric targets, like rain, snow, dust, and insects. The radar provides the mean radial velocity as a function of range, azimuth, and elevation. Assuming a uniform wind field (u_o,v_o,w_o) and a constant fall velocity, the radial velocity V_r can be modelled as a function of the azimuth φ and the elevation θ:

$$V_r(\varphi,\theta) = u_o \cos\theta \sin\varphi + v_o \cos\theta \cos\varphi + w'_o \sin\theta \quad (1)$$

where w'_o is the sum of the vertical wind speed and the terminal fall velocity of the hydrometeors. When Doppler data are displayed at constant range and elevation, the radial velocity as a function of azimuth will resemble a sine (see Figure 1). The wind speed and direction can be determined from the amplitude and the phase of the sine, respectively. This well-known technique is called Velocity Azimuth Display (VAD)[2].

Instead of processing multiple VADs and averaging the results, one can also process all available radial velocity data within a certain height layer at once. The parameters of the wind field can then be extracted using a multi-dimensional and multi-parameter linear fit. This so-called Volume Velocity Processing technique (VVP) has been introduced by Waldteufel and Corbin in 1979[3]. At KNMI the VVP technique is used for the operational production of weather radar wind profiles with a 200 m height resolution[4].

Figure 1 shows two examples of VAD data from the operational weather radar in De Bilt. The huge difference in scatter of the observed radial velocity data around the modelled radial velocities is evident (the origin is discussed below). The amount of scatter can be quantified using the standard deviation of the radial velocity (SDRV):

$$SDRV^2 = \Sigma_{i=1}^{N} [V_{r,i}-V_r(\varphi_i,\theta_i)]^2 / (N-3) \quad (2)$$

where $V_{r,i}$ are the observed radial velocities and N is the number of data points. Quality control on the wind data is performed by rejecting all vectors with a SDRV above 2.0 m/s.

Verification of radar wind profiles

An intercomparison of different implementations of the VAD and VVP windprofile retrieval methods using radiosonde profiles as a reference revealed that the VVP method performs slightly better than the VAD method[4]. Furthermore it was found that the simplest implementation of the VVP retrieval method, i.e.,

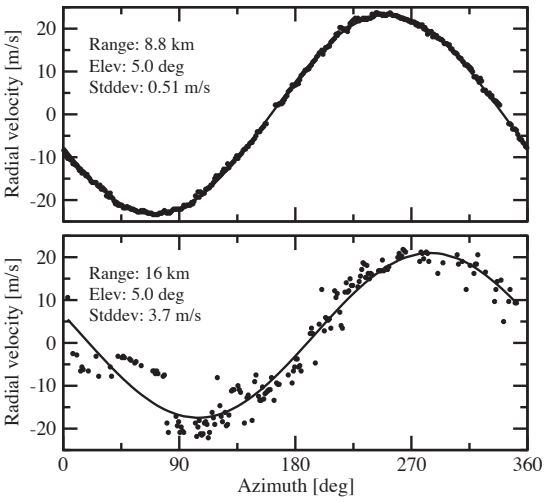

Figure 1. Two examples of Velocity Azimuth Display (VAD) data from the operational weather radar in De Bilt are shown. The upper frame displays a VAD during the passage of a cold front (1409 UTC on 8 March 2003) and the lower frame during intense bird migration (0009 UTC on 7 March 2003).

using the uniform wind field, provides the best horizontal wind data.

Figure 2 shows the statistics of the VVP (upper frames) and radiosonde (lower frames) wind profile observations against the HIRLAM NWP background. The bias and standard deviation of the Cartesian u- and v-components of the wind vectors are calculated for a 9 months verification period. In this comparison the radiosonde has a clear advantage over weather radar because the radiosonde profiles are assimilated by the HIRLAM model. For the radar wind data, a small positive bias for both Cartesian components is seen.

Quality differences between the weather radar (VVP) and radiosonde observations can be assessed by investigating the standard deviation of the observations against the HIRLAM background. The standard deviation of the radiosonde wind vector components is between 1.5 and 2.0 m/s at ground level and gradually increases to almost 3.0 m/s aloft. This increase is probably due to the increase of the wind speeds with height and to horizontal drifting of the radiosonde. The standard deviation of the VVP wind vector components against the HIRLAM background is around 2.0 m/s at ground level and only 2.5 m/s aloft. Figure 2 shows that observation minus background statistics of the weather radar wind profiles are at least as good as those of the radiosonde profiles. This result clearly demonstrates the high quality of the weather radar wind profiles.

Temperature advection from thermal wind

Figure 3 shows a time-height plot of the weather radar and HIRLAM wind profiles during the passage of a cold front. Evidently the agreement between the radar and model wind vectors is good, but the update frequency and availability differ. The vertical shear in the wind profiles can be highlighted by deducing the temperature advection using the thermal wind. The thermal wind (u_T, v_T), which is basically the vertical shear of the (geostrophic) wind, is given by:

$$v_T = -R/f\ (\partial T/\partial x)_p\ \ln(p_2/p_1) \qquad (3)$$

where R and f are the ideal gas constant and the Coriolis parameter, p_1 and p_2 are the air pressures at the bottom and top of the height layer. A similar equation is valid for u_T. Assuming hydrostatic balance one can calculate the temperature gradients from the vertical wind shear:

$$\partial T/\partial x = +f/g\ (v_2-v_1)/(z_2-z_1)\ T((z_1+z_2)/2) \qquad (4)$$
$$\partial T/\partial y = -f/g\ (u_2-u_1)/(z_2-z_1)\ T((z_1+z_2)/2) \qquad (5)$$

This result clearly demonstrates the high quality of the weather radar wind profiles.

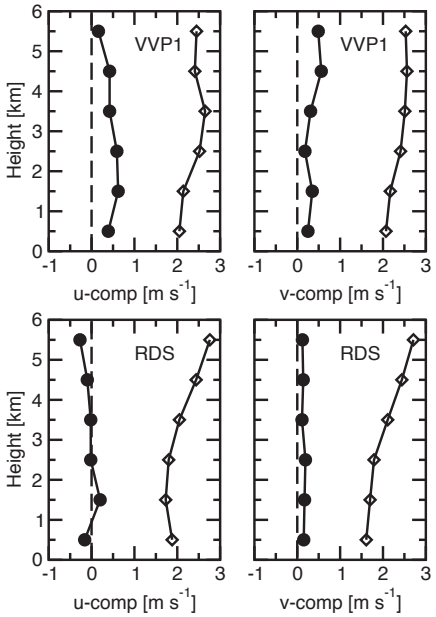

Figure 2. Profiles of the bias (●) and standard deviation (◇) of the Cartesian u- and v-components from the verification of the radar (upper) and radiosonde (lower) wind data against the HIRLAM NWP model.

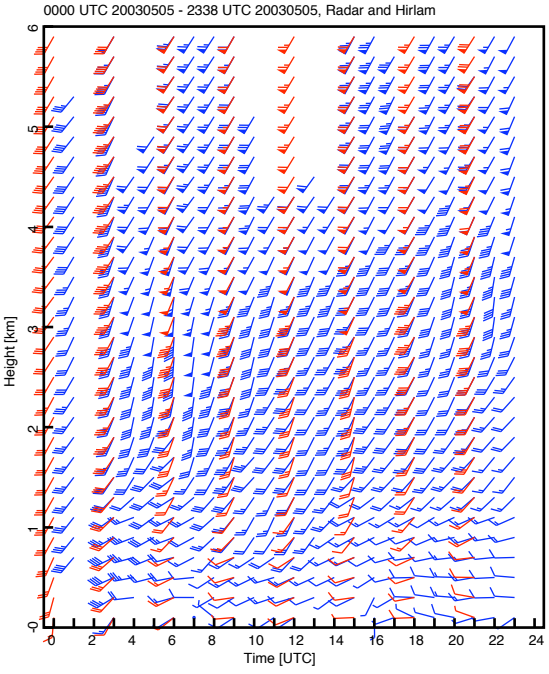

Figure 3. A time-height plot with the weather radar wind profiles (blue barbs) for 5 May 2003. The wind profiles from the HIRLAM NWP model are overlaid in red. Wind speed and direction are indicated by wind vanes. Each full barb represents a wind speed of 5 m/s and each triangle a wind speed of 25 m/s.

where g is the gravitational constant and the temperature T(z) is approximated by the International Standard Atmosphere (ISA). Thus the temperature advection is obtained from:

$$\partial T/\partial t = -(u\,\partial T/\partial x + v\,\partial T/\partial y) \qquad (6)$$

The temperature advection has been calculated from the wind profiles in Figure 3 and the result is shown in Figure 4. Cold air advection (blue) is seen below 3 km and warm air advection (red) is found above. This can be explained by the cold front arching backward. Because the front is moving slowly, the cold advection does not penetrate heights above 3 km, something that would normally occur if the front was moving faster[5].

The temperature advection is retrieved using the geostrophic approximation which is questionable for mesoscale phenomena. Nevertheless, displaying the temperature advection emphasizes the rotation and vertical shear in the wind field, which would probably stay unnoticed otherwise.

Mesocyclones detected with horizontal wind shear

Mesoscale severe weather phenomena like gust fronts, microbursts, and mesocylcones, are usually associated with small-scale deviations in the local wind field. These small-scale deviations can be accentuated by calculation of the horizontal shear (HZS). The horizontal shear is a combination of the so-called radial shear (RS) and the azimuthal shear (AS). The radial shear is calculated by differencing the observed Doppler velocities at different ranges from the radar while the azimuth shear is calculated from different azimuths [6]. The horizontal shear is then calculated from:

$$HZS = \sqrt{RS^2 + AS^2} \qquad (7)$$

Values above 8 m s^{-1} km^{-1} indicate severe and/or dangerous shear zones.

On 23 August 2004 a cold front passed over the Netherlands from southwest to northeast and around 15 UTC a supercell thunderstorm developed on this front. Around 16 UTC the supercell produced a tornado near Muiden. Figure 5 shows the damage inflicted on an old barn in Muiden. The supercell thunderstorm has been observed by the Doppler weather radar in De Bilt at a range of about 30 km. Part (a) of Figure 6 shows the high-resolution radar reflectivity recorded at 1612 UTC and is zoomed in around Muiden. The supercell thunderstorm is clearly visible and a large band of extremely strong reflectivities (>55 dBZ ≈ 100 mm/h) is seen. The hook echo, one of the most important signatures of a supercell, is located over Muiden.

Part (b) of Figure 6 shows the horizontal wind shear product corresponding to the high-resolution reflectivity product of part (a). Around the hook echo of the super cell, a region with strong horizontal wind shear (>15 m s^{-1} km^{-1}) reflecting the mesocyclone of the supercell is evident. So the Doppler radar detected the mesocyclone associated with the tornado in Muiden. It is stressed that a Doppler weather radar cannot detect a tornado directly because it is too small and too close to the earth's surface.

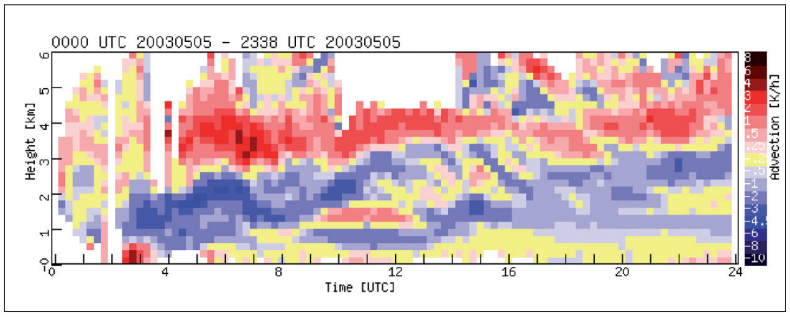

Figure 4. Time-height plot of temperature advection calculated from radar wind profile data of 5 May 2003 (see Figure 3). Red indicates advection of warm air and blue of cold air.

Figure 5. Damage of a (old) barn due to the tornado in Muiden on 23 August 2004 (photo by R. Sluijter).

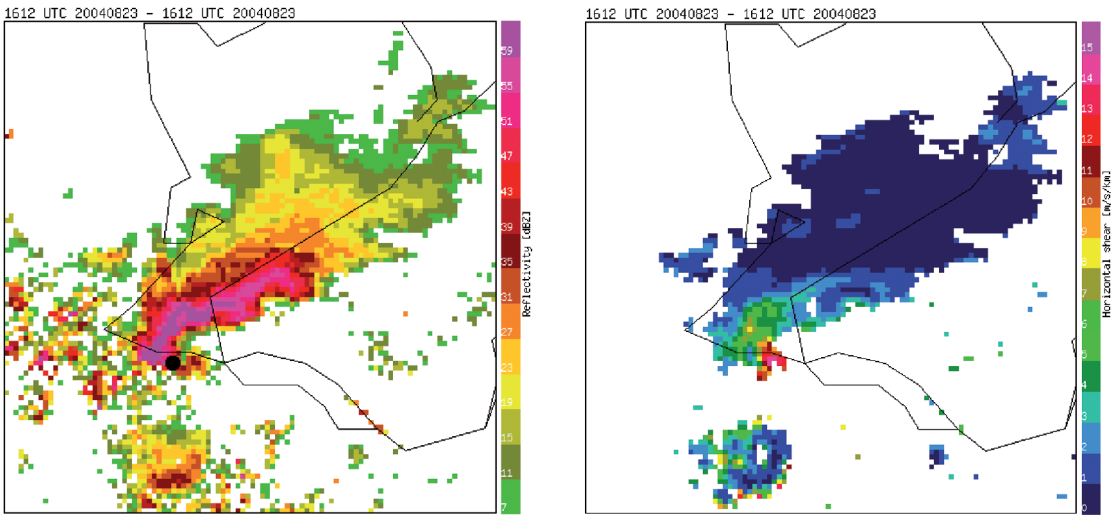

Figure 6. Part (a) shows a high-resolution (0.5 km) reflectivity product recorded by the Doppler radar in De Bilt at 0.3 deg elevation and zoomed around the supercell (1612 UTC on 23 August 2004) over Muiden (marked by black dot, west of Amsterdam). Part (b) shows the corresponding horizontal windshear product.

Monitoring of bird migration

Migrating birds are a potential hazard for aircraft during take-off, landing, and low-level flights. The impact of a crash of a crane with a military helicopter flying at 300 meter altitude in Israel is shown in Figure 7. Furthermore migrating birds can cause severe errors in the wind speed (up to 20 m/s!) and direction retrieved from a Doppler radar.

Figure 1 shows two examples of VAD data from the radar in De Bilt. The upper frame displays a high-quality 'wind' VAD during the passage of a cold front while the lower frame shows a VAD during intense bird migration. The huge difference in scatter of the observed radial velocity data around the modelled radial velocities is evident. The amount of scatter can be quantified using the standard deviation of the radial velocity (SDRV). Observations from a mobile bird radar of the Royal Netherlands Air Force (RNLAF) have been used to validate the discrimination of winds and birds using SDRV. These data have been recorded during the spring of 2003 at air force base De Peel, about 80 km from the radar in De Bilt.

A scatter plot of the reflectivity versus SDRV for the radar wind vectors of De Bilt is shown in Figure 8. The magenta and blue bullets correspond to vectors classified by the mobile bird radar in De Peel as 'wind' and 'birds', respectively. The horizontal dashed line marks the default threshold used to quality control the wind vectors. The excellent separation between wind and birds is evident from the figure. The magenta bullets above the dashed line are mostly due to insects. It is straightforward to use this method for the rejection of bird contamination from wind profiles[7], and further development will improve the extraction of bird migration information[8].

Outlook

Due to the EUMETNET programme on operational exchange of weather radar data (OPERA) the availability of weather radar wind profiles in Europe has increased dramatically, and the format and quality of the exchanged data have been harmonized. Operational assimilation of the wind data from the European radar network in the HIRLAM model will be pursued. In 2007 the receivers, signal processors, and control systems of the KNMI weather radars will be modernized. This upgrade will enable higher update frequencies, higher spatial resolution, and new (Doppler) products.

Acknowledgments

Hans Beekhuis (KNMI) is gratefully acknowledged for his skilful technical assistance and good collaboration. The work on temperature advection from radar wind profiles has been performed by Susanne Jonker (WUR). Han Mellink (KNMI) helped with analysing the cases for the evaluation of the horizontal wind shear product. The collaboration with Hans van Gasteren (RNLAF) and Prof. Willem Bouten (UVA) on the bird migration research is highly appreciated.

Figure 7. A full hit of a crane on a military helicopter flying at 300 meter altitude in Israel. Cranes migrate in large numbers over Israel in March (photo obtained via RNLAF).

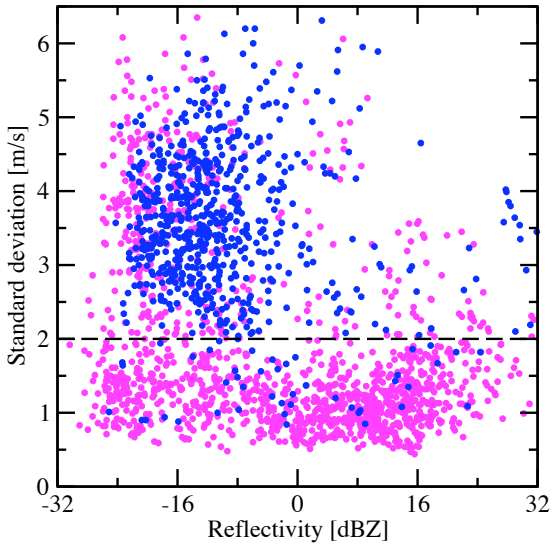

Figure 8. A scatter plot of the reflectivity versus the standard deviation of the radial velocity (SDRV) for the radar wind vectors. The magenta bullets and blue bullets correspond to vectors classified by the mobile bird radar as 'wind' and 'birds', respectively.

The Doppler radar detected the mesocyclone associated with the tornado in Muiden.

1) Holleman, I. and H. Beekhuis, 2003. *Analysis and correction of dual-PRF velocity data.* J. Atm. Oceanic. Technol., **20**, 443-453.

2) Browning, K. A. and R. Wexler, 1968. *The determination of kinematic properties of a wind field using Doppler radar.* J. Appl. Meteor., **7**,105-113.

3) Waldteufel, P. and H. Corbin, 1979. *On the analysis of single Doppler radar data.* J. Appl. Meteor., **18**, 532-542.

4) Holleman, I., 2005. *Quality control and verification of weather radar wind profiles.* J. Atm. Oceanic. Technol., **22**, 1541-1550.

5) Jonker, S., 2003. *Temperature advection derived from Doppler radar wind profiles.* KNMI Internal Report IR 2003-08.

6) Holleman, I., H. Mellink, T. de Boer and H. Beekhuis, 2005. *Evaluatie van Doppler windscheringproduct (in Dutch).* KNMI Internal Report IR 2005-01.

7) Holleman, I., H. van Gasteren and W. Bouten, 2007. *Quality Assessment of Weather Radar Wind Profiles during Bird Migration.* J. Atm. Oceanic. Technol., submitted.

8) Gasteren, H. van, I. Holleman, W. Bouten and E. van Loon, 2007. *Extracting bird migration information from C-band weather radars.* Ibis, submitted.

Mesoscale winds from the new ASCAT scatterometer

Ad Stoffelen, Marcos Portabella, Anton Verhoef, Jeroen Verspeek and Jur Vogelzang

Introduction

Satellite based scatterometers provide high resolution all-weather wind vector fields over the seas. Wind speed and wind direction are provided at high accuracy under all weather conditions. The all-weather ESA ERS scatterometer observations have proven its significant impact for the forecasting of fast developing and severe weather. Moreover, scatterometer wind fields are provided on the scale of ocean eddies. These wind fields are important for driving the ocean's motion. As a consequence, oceanographic applications and climate research have been initiated using winds from the SeaWinds scatterometer on the QuikScat satellite. The EUMETSAT Advanced Scatterometer ASCAT on MetOp-A was launched on 19 October 2006 as the third wind scatterometer in space joining up with the ESA ERS-2 and the NASA/NOAA SeaWinds scatterometers. Together, the ASCAT, ERS-2 and SeaWinds scatterometers provide good coverage over the oceans in the morning and evening (Local Solar Time). They are used routinely in marine and weather forecasting. The KNMI contribution to the EUMETSAT Satellite Application Facilities (SAFs), the ASCAT calibration, the production of high spatial resolution wind products at KNMI and their application are elaborated below. The KNMI global ocean wind product from the ASCAT scatterometer is the first routine MetOp-A geophysical product. During the coming years KNMI will continue to develop high resolution operational products for coastal areas.

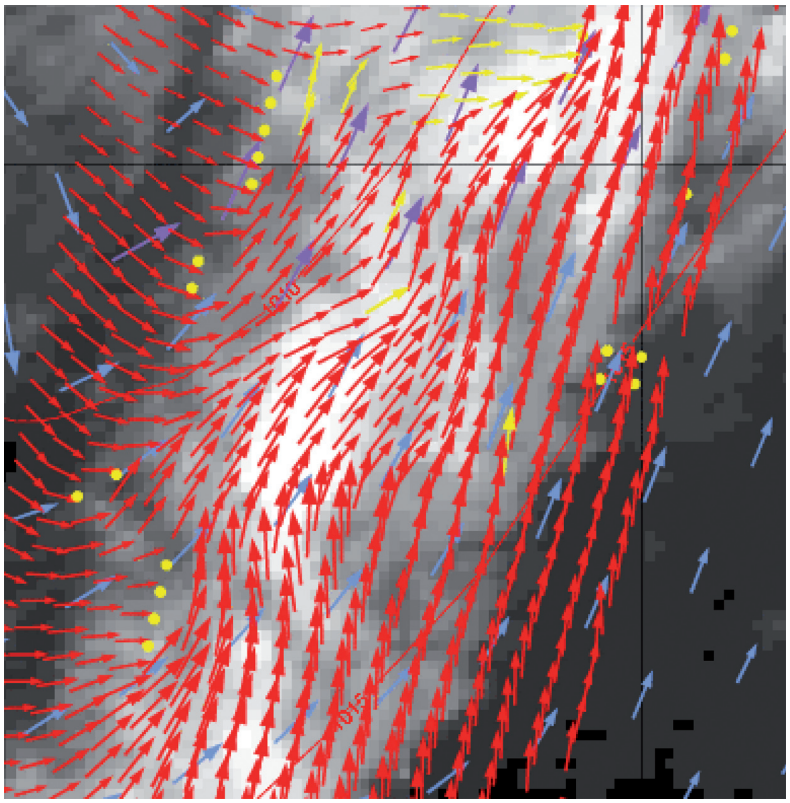

Figure 1. ERS-2 scatterometer winds (red) on 28 August 2006 13:00 UTC showing a train of atmospheric Rossby waves in the North Atlantic at 25W and 40N. The blue and purple arrows depict simultaneous NWP (HIRLAM) winds that generally do not resolve such weather phenomena. The METEOSAT InfraRed, IR, grey image in the background is consistent with the scatterometer surface winds. The Rossby train missed by NWP resulted in a bust precipitation forecast on 1 Sep 2006 in the Netherlands and England.

ASCAT winds

Scatterometers uniquely define the mesoscale wind vector field at the sea surface by measuring the radar backscatter signal from wind-generated cm-sized, so-called gravity-capillary sea waves. Because of the wavelength (5 cm), the signal of ASCAT is not affected by rain, and is therefore an 'all-weather' system. The all-weather capability of the ASCAT scatterometer provides unique wind field products of the most intense and often cloud-covered wind phenomena, such as polar front disturbances and tropical cyclones (for example, see Figure 1). As such, it has been demonstrated that scatterometer winds are extremely useful in the prediction of extra-tropical and tropical cyclones[1]. Moreover, high-resolution near-surface winds as provided by scatterometers are very relevant because these winds drive the ocean water circulation, which in turn plays a major role in the climate system and in marine life and its exploitation (e.g., fishery).

At the moment KNMI provides a regional quasi-real-time and a global near-real-time data stream for the ERS-2 and the SeaWinds scatterometer on QuikScat respectively. MetOp-A complements these global scatterometer missions with ASCAT. A regional quasi-real-time ASCAT dissemination and a near-real-time global service are being started at KNMI. In this way continuity of both wind services will be provided to the operational meteorological and oceanographic communities for another period of 15 years in the

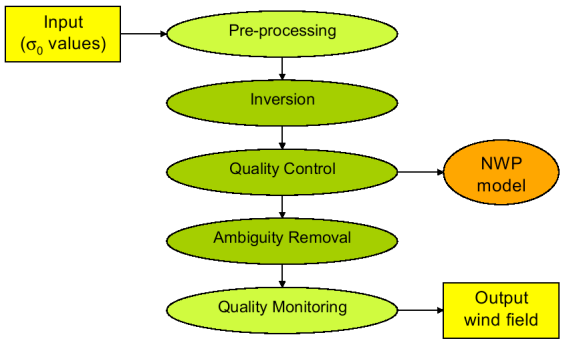

Figure 2. Overview of scatterometer wind processing. The scatterometer backscatter measurements, σ_0 values, are verified in the preprocessing, inverted to ambiguous wind solutions, spatially filtered in the ambiguity removal, checked on WVC level for internal consistency and nominal characteristics are monitored on wind product level.

MetOp era. China and India also plan to launch scatterometers this decade, but detailed information on the availability and processing of their winds has not yet been published.

The methodology developed for the successful application and assimilation of ERS winds in Numerical Weather Prediction (NWP) (see Figure 2) has been generalised at KNMI to include the new scatterometer concepts, such as SeaWinds and ASCAT. In the coming years, further progress in high resolution processing and with improved geophysical interpretation will be elaborated. Moreover, the current processing of scatterometer measurements does not allow winds in the coastal region due to land contamination. Studies are initiated to improve coastal scatterometer wind processing

ASCAT calibration

The geophysical knowledge of water-surface radar backscatter obtained from the ERS scatterometer observations in the radar C band is used in calibrating ASCAT. The empirical C-band Geophysical Model Function (GMF), called CMOD5[2], relates ERS scatterometer backscatter data to wind. Moreover, the geophysical uncertainties in the interpretation of scatterometer winds have been modelled in detail[3]. This provides insight in the coherence of the three scatterometer measurements, one by each of the three radar beams, in a Wind Vector Cell (WVC). In a first calibration step this coherence is predicted by CMOD5 and tested against the combined probability density function (PDF) of the ASCAT measurement data and its coherence (Figure 3). In a second step, a controlled distribution of backscatter measurements of ASCAT may be simulated by using a reference 10-m wind data set and CMOD5, and be compared to the

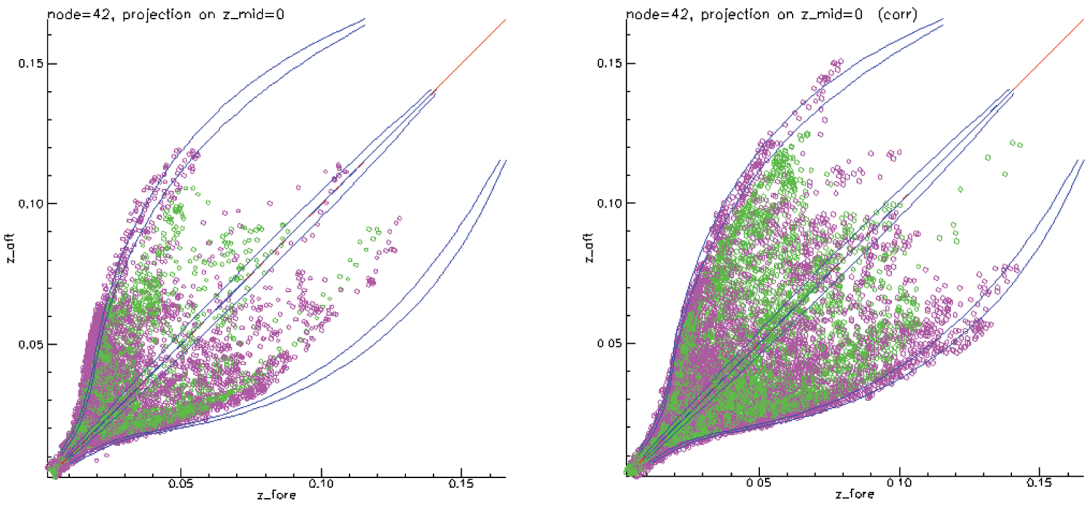

Figure 3. Expected and measured ASCAT scatterometer backscatter data at the WVC in the utmost outer right ASCAT swath. Symbols represent measured fore (horizontal axis) and aft look (vertical axis) backscatter values. ECMWF wind vectors are towards (purple) and away (green) from the mid beam pointing (look direction). The blue lines are for the CMOD5 GMF for wind directions with respect to the mid look of N•45 degrees for N = [0-8]. The left panel is for just after launch in 2006 and right, after the KNMI scaling correction[4].On the right, the wind direction outer lines of 45 and 315 degrees depict the outer purple points nicely.

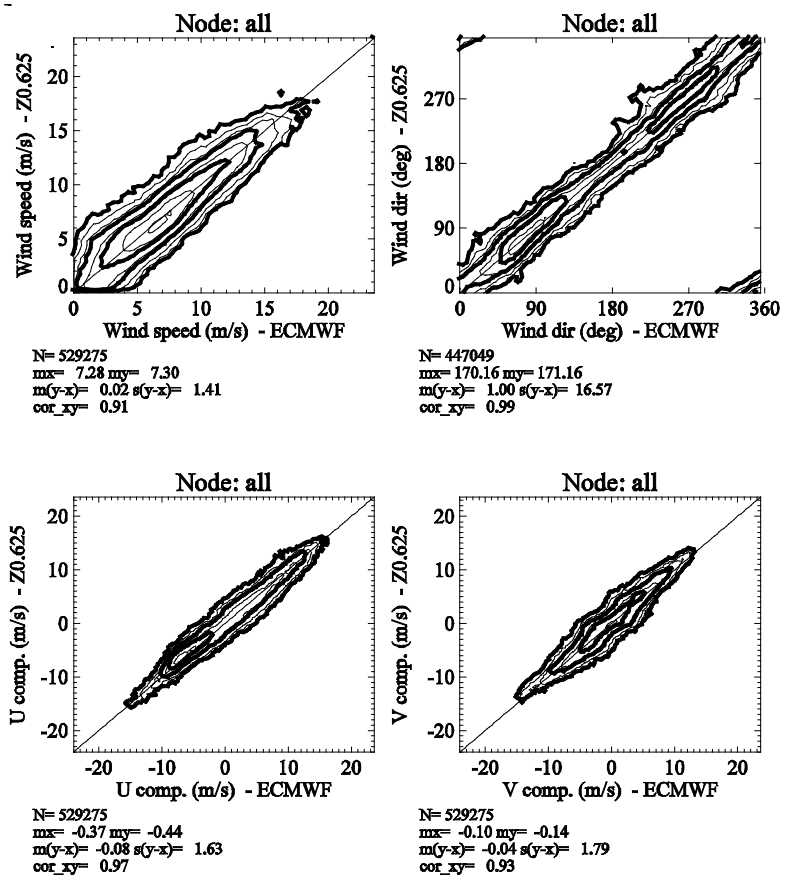

Figure 4. ASCAT winds computed after KNMI scaling corrections on the vertical axis and ECMWF winds on the horizontal axis for all ASCAT scatterometer swath positions and for wind speed (a), wind direction (b), and the meridional (c) and zonal (d) wind components. The winds are clearly within the specified accuracy of the OSI SAF wind product.

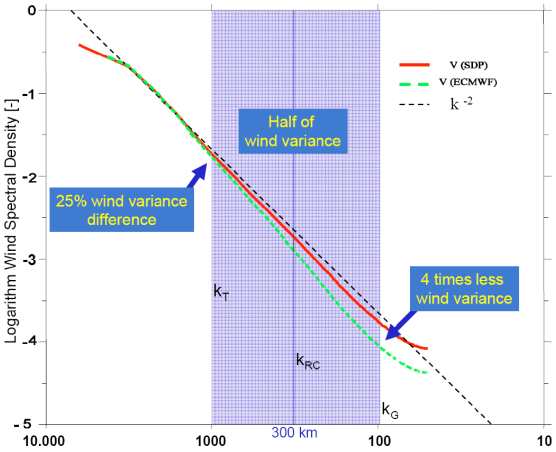

Figure 5. Wind variance versus spectral wave number k for a climatological spectrum (k-2), for the KNMI SeaWinds 25-km wind product (SDP), and for collocated NWP 10-m winds (ECMWF) on a 10log-10log scale[5]. With respect to the SeaWinds curve, the NWP spectral curve drops faster in variance over the blue shaded spectral range of corresponding wavelengths from 1000 km to 100 km.

The KNMI global ocean wind product from the ASCAT scatterometer instrument on the MetOp-A satellite is the first routine EUMETSAT MetOp-A geophysical product.

collocated set of ASCAT measurements. By performing such comparisons, KNMI has computed 'calibration' data to correct the backscatter measurements that, after wind processing, lead to ASCAT winds well within the user quality specifications[4]. Figure 4 gives an example. In the remaining MetOp-A commissioning period EUMETSAT will work together with KNMI towards calibrated radar backscatter data, improving the quality of the current ASCAT demonstration wind stream.

High resolution

The spatial consistency and detail in scatterometer sea surface winds is unprecedented. In many applications, such as storm surge and wave prediction, marine warnings and ocean forcing, NWP analysis winds are used as input, lacking mesoscale detail. For both operational real-time marine applications and oceanographic research it is important to characterise the differences between the scatterometer and NWP products. The difference in wind variance at smaller scales between SeaWinds and the ECMWF NWP model as shown in Figure 5 illustrates the general deficiency of NWP models. In particular, marked sharp structures in the scatterometer winds that are not represented in NWP analyses often appear near islands and in coastal regions. The smaller scales in the scatterometer winds suggest that ocean eddies which are of typical 10-km size are forced much more effectively in models by a scatterometer wind field than by NWP winds.

The standard KNMI 100-km QuikScat product has

been developed for NWP assimilation. It is verified to compare best with independent ECMWF NWP winds and is thus very suitable for NWP assimilation. At higher resolutions (< 100 km) more random noise is present in SeaWinds data[5]. Fortunately, SeaWinds noise reduction at 25 km resolution can be achieved by implementing the so-called Multiple Solution Scheme (MSS[6]). This scheme uses wind vector probability information from the wind inversion step[7] (Figure 2) in combination with 2D-Variational Ambiguity Removal, 2D-VAR. 2D-VAR implies a spatial meteorological balance in the near-surface wind by applying constraints on rotation and divergence[8]. The improvements in MSS are mainly due to the reduction of occasional erratic noise, while coherent mesoscale structures remain present and become more visible. In Figure 6 the MSS 25-km product is shown on the right. It is clear that with respect to the left-hand panel (at 100 km resolution) important mesoscale details, potentially useful for short range weather forecasting and nowcasting, become visible.

Different wind data sources represent different spatial scales: NWP models lack deterministic scales below 100 km, scatterometers present scales down to 25 km and in situ measurements are local. On the other hand, in terms of application, a local wind is only locally useful, while a field of cell-averaged winds comprehensively represents the conditions over a large area. Therefore, these wind observations cannot be mutually compared without taking into account spatial representation and the wind variability spectrum. Stoffelen and co-authors [9,10] included these aspects in a triple collocation comparison method and derived wind observation error measures. Table 1 presents recent RMS error values obtained from this study, showing the reasonable quality of NWP data in the extratropics, but relatively poor quality in the tropics. Buoy data appear somewhat inaccurate, since the error is computed for a space-averaged wind in a 50-km size scatterometer cell. As a consequence, the spatial wind variability on scales smaller than 50 km is here considered to be part of the buoy observation wind error.

Applications

Scatterometer winds are used by all major NWP centres and by the oceanographic community. At KNMI efforts are currently ongoing to assimilate high resolution ASCAT scatterometer data in the NWP High-Resolution Limited Area Model (HIRLAM) and operational implementation is planned for the second half of 2007. Emphasis is put on the assimilation of high-resolution products and on exploitation of winds on the short forecast range, particularly for extreme weather events. Moreover, these winds are today

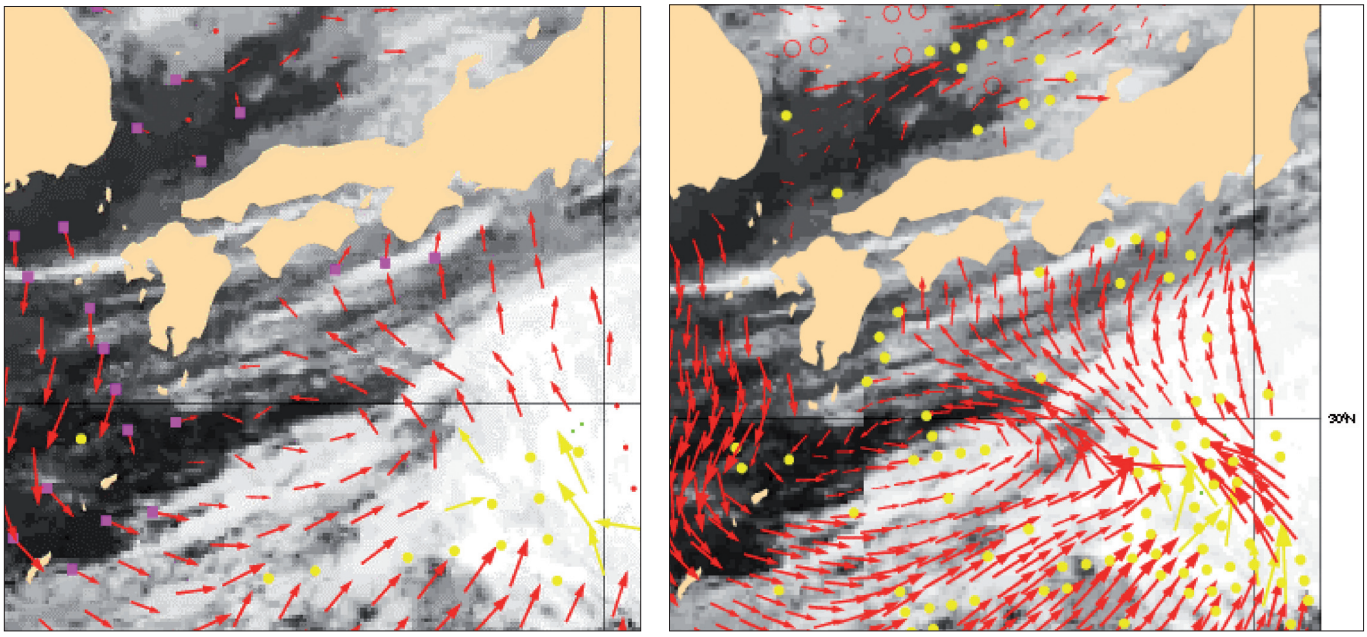

Figure 6. 100-km (left) and corresponding 25-km (right) QuikScat wind product. The latter shows additional mesoscale detail not present in the former. Yellow dots denote WVC QC, while yellow arrows fail the 2D-VAR spatial consistency check. GOES IR cloud imagery is provided underneath for reference and comparison (see also Figure 1 and 7).

Reinforced international collaboration between space agencies is the only solution to creating an effective ocean surface wind mission that for the benefit of mankind guaranties the availability of sufficient wind data over sea in the future.

being effectively used in near-real-time on the KNMI meteorological work station by the shift forecasters. These applications will particularly profit from the new ASCAT EUMETSAT Advanced Retransmission Service with a revolutionary timeliness of just 30 minutes after sensing.

Outlook

With the launch of ASCAT the series of C-band scatterometers is continued with extended coverage of the ocean surface wind and ice. EUMETSAT started timely user services in collaboration with KNMI. These services are now being further extended and are freely available at *http://www.knmi.nl/scatterometer*[11] for the SeaWinds, ERS-2 and ASCAT scatterometers (Figure 7). Research and development at KNMI will continue within the framework of the EUMETSAT Satellite Application Facilities (SAFs) to enhance the ASCAT wind processor capability towards a 12.5-km gridded product, make it operate nearer to the coast, and with improved geophysical modelling. Timely, highly accurate, spatially consistent and broad swath scatterometer winds provide the fine mesoscale structures over water surfaces. Since these transient atmospheric mesoscale structures are relatively short-lived, sampling only twice a day by one polar satellite is insufficient. Multiple scatterometers in space, separated in overpass time, would solve this temporal undersampling problem. The ERS-2 and SeaWinds scatterometers are now more than 12 and 8 years in space, respectively, and both multiplied their expected life times already. Although concrete plans exist in China and India to launch scatterometers, improved temporal sampling in the longer term after SeaWinds ceases is a critical issue. Therefore, reinforced international collaboration between space agencies is the only solution to creating an effective ocean surface wind mission that for the benefit of mankind guaranties the availability of sufficient wind data over sea in the future.

Vector RMS error [m/s]	TAO/PIRATA buoys Tropical	NDBC/MEDS/ UKMO buoys Extra-tropical
Buoy	1.5	1.5
Scatterometer	1.2	1.6
ECMWF model	2.0	2.1

Table 1. Wind vector error estimates (50-km scale) of buoy, scatterometer and ECMWF model winds based on a triple collocation method for a data set collocated with tropical buoys, 2nd column, and extra tropical buoys, last column[9,10].

1) Isaksen, L. and A. Stoffelen, 2000. *ERS-Scatterometer Wind Data Impact on ECMWF's Tropical Cyclone Forecasts.* IEEE-Transactions on Geoscience and Remote Sensing (special issue on Emerging Scattero-meter Applications), **38** (4), 1885-1892.

2) Hersbach, H., A. Stoffelen and S. de Haan, 2007. *An improved C-band scatterometer ocean geophysical model function: CMOD5.* J. Geophys. Res., **112**, C03006. doi:10.1029/2006JC003743

3) Portabella, M. and A. Stoffelen, 2006. *Scatterometer backscatter uncertainty due to wind variability.* IEEE Transactions on Geoscience and Remote Sensing, 44, 3356-3362.

4) Verspeek, J., A. Stoffelen and M. Portabella, 2007. *ASCAT wind calibration and validation.* OSI SAF report, SAF/OSI/KNMI/TEC/TN/163 v1.0, 28 pp.

5) Vogelzang, J., 2006. On the quality of high resolution wind fields. NWPSAF-KN-TR-002, Version 1.2, 31-08-2006 53 pp., .

6) Portabella, M. and A. Stoffelen, 2004. *A probabilistic approach for SeaWinds data assimilation.* Quart. J. Royal Meteor. Soc., **130**, 127-159.

7) Stoffelen, A. and M. Portabella, 2006. *On Baysian Scatterometer Wind Inversion.* IEEE Transactions on Geoscience and Remote Sensing, 44, 1523-1533.

8) Stoffelen, A., 2000. *A generic approach for assimilating scatterometer winds.* Proc. ECMWF seminar,

Reading, UK, 4-8 Sept. 2000, http://www.ecmwf.int/publications/library/ecpublications/_pdf/seminar/2000/sem2000_stoffelen.pdf
9) Stoffelen, A., G.-J. van Oldenborg, M. Portabella, J. de Kloe and A. Verhoef, 2006. *Scatterometer Ocean Stress.* Report to the CM-SAF, http://www.knmi.nl/scatterometer/
10) Portabella, M. and A. Stoffelen, 2006. *Development of a global scatterometer validation and monitoring.* Visiting Scientist Report for the EUMETSAT OSI SAF., www.osi-saf.org
11) KNMI scatterometer site, http://www.knmi.nl/scatterometer

Determination of the mixing layer height from ceilometer backscatter profiles

Marijn de Haij, Henk Klein Baltink and Wiel Wauben

Introduction

The mixing layer height (MLH) is a key parameter in studies of many atmospheric boundary layer processes, including air quality. It primarily determines the volume in which turbulence is active and into which constituents, which are emitted near the surface, are dispersed. The height of the mixing layer typically varies between 50 and 2500 m for The Netherlands, depending on, for example, the season, time of day, the synoptic situation and local conditions as orography, land use and surface roughness.

The research presented here is performed as part of the project Integrated observations and modelling of Greenhouse Gas budgets at the national level in The Netherlands[1)], (hereafter ME2 project). The overall goal of the ME2 project is to improve the description of the temporal and spatial distribution of greenhouse gases in the Netherlands. One of the work packages focuses on the influence of the dynamics and mixing processes in the Planetary Boundary Layer (PBL) on greenhouse gas concentrations. An important task within this work package is the continuous monitoring of PBL height and the driving variables for PBL growth (e.g., sensible heat flux) at several locations in the Netherlands. KNMI actively participates in the ME2 project, together with nine other Dutch research institutes and universities.

Below is a description of the study which was carried out to test the feasibility of the mixing layer height detection from the backscatter profiles of a commercial ceilometer. The instrumentation and developed method are described, whereafter a case study and the general results on the feasibility of the method are discussed. Finally, some concluding remarks are given, together with an outlook on the BSIK-ME2 measurement campaign.

Instrumentation

A lidar (LIght Detection And Ranging) system has been recognised as a suitable instrument to detect the boundaries of aerosol layers[2,3,4)]. A lidar system transmits laser pulses vertically and measures the backscattered signal. The strength of the backscattered signal depends on the amount of scattering particles in a volume at a certain distance from the instrument. The time interval between transmission and reception of the signal determines the distance. The backscatter profile is the backscattered signal as a function of height.

A ceilometer is a commercial lidar system that is primarily used for the detection of cloud base heights for aviation and meteorology. Ceilometers are designed to operate and measure continuously and require little maintenance. KNMI operates Vaisala LD-40 ceilometers (Figure 1) at about 25 locations in its meteorological observation network in The Netherlands.

The presence of aerosols can be detected in the backscatter profile of a ceilometer. As aerosols are mainly emitted at the surface, the concentration is generally higher in the mixing layer than in the free troposphere. Therefore the MLH estimation by lidar systems is based on the detection of the sharp decrease (gradient) in aerosol backscatter at the top of the mixing layer. This decrease marks the interface between the aerosol containing mixing layer and the relatively clean free troposphere. Other commonly used instruments for the estimation of the mixing layer height are SODARs (SOund Detection And Ranging), wind profilers and radiosondes[5)]. These instruments use gradients in the acoustic refractive index, radar refractive index and in the temperature and humidity profiles respectively, to determine the MLH.

Method

The ceilometer MLH algorithm[6)] applies a Haar wavelet transform to locate the strong negative gradient in the aerosol backscatter at the top of the mixing layer[7)] (see Figure 2). The wavelet algorithm is applied to the 10 minute averaged, range- and overlap-corrected, backscatter profile within a vertical domain of 90-3000 m. Furthermore the upper range limit is restricted by the lowest cloud base and the SNR<1 height. The latter is the height where the SNR (signal-to-noise-ratio) drops below 1, indicating the range for which the backscatter signal is assumed to be reliable enough for MLH estimation. The algorithm

Figure 1. Map of the KNMI meteorological observation network in The Netherlands. The locations with a LD-40 ceilometer (inset photograph) are represented by black dots.

The mixing layer height is a key parameter in studies of many atmospheric boundary layer processes, including air quality

is able to estimate up to two mixing layer heights, referred to as MLH1 and MLH2. A quality index has been introduced to make a first estimate of the reliability of the derived mixing layer height. This index is related to the difference in backscatter just below and above the estimated mixing layer height. Time series of the MLH detection hold information on the consistency of the results.

Case studies

The backscatter contour plot and resulting MLH estimates for Cabauw on July 27th, 2002 are shown in Figure 3. The development of a convective mixing layer is clearly observed, with a sharp and

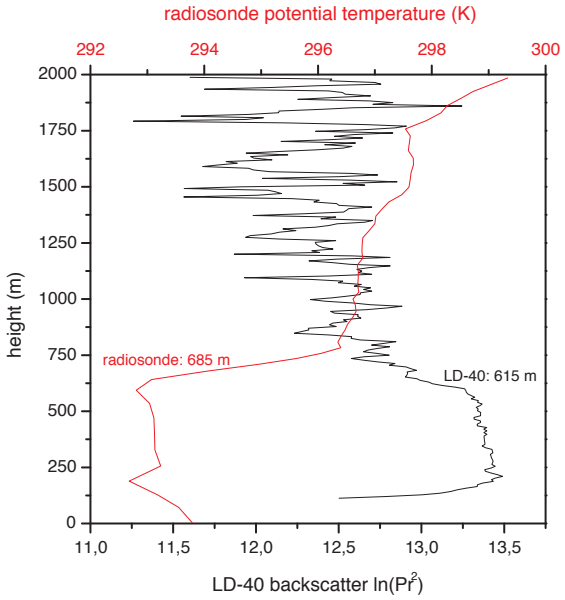

Figure 2. LD-40 backscatter profile (black) and radiosonde potential temperature profile (red) for De Bilt on September 23rd, 2005, 12 UTC. Note the good agreement of the mixing layer height estimates.

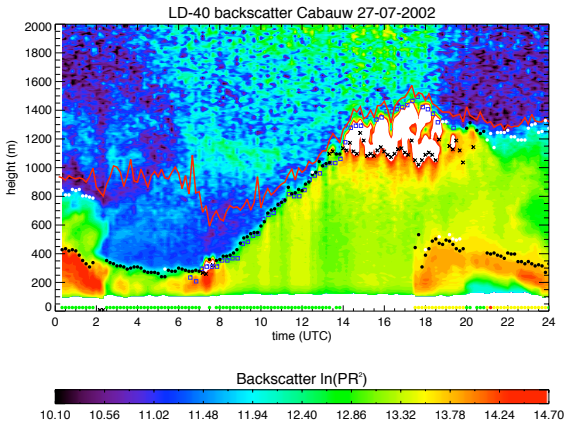

Figure 3. LD-40 backscatter contours and derived mixing layer heights for Cabauw on July 27th, 2002. Legend: MLH1 (black dot), MLH2 (white dot), wind profiler MLH (blue square), SNR<1 height (red line). The MLH1 quality indices are represented by the dots below the contours (green='good', yellow='weak', red='poor').

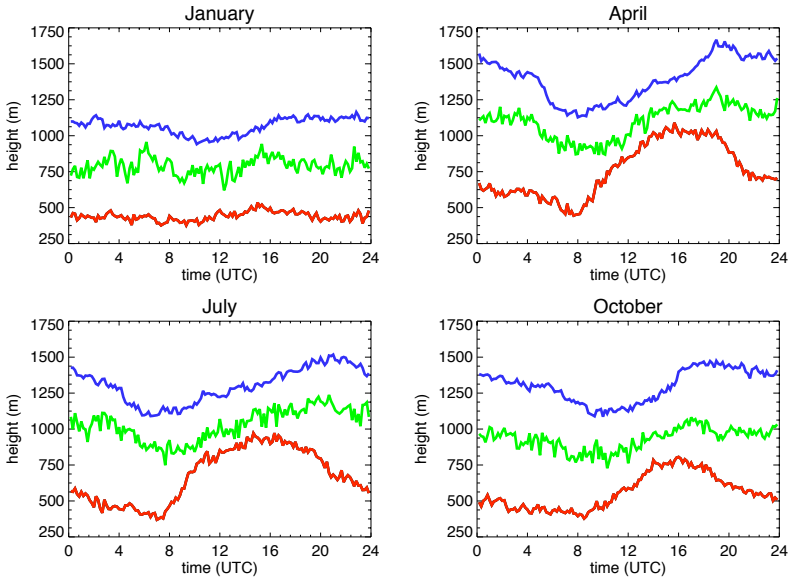

Figure 4. Monthly mean diurnal cycle in January, April, July and October for De Bilt (2000-2005), of MLH1 (red), MLH2 (green) and the SNR<1 height (blue).

strong decrease in aerosol backscatter between the mixing layer and the free atmosphere. The resulting MLH time series shows a low variability on small time scales. The build up of the convective layer is disturbed around 1400 UTC by the development of cumulus clouds on top of the mixing layer. These clouds restrain the algorithm from detecting the mixing layer height successfully. Around 1730 UTC a new aerosol layer is observed, which extends between 200 and 500 m above ground level during the evening. The occurrence of this layer coincides with a change in wind direction and marks the advection of an air mass containing aerosol from a different source area. During the first two and last three hours of this day, a secondary MLH is detected above the elevated aerosol layer. This secondary MLH is associated with the top of the so-called residual layer.

Feasibility of the method

Six years of backscatter profiles (2000-2005) from the LD-40 at the KNMI test field in De Bilt have been used to assess the overall performance of the ceilometer MLH algorithm with respect to the monthly availability and reliability of the MLH estimates[6]. The monthly mean diurnal cycle of the mixing layer heights and the SNR<1 height for January, April, July and October are shown in Figure 4, representative for the winter, spring, summer an autumn season, respectively. The typical shape of the development of a convective mixing layer is observed, as well as an evident annual cycle of the amplitude of the diurnal variation. However, the monthly mean MLH1 during daytime observed for spring and summer months is lower than expected. Further research showed that the ceilometer is unable to detect most of the deep mixing layers heights, especially under strong convective conditions. One must keep in mind that the ceilometer MLH algorithm needs sufficiently high aerosol concentrations in order to be able to derive a MLH. Since the backscatter signal of aerosol is much less than for clouds, the sensitivity and hence the range of a ceilometer for MLH detection is much less than for cloud base detection. The overall detection rate for MLH1 is between 42 % (December) and 60 % (June). However, the relative contribution of 'Weak' and 'Poor' detections increases with increasing detection rate. The higher MLH values as observed during daytime in April and July (Figure 4) generally coincide with lower quality indices. This is likely related to the enhanced vertical variability in the backscatter signal in these months. This increases the chance of a faulty detection of the mixing layer height at a less pronounced decrease in the aerosol backscatter. Beside this, the most important reason for the lower detection rates during the winter months is the frequent occurrence of fog, rain and clouds, which inhibit a successful MLH detection. Note that in case of boundary layer clouds the cloud base height can sometimes be used as an approximation for the MLH.

A comparison of MLHs estimated by the MLH algorithm and a radiosonde method applied to 1200 UTC profiles of temperature and humidity in De Bilt, is

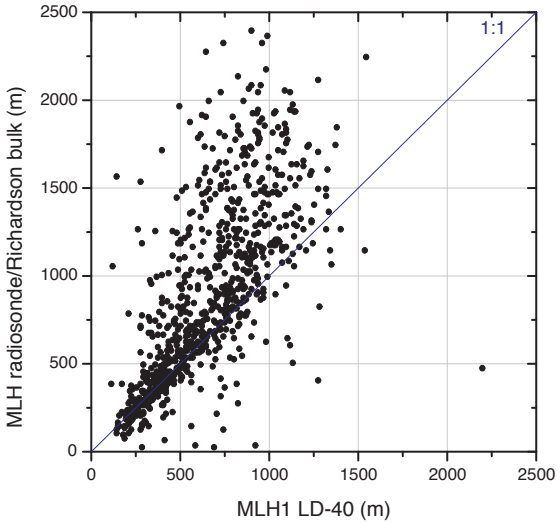

Figure 5. MLH1 from the LD-40 against MLH derived by the Richardson bulk method applied to radiosonde profiles in De Bilt at 12 UTC, 2000-2005.

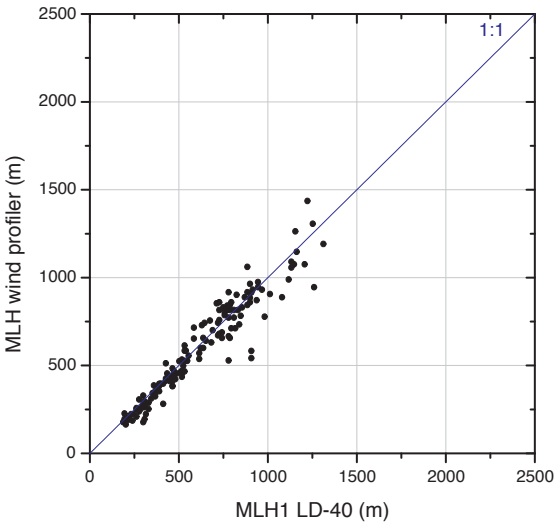

Figure 6. MLH1 from the LD-40 against MLH derived by the wind profiler in Cabauw for eight days in August 2001.

A lidar (LIght Detection And Ranging) system has been recognised as a suitable instrument to detect the boundaries of aerosol layers

shown in Figure 5. The agreement between the ceilometer and radiosonde is poor if all MLH estimates are considered. In particular for values of LD-40 MLH above 500 m much scatter is observed. The MLH derived by the radiosonde methods is mostly higher than the LD-40 estimates. A major improvement in agreement between the LD-40 and the radiosonde MLH is seen when only the detections with the highest quality index are taken into account. As a consequence of this selection, the number of points in the scatter plot decreases from 41 % to 16 % of the total number of used radiosoundings in the considered period. Very consistent results are found in the comparison of LD-40 and wind profiler MLH in Cabauw on eight days in August 2001, as shown in Figure 6.

Conclusions

An automated method was developed to derive the mixing layer height from the backscatter profiles measured with a Vaisala LD-40 ceilometer. The detection of the mixing layer height is based on the (strong) decrease in aerosol backscatter at the transition from the polluted mixing layer to the relatively clean free atmosphere. Although the detection is feasible by the method presented, limitations exist. The reliability of the MLH detection is strongly connected to the variability of the aerosol backscatter signal in height. Profiles that show a fairly constant and sufficient amount of aerosol backscatter generally give a reliable detection of MLH. This mainly occurs when the mixing layer grows not too deep, e.g. in a shallow wintertime mixing layer. Furthermore, problems sometimes occur during the afternoon decay of the convective mixing layer or for the nocturnal mixing layer. The problems encountered are partly caused by instrumental limitations. As commercial ceilometers were originally developed for cloud base detection, the sensitivity to aerosols is lower than for research lidars. The quality index gives a good indication of the reliability of the MLH detection.

Outlook

The BSIK-ME2 measurement campaign is executed from July 2007 to July 2009. As a part of this campaign, KNMI will store and process backscatter data from six LD-40 ceilometers. A good colocation with scintillometry instruments operated by Wageningen University (WUR) was aimed for in the set-up of the ceilometer network. Scintillometers measure the area averaged sensible heat flux, which is the driving mechanism behind the development of the daytime mixing layer. Hence, the spatial variation of the MLH

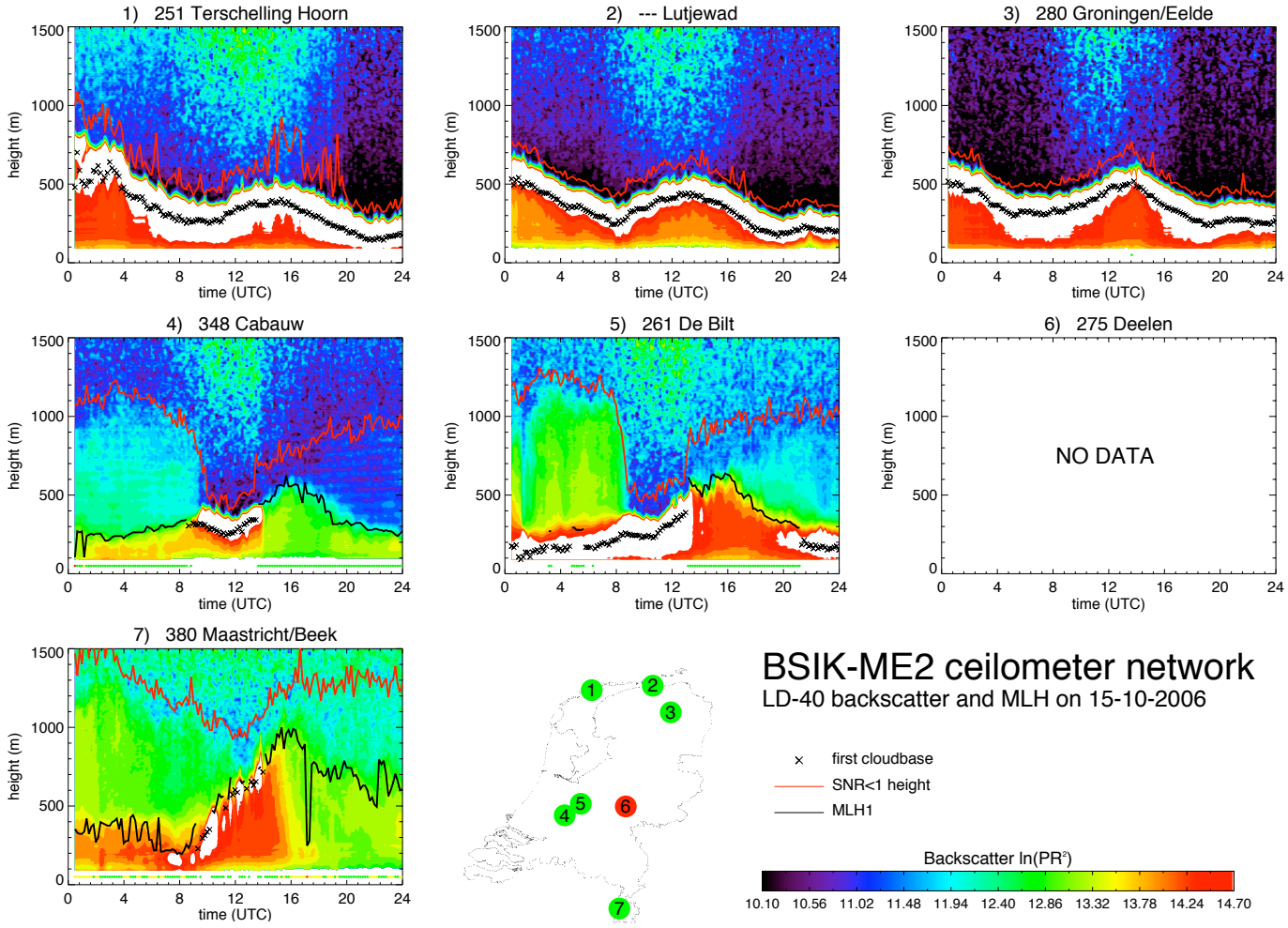

Figure 7. LD-40 backscatter contours and the estimated mixing layer height for the BSIK-ME2 ceilometer network on October 15th, 2006.

can be coupled directly to a variation in the sensible heat flux. The six selected locations are Hoorn (Terschelling), Eelde, Cabauw, De Bilt, Deelen and Maastricht. A quicklook of backscatter data and the resulting MLHs for this small network on October 15th, 2006 is shown in Figure 7.

During the campaign the usefulness of the ceilometer MLH product will be further evaluated. Depending on the results of the evaluation the implementation of the wavelet algorithm in the sensor interface of the KNMI operational ceilometer network will be considered. After such an implementation the MLH for all ceilometer locations in the Netherlands would become available to users every 10 minutes in near real-time.

This project is executed in the frame of the programme Climate changes Spatial Planning (BSIK-KvR)[8].

1) Hutjes, R.W.A., 2005. *Integrated observations and modelling of Greenhouse Gas budgets at the national level in the Netherlands.* Project proposal BSIK ME2 project, Wageningen, The Netherlands.
2) Ruiter, A. de, and D.P.J. Swart, 1991. *Automatische menghoogtebepaling met lidar.* PhD Thesis, University of Amsterdam, Amsterdam, The Netherlands.
3) Cohn, S.A. and W.M Angevine, 2000. *Boundary layer height and entrainment zone thickness measured by lidars and wind-profiling radars.* J. Appl. Meteor., **39**, 1233-1247.
4) Schäfer, K., S. Emeis, A. Rauch, C. Münkel and S. Vogt, 2004. *Determination of mixing layer heights from ceilometer data.* Remote Sensing of Clouds and the Atmosphere IX, Proc. of SPIE, Bellingham, WA, USA, 5571, 248-259.
5) Seibert, P., F. Beyrich, S.-E. Gryning, S. Joffre, A. Rasmussen and P. Tercier, 2000. *Review and intercomparison of operational methods for the determination of the mixing height.* Atmos. Environm., 34, 1001-1027.
6) Haij, M.J. de, H. Klein Baltink and W.M.F. Wauben, 2007. *Continuous mixing layer height determination using the LD-40 ceilometer: a feasibility study.* KNMI Scientific Report WR 2007-01, 98 pp.
7) Brooks, I.M., 2003. *Finding boundary layer top: application of a wavelet covariance transform to lidar backscatter profiles.* J. Atm. Oceanic Technol., **20**, 1092-1105.
8) *Klimaat voor Ruimte website, www.klimaatvoorruimte.nl*

Upper Air Humidity observations using GPS

Siebren de Haan and John de Vries

Introduction

Humidity plays an important role in atmospheric processes like convection, cloud formation and precipitation, and it is highly variable in space and time. The current operational meteorological observing system relies almost entirely on radiosonde observation for upper air humidity measurements. Radiosondes are launched typically two to four times per day, leaving large parts of the day unsampled.

Ground based Global Navigation Satellite Systems (GNSS), such as the well known Global Positioning System (GPS, United States) and, in the future, Galileo (Europe), can partially fill this lack of information. Because GPS is currently the only operational GNSS we will use the term GPS in the text below. GPS signals, transmitted by a GPS satellite and received on earth are bended by the atmospheric refractivity resulting in a signal delay. When the satellite and receiver position are known an estimate of the total refractivity along the signal path can in principle be made. Refractivity depends on temperature, atmospheric pressure and humidity. When temperature and pressure are known, information on the humidity can be derived. In practice, also other unknowns such as receiver clock offsets have to be estimated.

The benefit of GPS humidity observations lies in the fact that the observations are possible in any weather situation and the observation period can be as small as 5 to 15 minutes. The deficit is that the observations are (currently) restricted to land and that an integrated quantity is observed and not a profile. Below, the method of observing upper humidity using GPS is explained. Next, some applications of GPS upper air humidity are discussed.

Method of observing upper air humidity using GPS

To accurately estimate the total delay due to the atmosphere, the positions of the GPS receivers have to be known with an accuracy of a few millimetres. This requires a fixed stable network with high-standard GPS receivers. Note that low-cost GPS receivers have a position accuracy of a few meters. In The Netherlands a network of 35 receivers is installed as a result of close collaboration, called NETPOS, between the Kadaster (the National Surveying Department of the Netherlands) and the Ministry of Transport, Public Works and Water Management. On three remote automatic weather stations operated by KNMI a GPS receiver is installed. In return KNMI has access to raw GPS time delay observations of the network. This data is available in batches of one-second values every 5 minutes with a delay of less then 2 minutes.

Surveying with GPS with an uncertainty of a few centimetres is achieved using NETPOS. All raw one-second GPS data received by the network are processed to calculate a first order atmospheric correction. For atmospheric applications a higher accuracy in positioning is needed. This higher accuracy requires estimation of several unknowns such as satellite position and receiver clock errors. By collecting and processing all raw GPS time delay observations from the network over a period of several hours this accuracy can be met. Furthermore, a network of GPS receivers with baselines longer than 1000 km, will improve the absolute accuracy of the atmospheric estimate. In Figure 1 the network of the GPS receivers used for meteorological applications is shown.

The open circles denote the sub-network used to calculate atmospheric delays every hour and the

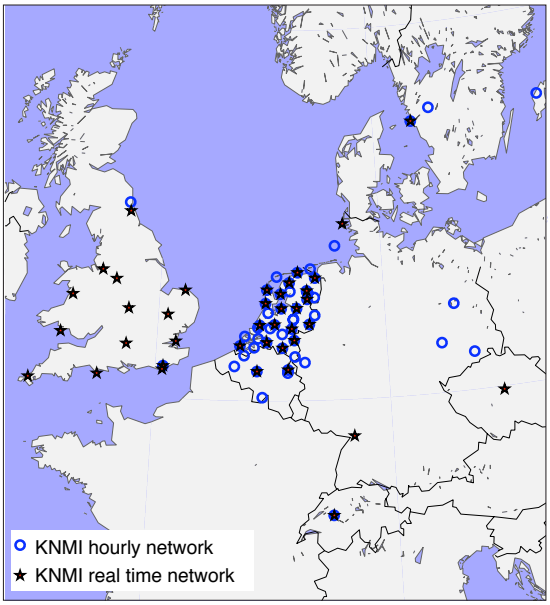

Figure 1: GPS receiver network used for processing at KNMI. KNMI is generating two types of ZTD's: an observation available every hour (sites denoted by open circles) and every 15 minutes (sites denoted by asterisk).

asterisks show the sub-network for real-time applications. The first product is available after 45 minutes of the last observations and is aimed to be used in numerical weather prediction models, while the real-time delay is less accurate but still suitable for nowcasting purposes.

The atmospheric delay is called the Zenith Total Delay (ZTD) and is determined for each GPS receiver. ZTD can be expressed as a sum of a dry and wet part, the so-called Zenith Hydrostatic Delay (ZHD) and the Zenith Wet Delay (ZWD). The ZHD can be approximated using the surface atmospheric pressure[1], and thus the ZWD can be computed from the total delay by subtraction. The ZWD is proportional to the vertically integrated column of water vapour (IWV) over the GPS receiver. This relation depends on the mean temperature of the atmosphere, which can be approximated by a function of the surface air temperature[2]. So IWV can be obtained from a ZTD observation.

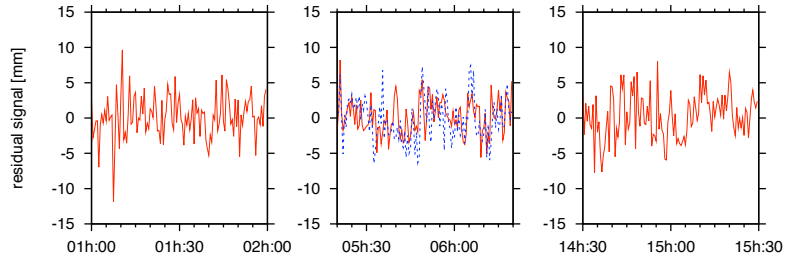

Figure 2: Residual signal of the GPS receiver for three different intervals of one hour. The middle panel shows the residual from two satellites; for the other panels only one residual was observed above 50 degrees elevation.

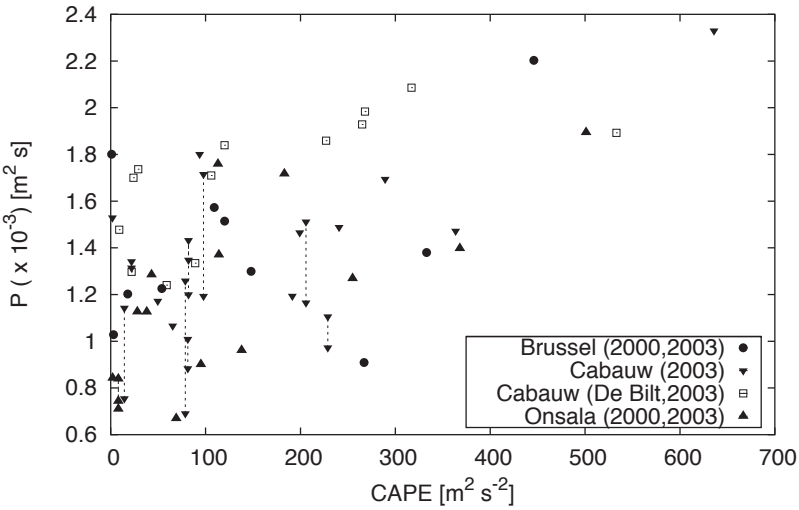

Figure 3: Scatter plot of Convective Available Potential Energy (CAPE) as observed by radiosonde measurements and spectral power density (P) for two periods (two weeks in November 2000 and May 2003) and three GPS sites and four radiosonde launch sites. Symbols are connected by a line when more than one GPS satellite was visible.

Applications of GPS humidity observations

Atmospheric instability and GPS

In fact, ZTD is an average over time and space of the delay of the GPS signal. The difference between estimated ZTD mapped back on the line of sight between the receiver and satellite and the observed observation is called the residual signal.
This signal contains information on the state of the atmosphere. Figure 2 shows the residual signal with an observed elevation larger than 50 degrees mapped to the zenith. The major systematic errors (such as e.g. multipath signal reception) are removed from the signal, so the remaining signal will contain only noise and, when present, an atmospheric signature. In case of a convective atmosphere with significant updraft of humid air, the GPS signal will be influenced by fluctuations of the water vapour. Spectral analysis of a time series of one hour of GPS residual observations is performed to calculate the power spectral density (P) of the GPS signal. This parameter is compared to a measure of buoyancy called Convective Available Potential Energy (CAPE), which can be determined using radiosonde observations. In Figure 3 a scatter plot of P versus CAPE is shown for collocations of three GPS sites and four radiosonde launch sites. Despite the fact that the two measurements spaces are distinct (i.e. CAPE is based on a profile at a fixed time; P is based on a single value for the vertical averaged over a period of an hour) the correlation is remarkable (around 0.6). The continuous availability of GPS estimates may help the forecaster to detect atmospheric (in)stability[3].

EUMETNET E-GVAP

KNMI participates in the EUMETNET GPS water vapour programme (E-GVAP).This programme aims at providing the EUMETNET partners with European GPS delay data for use in operational meteorology. This is done in close collaboration with the geodetic community in Europe. EGVAP started April 2005 and is planned for four years.
A snapshot of the locations at which GPS ZTD estimates are measured and derived is shown in Figure 4. Implementation of ground based GPS data in operational NWP and nowcasting has requirements regarding quality, homogeneity, stability, actions to take in case of problems, extent of observation network, etc. A key goal of E-GVAP is to gradually

improve the ground based GPS (near-)real time delay data to meet these requirements.

The E-GVAP-programme is based on a combination of centralised tasks, which will be carried out by the E-GVAP team, and distributed activities, which will be handled by the national met-service members in collaboration with their geodetic colleagues.

The centralised tasks include database setup and maintenance, processing of GPS data from special selected sites and quality monitoring and feedback. The distributed functions include, amongst other things, enlargement of the GPS network in areas with poor coverage in liaison with the geodetic community.

Two dimensional water vapour fields
From real time GPS IWV two dimensional water vapour fields can be generated. These fields can be used for nowcasting of convection and thunderclouds. In the example shown in Figure 5 strong lighting events occur at the edges of water vapour ridges. The possible use of these water vapour fields for nowcasting will be a topic of research for the next few years.

Expected Impact of GPS Tropospheric Slant Delays
An alternative to vertically aggregated propagation delay observations is the actual delay along the slanted path of signal propagation from satellite to receiver. The intrinsic geometrical information in these so-called 'slant delays' offers the possibility of improved sampling of the local refractivity of the atmosphere in the vicinity of the receiver. A disadvantage of these observations is that they are likely to contain more noise. To find out if in spite of this detriment these observations contain useful information, an impact study was conducted with simulated slant delays.

The continuous availability of GPS estimates may help the forecaster to detect atmospheric (in)stability

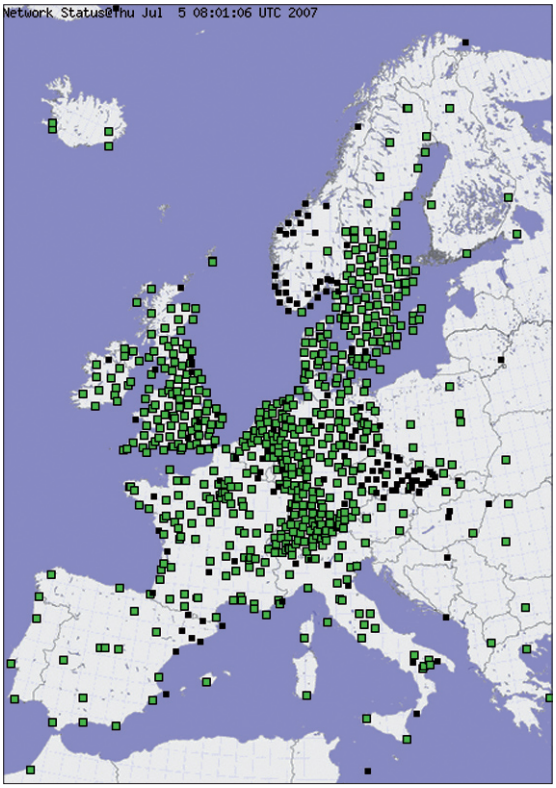

Figure 4: Locations in Europe with available GPS ZTD estimates. Operational sites are green; potential sites are black.

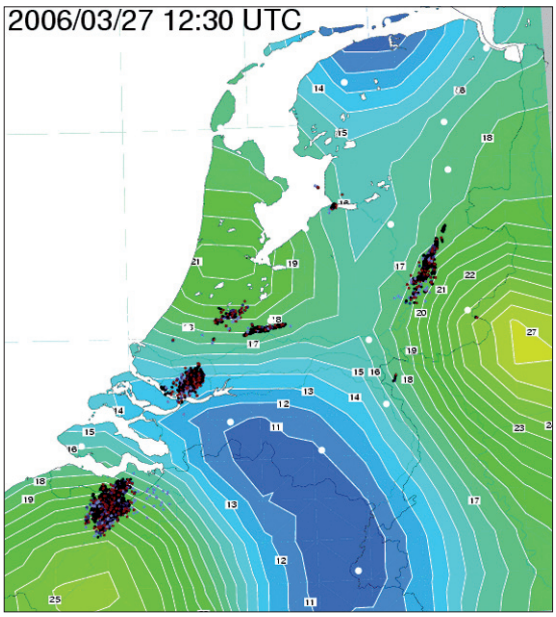

Figure 5: Example of the possible use of real time two dimensional GPS water vapour fields; a south westerly flow transported instable air which generated lightning events (black dots) in areas with a strong water vapour gradient, contoured from low values (blue) to high values (yellow).

The study comprised a System Simulation Experiment (SSE) carried out with the HIRLAM Forecasting System (HFS). The SSE is based on the Assimilation Ensemble Method (AEM), a probabilistic method originally used for the estimation of background errors[4,5] that has been extended and applied to simulate observation impact[6].

In this experiment three ensembles were generated, each defined by the set of observation types used in the ensemble:

- **Control** - The reference, incorporating all observations used in operations: SYNOP, SHIP, DRIBU, TEMP, PILOT, WINDPROF, AIREP and SATOB,
- **Denial** - As Control but without TEMP, PILOT and WINDPROF observations, a calibration experiment to determine the sensitivity of the HFS to humidity observations.
- **SDSIM** - As Control but with simulated slant delay observations added.

The ensembles consist of 4 members where each member represents an independent 14-day run of the forecasting system starting on May 2nd 2003 at 00 UTC. The model runs are performed on a 10km resolution grid with the Netherlands at the centre. The Denial ensemble is carried out to determine the sensitivity of the HFS for the input of moisture observations. It acts as a means to calibrate the SSE. For the SDSIM ensemble simulated noisy slant delay observations were generated before the experiment. They were computed from model fields of ECMWF analysis boundaries for the HFS using the HFS forward operator for GPS slant delays. In each assimilation cycle of the SDSIM ensemble on the order of 100 simulated slant delay observations are available from a GPS network mainly situated in the Netherlands. The slant delays were created using the actual GPS satellite constellation geometry at observation time.

For an ensemble with N members the RMS of *N-1* independent sets of analysis difference fields is called the analysis spread and represents a measure of the uncertainty in the analysis. The difference in the analysis spread between two ensembles that differ only in the set of observation types used in the analysis gives insight in the impact of a particular observation type.

The results of the Denial experiment generally confirmed the beneficial impact of radiosondes (not shown). To illustrate the impact of slant delays the analysis spread difference between the SDSIM and the Control ensemble for surface parameters and dew point temperature at the 850, 500 and 250 hPa level is presented in the maps in Figures 6 and 7 respectively. The maps in these figures show a reduction in the spread in red which signifies positive impact.
The yellow dots in and around The Netherlands in the panels represent the receiver stations in the GPS network.

For model surface fields of pressure reduced to mean sea level (PMSL), air temperature (T2m) and dew point temperature (Td2m) at 2 meter above the surface (at screen height) the impact is fairly neutral (Figure 6). The structure of the spread difference looks patchy for temperature and dew point temperature and amplitudes are small.

At 850 hPa positive impact is present around most stations of the GPS network and along the coast of Brittany (c.f. Figure 7). These structures reflect the

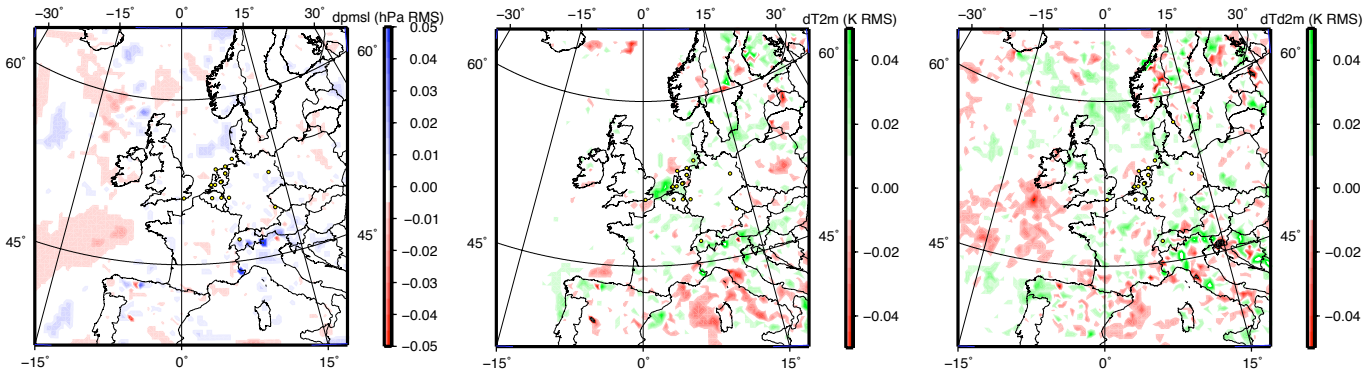

Figure 6: Differences in the spread between the members of the SDSIM and Control ensemble for surface parameters PMSL, T2m and Td2m.

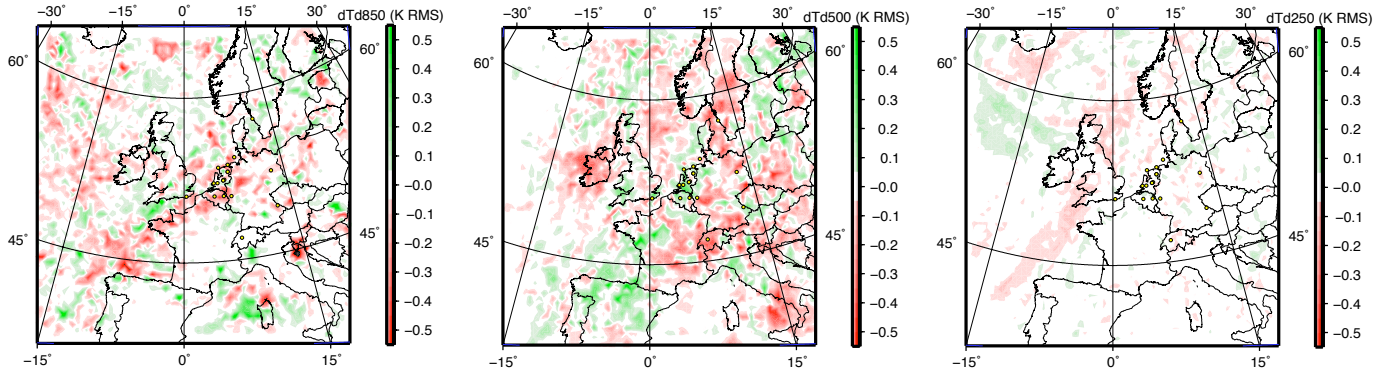

Figure 7: Differences in the spread between the members of the SDSIM and Control ensemble for dew point temperature at standard model levels 850, 500 and 250 hPa, indicated by dTd850, dTd500 and dTd250 respectively.

The spread differences for dew point temperature indicate that slant delays can achieve small local improvements in the accuracy of the upper air analysis

dominant flow regime at the time. At 500 hPa the impact is generally positive mainly over central Europe but remarkably not at the hart of the receiver network. There is no significant impact over the Atlantic Ocean. At 250 hPa the impact is neutral over Europe. Impact structures, positive or negative, are related to frontal systems over the Atlantic and are more large-scale than those at lower levels.

In general it was found that slant delay observations could not improve the accuracy of the analysis for PMSL and 2-meter air temperature beyond what can be achieved with radiosondes. For these parameters slant delay impact is mainly neutral. The spread differences for dew point temperature indicate that slant delays can achieve small local improvements in the accuracy of the upper air analysis.

Outlook

In the next few years GPS ZTD observations will become available on an operational basis at European scale, also at KNMI. Applications of GPS with respect to nowcasting will be further investigated, with emphasis on convective systems. As GPS ZTD becomes routinely available the observations will be assimilated in HIRLAM. In the case of GPS slant observations more research is required, especially in the pre-processing stage of creating the observations. Implementation of realistic spatial and temporal observation error characteristics in the assimilation system of the HFS is needed, followed by impact studies with real observations on a very high resolution grid (<5km) that have to be carried out for an extended period of time to study the effects of seasonal variations in atmospheric humidity.

1) Saastamoinen, J., 1972. *Atmospheric Correction for the Troposphere and Stratosphere in Radio Ranging of Satellites.* Geophysical Monograph Series, **15**, 247-251.
2) Bevis, M., S. Businger, T.A. Herring, C. Rocken, R.A. Anthes and R.H. Ware, 1992. *GPS meteorology: Sensing of atmospheric water vapour using the global positioning system.* J. Geophys. Res., **97**, 15.787–15.801.
3) Haan, S. de, 2006. *Measuring atmospheric stability with GPS.* J. Appl. Meteor., **45**, 3, 467-475.
4) Fisher M., 2003. *Background error covariance modeling. Recent Developments in data assimilation for Atmosphere and Ocean.* ECMWF Seminar Proceedings, Reading, UK, 8-12 September 2003, 45-64.
5) N. Zagar, E. Andersson and M. Fisher, 2005. *Balanced tropical data assimilation based on a study of equatorial waves in ECMWF shortrange forecast errors.* Quart. J. Royal Meteor. Soc., **131**, 987-1011.
6) D.G.H. Tan and E. Andersson, 2005. *Simulation of the yield and accuracy of wind profile measurements from the Atmospheric Dynamics Mission (ADM-Aeolus)*. Quart. J. Royal Meteor. Soc., **131**, 1737 - 1757.

Internet links
EGVAP: http://egvap.dmi.dk
Real Time Water Vapour: http://www.knmi.nl/research/groundbased_observations/gps/real_time_IWV.html

Accuracy assessment of an integrated profiling technique for operationally deriving profiles of temperature, humidity and cloud liquid water

Erik van Meijgaard, Henk Klein Baltink and Reinout Boers

Introduction

Precise quantification of the atmospheric state is essential for climate research and weather prediction. Historically most of the operational atmospheric profiling is performed by radiosondes, but this network is under pressure due to the high costs, and operational alternatives are not available. Clearly, radiosondes state benchmark measurements for profiling the atmosphere, but are usually operated only on a 12-hourly basis, hence short-lived weather events may not be captured. Also, ascents need typically one hour to profile the troposphere and underlie wind drift effects. Furthermore a method to measure condensed water with radiosonde operationally does not exist. Cost-effective and operational measurements of cloud liquid water content would be of high value for the evaluation and development of numerical weather prediction (NWP) and climate models. A pressing question still is to what extent a ground-based remote sensing profiling station could complement or partially substitute an operational radiosonde network.

Passive microwave radiometry has the potential of retrieving the atmospheric thermodynamic state in a quasi continuous and instantaneous way[1]. This requires a retrieval model which transforms the measured radiative quantities into thermodynamic information. In general, the retrieval problem is underdetermined. No unique solution exists but a wide range of possible thermodynamic structures give rise to the same set of measured radiative quantities. Further assumptions and additional measurements are needed to narrow down the number of valid solutions. Moreover, the vertical resolution of a typical stand-alone microwave profiler for temperature and humidity retrieval is rather coarse.

To overcome these shortcomings sensor synergy may prove beneficial. In the approach presented here, a continuous retrieval of the vertical structure of temperature, humidity and condensed water is achieved by employing synchronous and co-located measurements obtained with a microwave profiler, a cloud radar and a lidar ceilometer. These measurements are combined with a priori information from the nearest operational radiosonde. The cloud radar and lidar ceilometer can unambiguously locate a cloud in the vertical, filling a major gap left by the radiometer. The Integrated Profiling Technique[2] (IPT) combines these measurements in an optimal estimation framework.

This chapter addresses the accuracy of the IPT in describing the actual atmospheric state. The research is timely because remote sensing technology is becoming more accurate and affordable and operational systems are already being deployed at a number of stations mainly over Europe and the US.

In general it is not possible to assess the accuracy of the retrieval method because the 'true' state required to validate the retrieved state is unknown. This applies in particular to the cloudy component. E.g. in situ liquid water measurements are only sparsely available from aircraft and exhibit large measurement uncertainties. Moreover, it is impossible to measure instantaneously by aircraft the vertical column probed by a ground-based profiling station. To overcome the problem inherent in validating the IPT technique with real world data an accuracy assessment has been performed within a state-of-the-art model environment. There the atmospheric state and the measurements are exactly known at an arbitrary time and location. A further benefit is that the impact of the a priori information required by the IPT can be evaluated as a function of time and space with respect to the remote sensing measurements. For a detailed discussion on the implementation and results see Löhnert et al., 2007[3].

Accuracy assessment strategy

We apply an atmospheric model to create an artificial 'true' atmospheric state. This is the state we like to recover by applying the IPT to remote sensing measurements (Figure 1). Within the model world, measurements from real instruments do not exist. Instead, virtual instruments or forward models are used to calculate simulated measurements from the given atmospheric state (i.e. temperature, pressure,

A pressing question still is to what extent a ground-based remote sensing profiling station could complement or partially substitute an operational radiosonde network

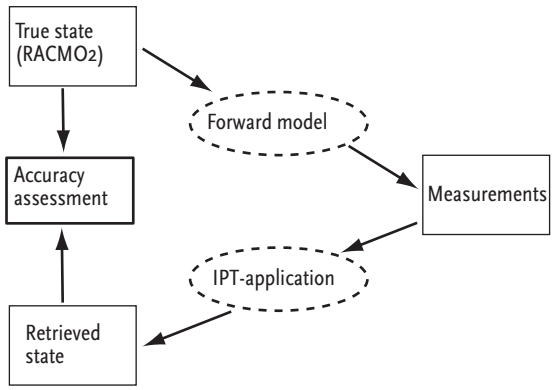

Figure 1. Concept of the experimental setup applied in this study.

humidity, cloud position and microphysics). The advantage is that we can exclude systematic measurement errors and systematic errors due to uncertainties in radiative transfer, which are almost impossible to quantify in reality. To produce realistic retrieval results, noisy errors typical for each measurement have been included.
A possible disadvantage of this approach is that the model atmospheric states may not cover the full range of observable states; the accuracy assessment is restricted to the model world itself. To transfer the findings to the real world, we must assume that the state-of-the-art atmospheric model represents the atmospheric state in a realistic manner for both mean and variability. The validity of this assumption can be tested by evaluating atmospheric models with measurements from long term observational campaigns like the European CloudNET and the US Atmospheric Radiation Measurement projects.

State vector, measurement vector and forward model

We have used the KNMI regional climate model RACMO2[4] to generate a time series of 'true' atmospheric states that must be reproduced by the retrieval. An uninterrupted model run, laterally forced by ECMWF analyses, has been performed for a 2-month period synchronous to the BBC1-campaign (August-September 2001).

The model output consists of vertical profiles at selected grid boxes of temperature, absolute humidity and cloud liquid water content (LWC), hereafter referred to as the atmospheric state vector. A forward model operator is applied to project this vector on the measurement vector containing the measured parameters, namely brightness temperatures from the microwave profiler, radar reflectivities from the cloud radar, and surface meteorological measurements of temperature and humidity.

The brightness temperatures are obtained from the given atmospheric state by applying a radiative transfer operator at the microwave profiler frequencies. In the retrieval scheme, cloud radar reflectivities are used to determine the altitude of the cloud. In addition a power law relation is used to relate radar reflectivity to the in-cloud liquid water content. Near surface values of temperature and humidity, required by the retrieval method, are taken from the lowest model level.

To make the experimental set-up realistic, random noise is added to the measurement vector. Variations in the aerosol loading are represented using a relation between radar reflectivity and liquid water content which depends on the cloud droplet concentration. Since aerosol amount is not a variable in RACMO, wind direction is used as a proxy to prescribe the variation in cloud droplet concentration in the range between 50 and 300 per cm^3, thereby mimicking air of maritime and continental origin, respectively.

Inversion of the measurement

The IPT is applied to the measurement vector in order to retrieve the atmospheric state vector in an optimal way. Determining the state vector from the measurement vector is an underdetermined and ill-conditioned problem. No unique solution exists and small errors in the measurement can lead to huge deviations in the retrieved profile. Therefore measurements are combined with a priori information, which can be regarded as a first guess solution. The optimal estimation equations[5] are suited for combining a set of instantaneous measurements with a priori information. Solving these equations requires knowledge of the a priori atmospheric state vector, the a priori covariance and the error covariance accounting for the combined measurement and forward modelling uncertainties.

In the real world, the a priori information will typically be taken from a climatology, a radiosonde ascent or a model forecast. In the model world we simulate the radiosonde information with model output from a grid column positioned at distance Δd from the measurement site and valid at time Δt prior to the measurement. In the now-casting mode we only utilize information from the most recent radiosonde ascent prior to the measurement. The now-casting mode reflects the IPT application to calculate thermodynamic profiles in real-time, once measurement and a priori data have been collected. The a priori covariance is constructed likewise by quantifying the assumption that the 00 (12) UTC sounding may serve as a proxy for the temperature and humidity profiles between 00 and 12 (12 and 24) UTC. In the model world, the calculation of the a priori covariance is straightforward, since model output of thermodynamic profiles is known at arbitrary temporal resolution. In the real world, the determination of the a priori covariance requires frequent radiosonde information, at least once per three hours. This is only feasible during intensive field campaigns like the BBC campaigns in 2001 and 2003 at Cabauw.

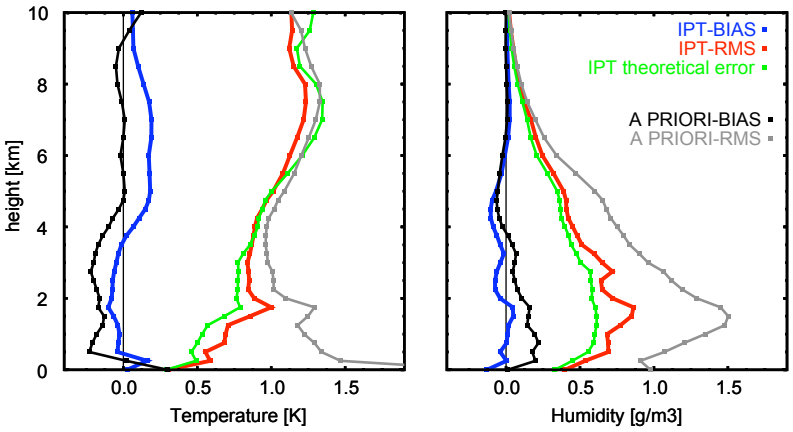

Figure 2. Accuracies of temperature and absolute humidity profiles for the now-casting mode.

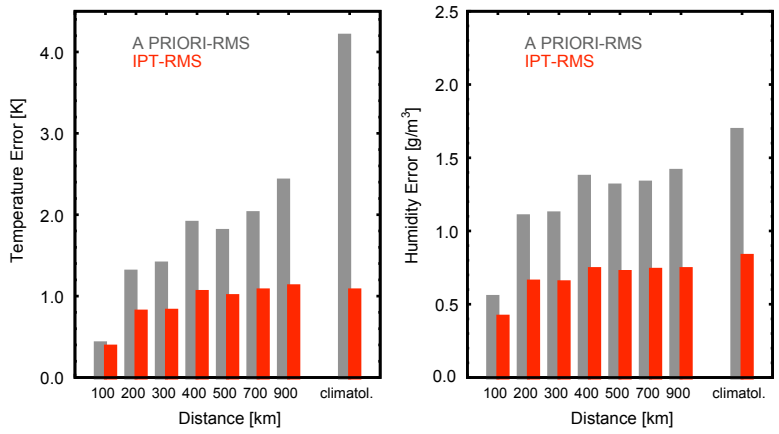

Figure 3. IPT and a priori accuracies for temperature and humidity averaged over the bottom 4 km of the atmosphere as a function of the distance between the radiosonde launch site and the remote sensing site. Grey bars: a priori RMS errors (assuming the persistent validity of the nearest and most recent radiosonde ascent), red bars: the IPT RMS errors, The last pair of bars (climatol.) shows results for a priori data inferred from a climatology.

As a priori for liquid water we use an average LWC profile derived from many realizations of a cloud microphysical model[6]. The LWC components of the a priori covariance are independent of temperature and humidity. Therefore the a priori covariance between these parameters is set to zero.

The error covariance matrix is constructed from considerations on propagation of errors corresponding to instrumental accuracy levels, radar calibration errors, but also uncertainty estimates associated to assumptions made e.g. in the relationship between radar reflectivity and liquid water content or in the interaction of microwave radiation with gaseous absorbers.

Retrieval of temperature and humidity profiles at the radiosonde site

A priori information is constructed in the now-casting approach. Also, the a priori information and the measurement vector are collocated. The results for temperature and humidity are shown in Figure 2. The IPT RMS (root mean square) errors that result from the IPT application are shown together with the RMS errors that come from assuming persistence of the a priori information (a priori RMS). The difference between these two RMS errors is the retrieval profit, i.e. the benefit due to the use of all measurements compared to the radiosonde alone. For temperature, the highest retrieval profit is in the lowest 2 km where the information added by the microwave profiler is highest. Also shown is the uncertainty associated with the error propagation, the so-called theoretical IPT error. When this error is comparable to the IPT RMS, the retrieval system is considered well balanced. Compared to temperature, the retrieval profit for humidity is more pronounced and extends to higher altitudes.

Retrieval of temperature and humidity profiles away from the radiosonde site

Next we carry out a sensitivity study with the central question: How accurate is the IPT if the a

IPT can add a significant retrieval profit to the profiles in the times between two radiosonde ascents

priori information comes Δd km away from the profiling station and from a discrete time period Δt hour prior to the actual measurement? The results shown in Figure 3 are relative to the combination 0km/0h, which represents the optimal result, because then the a priori information is already equal to the model truth and additional measurements can not improve on that. (In the previous paragraph a priori profiles were taken at Δd = 0 km, but Δt was encompassing all values from 0 to 12 h.) Applying Taylor's hypothesis all results have been expressed in terms of a spatial distance. The RMS values have been averaged over the lowest 4 km where the retrieval profits are largest. Not surprisingly the a priori temperature RMS increases with distance, but performs better than an a priori estimate from climatological data. For large distances the IPT RMS error is rather constant with values close to 1 K. Interestingly, a comparable value for the IPT RMS error is obtained, if a priori information is derived from climatological data. When a high accuracy is not demanded, the IPT can lead to a retrieval profit of more than 3 K in the lowest 4 km.

If IPT RMS accuracies better than 1 K are required, the profiling station should be located within a radius of 200 km from the radiosonde. Within this range, the retrieval profit is generally lower (due to the higher accuracy of the a priori information). However application of the IPT still improves the accuracy! Comparable results are found for humidity. When accuracies better than 0.5 gm^{-3} are required the distance between the radiosonde ascent and the station should be less than 100 km. Again, for distances of 400 km or beyond results with a priori information from a climatology are comparable to a priori information from radiosondes.

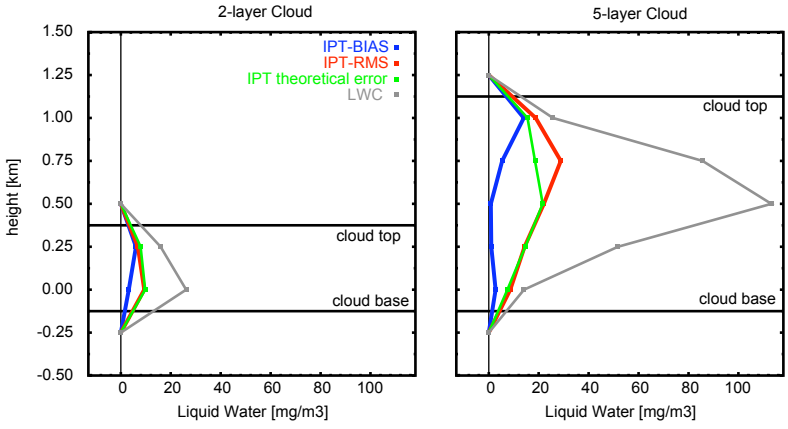

Figure 4. IPT RMS accuracies of liquid water content as a function of height above cloud base. The left panel shows the result for the class of relatively thin clouds (500 m), the right panel shows the result for the class of thicker clouds (1250 m).

Thermodynamic profile retrieval within liquid water clouds

The IPT version under investigation can handle clouds with a vertical extension up to 1500 m with a vertical resolution of 250 m. We have evaluated the IPT performance as a function of height to cloud base. Results for thin clouds (500 m) and thicker clouds (1250 m) are shown in Figure 4. In general, the IPT RMS errors increase with increasing cloud vertical extent due to larger amounts of LWC in geometrically thicker clouds. It is evident that the largest IPT RMS errors are correlated to the maximum LWC values within the profile. If the cloud layers nearest to cloud top and base are excluded from the analysis, the mean relative LWC error for clouds with vertical extent from 750 to 1500 m is approximately 30%. Also, the predicted theoretical IPT errors are found in rather good agreement with the derived IPT RMS errors.

Discussion and Outlook

We have discussed how ground-based remote sensors can be used in an optimal way to retrieve continuously the thermodynamic state of the atmosphere. For the retrieval of temperature and humidity profile, the highest information content originates from the brightness temperature measurements of microwave profilers. Due to the limited vertical resolution remote sensing instruments cannot achieve the accuracy of a radiosonde ascent. However, we have demonstrated that IPT can add a significant retrieval profit to the profiles in the times between two radiosonde ascents, at locations of up to 300 km away from the ascent.

The results for temperature and humidity retrievals have been obtained in the now-casting approach. We expect this approach to be a major focus in future, because it is suitable for real-time applications in short-term weather forecasting and data assimilation. An alternative approach is the climate mode in which

the a priori information is obtained by temporal interpolation of past and future information close to the time of the remote sensing measurement. The climate mode is particularly useful for the reprocessing of data time series where it is important to produce accurate physically consistent profiles of the atmosphere using as many measurements and as much a priori information as possible.

Although the results presented in this chapter are encouraging, it must be emphasized that they are obtained in an idealized setup. Transposition to the real world might introduce systematic errors associated with uncertainties in the radiative transfer operator and the instrument calibration. The underlying causes are in the treatment of microwave absorption due to gaseous components (oxygen and water vapour) and liquid water in standard absorption models. Also, receiver drifts and absolute calibration inaccuracies may lead to long-term instrumental offsets causing systematic deviations. Here, state-of-the-art microwave profilers (such as the RPG HATPRO[7]) can guarantee relatively high-accuracy and stable measurements. An advantage of the IPT-RACMO2 test-bed developed here is that systematic errors related to instrument characteristics and uncertainties in the microwave absorption may now be investigated in detail. This will help to assess whether instrument performance and forward model accuracy are really suited in getting the results close to the theoretically possible ones highlighted in this study.

---

1) Westwater, E. R., 1997. *Remote sensing of tropospheric temperature and water vapor by integrated observing systems.* Bull. Amer. Meteor. Soc., **78**, 1991-2006.
2) Löhnert, U., S. Crewell and C. Simmer, 2004. *An integrated approach towards retrieving physically consistent profiles of temperature, humidity, and cloud liquid water.* J. Appl. Meteor., **43**, 9, 1295-1307.
3) Löhnert, U., E. van Meijgaard, H. Klein Baltink. S. Gross and R. Boers, 2007. *Accuracy assessment of an integrated profiling technique for operationally deriving profiles of temperature, humidity and cloud liquid water.* J. Geophys. Res., **112**, D04205. doi:10.1029/2006JD007379
4) Lenderink, G., B. van den Hurk, E. van Meijgaard, A.P. van Ulden and J.H. Cuijpers, 2003. *Simulation of present-day climate in RACMO2: first results and model developments.* KNMI Technical Report TR-252, KNMI, De Bilt, The Netherlands, 24 pp.
5) Rodgers, C. D., 2000. *Inverse methods for atmospheric sounding: Theory and practice.* World Scientific, 238 pp.
6) Issig, C., 1997. *Ein spektrales Wolkenmodell mit integriertem Strahlungsübertragungsmodell zur Unterstützung von Niederschlagsalgorithmen.* PhD Thesis, University of Bonn, Bonn, Germany, 119 pp.
7) Rose, T., S. Crewell, U. Löhnert and C. Simmer, 2005. *A network suitable microwave radiometer for operational monitoring of the cloudy atmosphere.* Atmospheric Research, **75**, 3, 183-200. doi:10.1016/j.atmosres.2004.12.005

Satellite observations of air quality, climate and volcanic eruptions

Ronald van der A and Hennie Kelder

Introduction

Satellite observations of atmospheric constitents have many applications in the area of climate research, air quality monitoring and aviation safety. Here, we will focus on the satellite observations of two important trace gases, NO_2 and SO_2. Applications are air quality monitoring and support to aviation control.

Nitrogen oxides (NO_x, the collective name for NO and NO_2) play an important role in atmospheric chemistry and in the climate system as precursor of tropospheric ozone, an important greenhouse gas. The most important source of NO_x is the combustion of fossil fuels, mainly by traffic and large power plants. Other important contributors are the burning of biomass, soil emissions and lightning. Close to the earth surface the lifetime of NO_x is short (a few hours). Therefore, NO_2 concentrations will be highest close to the source. Nitrogen oxides affect the health of humans and animals. They irritate the lungs and lead to lower resistance to respiratory infections such as influenza. Frequent exposure to high concentrations may cause acute respiratory illness. Another serious problem caused by nitrogen oxides is the formation of aerosols and tropospheric ozone (i.e. smog), which has also harmful health effects. In addition, increasing tropospheric ozone affects climate.

Sulphur dioxide, SO_2, enters the atmosphere as a result of natural phenomena as well as anthropogenic activities, e.g. combustion of fossil fuels, oxidation of organic material in soils, volcanic eruptions, and biomass burning. Coal burning is by far the largest man-made source of SO_2 (about 50%), with oil burning accounting for a further 25 to 30%. Sulphur dioxide reacts on the surface of a variety of airborne solid particles, is soluble in water and can be oxidised within airborne water droplets, producing sulphuric acid. This acidic pollution can be transported by wind over large distances, and is deposited as acid rain. Changes in the abundance of SO_2 have an impact on atmospheric chemistry and hence on the climate. Consequently, global observations of SO_2 are important for atmospheric and climate research. Volcanic eruptions are important sources of ash and SO_2 in the atmosphere, which may have an impact on air traffic. Near-real time retrieval of SO_2 concentrations enables monitoring of such events and assists in aviation control. Off-line retrieval, on the other hand, is more suitable for monitoring anthropogenic pollution aspects.

Tropospheric nitrogen dioxide

Satellite observations

Satellite instruments (such as GOME, SCIAMACHY and OMI) use spectroscopy to retrieve atmospheric trace gas concentrations in the atmosphere. By comparing the measured spectrum of the backscattered light from the Earth's atmosphere with a reference spectrum, the column density of nitrogen dioxide along the light path can be determined. The NO_2 stratospheric column is deduced from a chemistry-transport model assimilation run of the NO_2 column data. Subsequently, the assimilated stratospheric column is subtracted from the retrieved total column, resulting in a tropospheric column. Information about the global tropospheric NO_2 columns is publicly available on the TEMIS (Tropospheric Emission Monitoring Internet Service) website *htpp://www.temis.nl*. TEMIS is a service, led by the KNMI, that provides tropospheric data from satellites freely to a wide range of users and applications. More details about the satellite observations and the retrieval technique can be found in several publications[1,2,3].

NO_2 has been monitored by satellite since 1995 with GOME, since 2002 with SCIAMACHY, and since 2004 with the OMI instrument; the latter two instruments having the advantage of a high spatial resolution. In Figure 1 the mean tropospheric NO_2 is shown as measured by OMI in the period May 2006 till February 2007. Clearly visible are the industrial regions in China, Europe, South-Africa and the USA. The yearly averaged NO_2 column for 2005 measured with SCIAMACHY zoomed-in over China can be seen in Figure 2. It shows high concentrations of NO_2 above highly populated regions like Beijing, Shanghai, Hong Kong and South Korea. It can also be seen that the satellite detects the emissions around the Yellow river (Huang He). Over the sparsely populated western

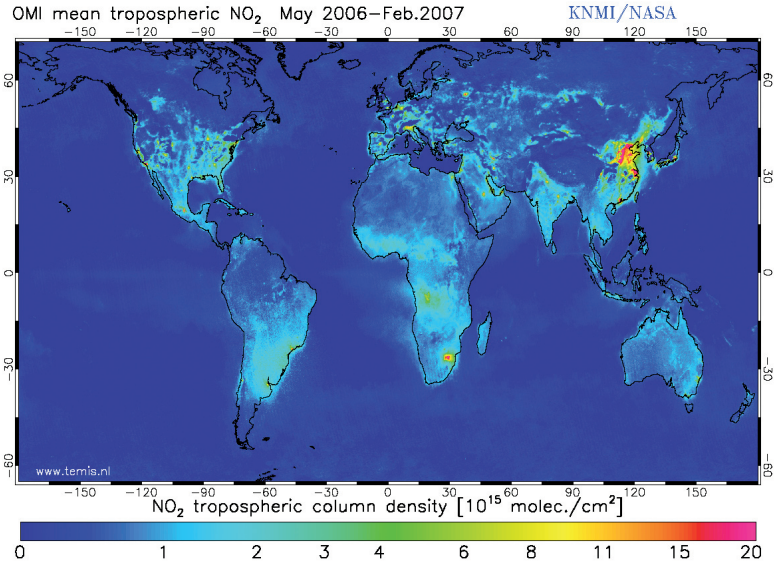

Figure 1. World map of the averaged tropospheric NO_2 column measured by OMI in the period May 2006 till February 2007.

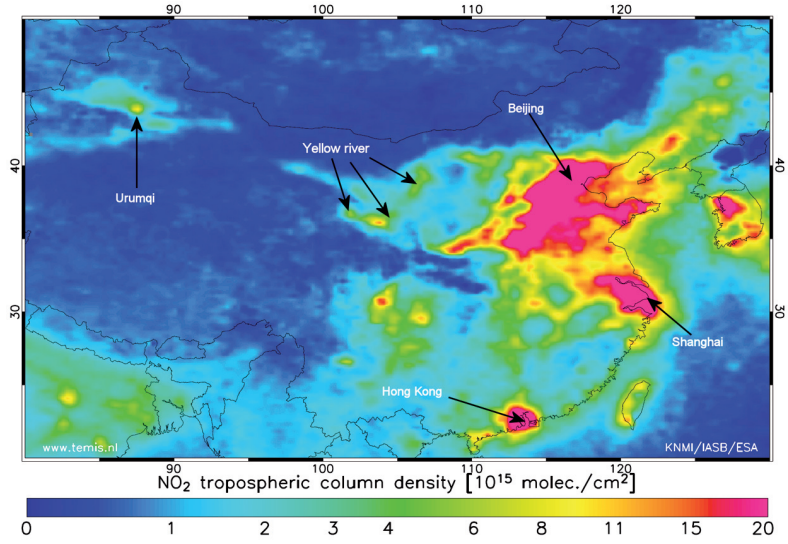

Figure 2. The yearly averaged tropospheric NO_2 column measured by SCIAMACHY for 2004 in China. High values are measured above the major cities. The industrial area around the Yellow River (Huang He) is also noticeable and highlights the river stream.

part of China, low NO_2 concentrations are observed, except over the large city Urumqi in the Northwest.

Air quality monitoring

Blond and co-authors[4] have shown that SCIAMACHY provides detailed information on the nitrogen dioxide content in the planetary boundary layer. The cloud free satellite observations were compared with surface measurements and simulations over Western Europe performed with the regional air-quality model CHIMERE (shown in Figure 3). The model has a resolution of 50 km, similar to the satellite observations. CHIMERE seems to underestimates surface NO_2 concentrations for urban and suburban stations but this is mainly attributed to the low representativeness of point observations. No such bias is found for rural locations. The yearly-average SCIAMACHY and CHIMERE spatial distributions of NO_2 show a high degree of quantitative agreement over rural and urban sites: a bias of 5% (relative to the retrievals) and a correlation coefficient of 0.87 (n=2003). The consistency of both SCIAMACHY and CHIMERE outputs over sites where surface measurements are available gives confidence in evaluations of the model over large areas not covered by surface observations. The NO_2 columns show a high daily variability. Still, the daily NO_2 pollution plumes observed by SCIAMACHY are often well described by CHIMERE both in extent and in location. This result demonstrates the capabilities of a satellite instrument such as SCIAMACHY to accurately monitor the NO_2 concentrations over large areas on a regular basis. It provides evidence that present and future satellite missions, in combination with a regional air quality model and surface data, will contribute to improve quantitative air quality analyses at a continental scale.

Trends in tropospheric NO_x emissions

The combined measurement series of both GOME and SCIAMACHY almost span a decade, which allows for a trend analysis of NO_2 concentrations. To do so, the averaged monthly tropospheric NO_2 columns are fitted with a linear model that also includes a sinus to represent the seasonal variation of NO_2. The seasonal variation for anthropogenic NO_2 is mainly determined by the changing day-length over the year. In absence of sunlight NO_2 has a longer lifetime in the atmosphere, which explains that the NO_2 columns are on average higher during wintertime. By applying the model to each grid cell a spatial distribution of the fit parameters is calculated. Furthermore the precision of the trend is calculated. It can be concluded that the 10 years long NO_2 dataset from GOME and SCIAMACHY can be used for significant trend analysis in most parts of the world. In highly populated and industrialised areas the trend is large enough to be significant. For instance Shanghai had a yearly increase of tropospheric NO_2 of about 29% since 1996. Figure 4 shows the derived annual growth in the tropospheric NO_2 columns from this analysis.

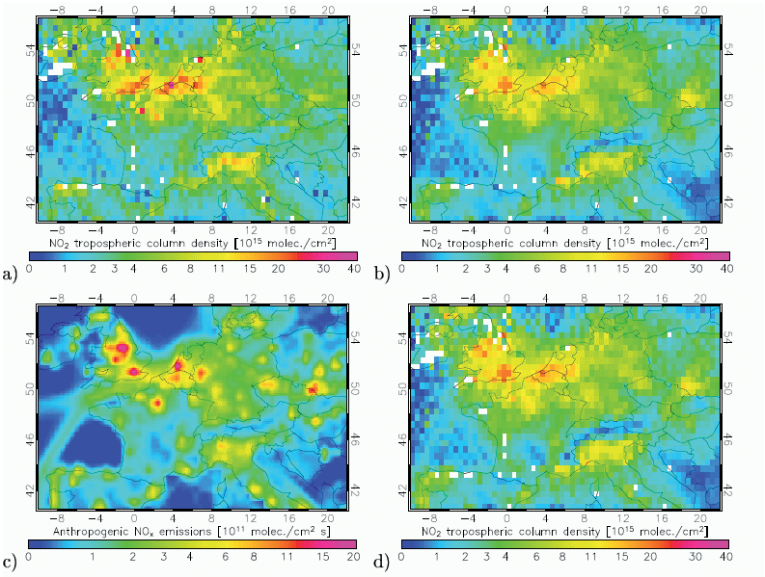

Figure 3. Comparisons between annual means of, a) NO_2 SCIAMACHY tropospheric columns (10^{15}molecules cm^{-2}), b) NO_2 CHIMERE tropospheric columns obtained by using the averaging kernels, c) emissions (EMEP) of nitrogen oxides (NO_x) over Western Europe for 10h00 UTC for 1998, and d) NO_2 CHIMERE tropospheric columns computed without using the averaging kernels. The emissions are derived from data given by EMEP, interpolated on the CHIMERE grid domain, unit 10^{11} molecules cm^{-2} s^{-1}.

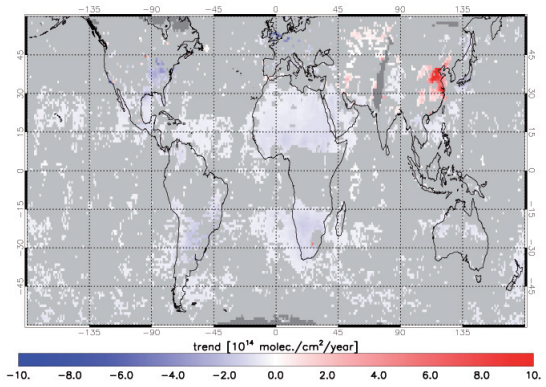

Figure 4. World map of the linear trend per year for tropospheric NO_2 in the period 1996 till 2005 derived from satellite observations by GOME and SCIAMACHY. For the light grey areas no significant trend has been found in the time series. For the dark grey areas not enough observations were available to construct a time series of tropospheric NO_2.

present and future satellite missions, in combination with a regional air quality model and surface data, will contribute to improve quantitative air quality analyses at a continental scale

The largest trend is found in Eastern China, where the economic growth is one of the fastest of the world. The fastest growing city with respect to both economy and tropospheric NO_2 is Shanghai. It is interesting to note that the growth in the region around Hong Kong is less than for other regions with a high economical activity. This is probably due to the already high level of economic activity in 1996 when our trend study started, and to a package of measures against air pollution in Hong Kong over the last years. Further results of this trend study are published by Van der A and co-authors[5].

Global implications

The fast growing emissions in China lead locally to rapidly increasing NO_2 concentrations, which affects the local ozone concentrations. Clearly these large increases will have severe consequences for the local air quality, but even effects on global scale can be expected, because the lifetime of tropospheric ozone is much larger than the lifetime of NO_2. Therefore, ozone can be transported over large distances by the wind. Using a chemical transport model the change in ozone due to increasing emissions in China can be calculated. Figure 5 shows increasing ozone concentrations in the Northern hemisphere caused by the growing Chinese emissions in the period 1997-2005. In this period of eight years the global averaged tropospheric ozone column has increased with 0.54 %[6]. The largest growth in tropospheric ozone we find in a plume reaching from China to the East along the direction of the prevailing winds. From the figure we conclude that the tropospheric ozone concentrations in the entire Northern hemisphere are increased due to the growing emissions in China. These increases seem small, but are still important. In Europe, the air pollution has been increased as a result of intercontinental transport. In addition, since ozone is a strong greenhouse gas, the effects on climate change cannot be neglected.

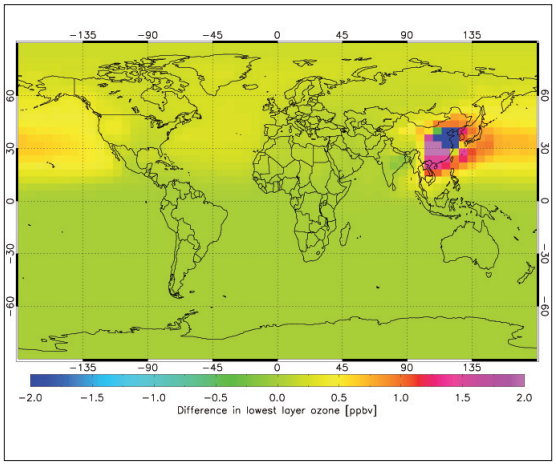

Figure 5. The difference in ground-level ozone caused by the increase of Chinese NO_x emissions between 1997 and 2005.

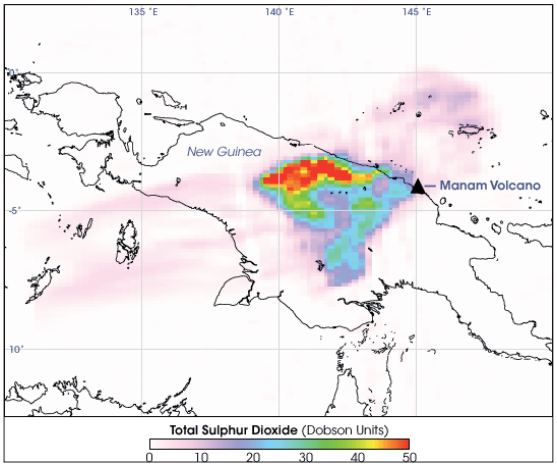

Figure 6. OMI observations of SO_2 from the eruption of the Manam volcano in New Guinea on 27 January 2005 (source: NASA).

Shanghai had a yearly increase of tropospheric NO_2 of about 29% since 1996

Volcanic eruptions

Volcanic eruptions may eject large amounts of ash (aerosols) and trace gases such as SO_2 into the atmosphere. These ejecta can have considerable impact on the safety of air traffic and on human health. Ground-based monitoring is carried out at only a limited number of volcanoes: most volcanoes, in particular remote ones, are not monitored on a regular basis. Global observations of SO_2 and aerosols derived from satellite measurements in near-real-time may therefore provide useful complementary information to assess possible impacts of volcanic eruptions on air traffic control and public safety. Observations of SO_2 are performed with UV-VIS satellite instruments such as GOME, SCIAMACHY and OMI. The technique used to retrieve the SO_2 column is called Differential Optical Absorption Spectroscopy (DOAS). Volcanic emissions and strong pollution events are clearly detected with this approach, which makes it very suitable for use in a near-real-time service, with an automatic warning system for exceptional SO_2 emission levels. Within the ESA projects TEMIS and PROMOTE this system provides information to the London and Toulouse VAAC (Volcanic Ash Advisory Centre), which issues warnings to the airline companies in case of observed volcanic ash or SO_2 clouds. The London and Toulouse VAAC are responsible for the air traffic in Europe, Africa and part of Asia.

Figure 6 shows the OMI observations of SO_2 from the eruption of the Manam volcano in New Guinea on 27 January 2005.

Conclusions

A decade of satellite observations of nitrogen dioxide in the atmosphere has been used to derive trends in anthropogenic emissions in China. As expected the nitrogen dioxide concentration is growing most rapidly in Eastern China, where the economic growth is largest. By feeding the derived trends to a global chemical transport model of the atmosphere the effects on the concentrations of world-wide tropospheric ozone can be determined. According to the model the background concentration of ozone has increased in the entire northern hemisphere as a result of the growing emissions in China. Another trace gas observed by satellites is SO_2, which occurs in large quantities in areas with large air pollution or with volcanic eruptions. Observation of these volcanic eruptions in near-real time helps the Volcanic Ash Advisory Centres in warning airline companies for potentially dangerous areas.

1) Eskes, H.J. and K.F. Boersma, 2003. *Averaging Kernels for DOAS total-column satellite retrievals.* Atm. Chem. Phys., **3**, 1285 – 1291.
2) Boersma, K.F., H.J. Eskes and E.J. Brinksma, 2004. *Error analysis for tropospheric NO_2 retrieval from space.* J. Geophys. Res., **109**, 4311. doi: 10.1029/2003JD003961
3) Boersma, K.F., 2005. *Satellite observations of tropospheric nitrogen dioxide; retrieval interpretation and modelling,* PhD Thesis, Universiteitsdrukkerij Technical University Eindhoven, Eindhoven, The Netherlands.
4) Blond, N., K.F. Boersma, H.J. Eskes, R.J. van der A, M. van Roozendael, I. De Smedt, G. Bergametti and R. Vautard, 2007. *Intercomparison of SCIAMACHY nitrogen dioxide observations, in-situ measurements, and air quality modeling results over Western Europe.* J. Geophys. Res, **112**, D10311. doi: 10.1029/2006JD007277
5) A, R.J. van der, D.H.M.U. Peters, H.J. Eskes, K.F. Boersma, M. van Roozendael, I. de Smedt and H.M. Kelder, 2006. *Detection of the trend and seasonal variation in tropospheric NO_2 over China.* J. Geophys. Res., **111**, D12317, doi:10.1029/2005JD006594
6) Kuenen, J.J.P., 2006. *Anthropogenic NOx emission estimates for China based on satellite measurements and chemistry-transport modeling,* KNMI Technical Report TR-288, 62pp.

Scientific highlights of SCIAMACHY and OMI

Pieternel Levelt, Piet Stammes, Mirna van Hoek, Martin de Graaf, Ben Veihelmann and Ping Wang

Introduction

The Netherlands are actively involved in atmospheric composition measurements from space since 1995 with measurements from the GOME, SCIAMACHY and OMI satellite instruments. The MetOp satellite series with GOME-2 onboard will continue these measurements until 2020, thereby providing an important global climate data record. KNMI plays an active and often leading role in the analysis of measurements from these instruments. Here we describe some scientific highlights based on SCIAMACHY and OMI data.

Scientific highlights of SCIAMACHY

SCIAMACHY, launched on board of ESA's Envisat satellite in 2002, is a spectrometer covering the spectral range from 240 to 2380 nm with nadir and limb view capabilities. SCIAMACHY has been developed in collaboration between Germany, The Netherlands and Belgium. It not only measures UV-visible absorbing gases, like O_3, NO_2, SO_2, but also near-IR absorbing gases, like CO_2, CH_4 and CO. The spatial resolution is 30 km x 60 km in the UV-visible, and 30 km x 240 km in the near-IR; in 6 days the entire Earth is covered. With SCIAMACHY already many unique scientific results have been obtained, like global maps of NO_2, which is an air pollutant, and CH_4, which is an important greenhouse gas. These results are presented by Van der A and Kelder, and by Van Weele, elsewhere in this report.

In the period 2005-2006 the SCIAMACHY operational and scientific data products have been validated and matured. A special issue of Atmospheric Chemistry and Physics in 2005 was dedicated to the SCIAMACHY validation. The validation of the SCIAMACHY data products is being coordinated by KNMI (see: *http://www.sciamachy.org*). In The Netherlands, SRON and KNMI collaborate closely for the calibration, validation and exploitation of SCIAMACHY data. The SCIAMACHY results produced in The Netherlands are available at the TEMIS website (*http://www.temis.nl*), the SCIAMACHY data center (*http://neonet.knmi.nl*), and partly at the KODAC database (*http://kodac.knmi.nl/kodac*). Below we focus on two data products from SCIAMACHY, namely clouds and aerosols.

Cloud detection using oxygen

Detection of clouds from SCIAMACHY and OMI measurements is important for two reasons: (i) clouds affect the detection of trace gases, and (ii) clouds are an important component in the climate system because of their effects on the radiation balance and their role in the hydrological cycle. For SCIAMACHY, GOME and GOME-2 we use the reflectance inside and outside the absorption band of oxygen at 760 nm (the O_2 A-band) to detect the pressure and fractional cover of clouds, respectively. For OMI we use the oxygen absorption band at 477 nm. Since oxygen is well-mixed the detected amount of oxygen is a direct measure for the pressure of clouds. From radiative transfer simulations and comparisons with other cloud height detection techniques, it appears that cloud pressure retrieval using oxygen absorption at visible wavelengths produces the pressure of the middle of the cloud. The algorithm which uses the O_2 A-band is called FRESCO (Fast Retrieval Scheme for Clouds from the Oxygen A-band). This algorithm has been developed at KNMI since about 2000[1,2,3]. The algorithm fits the measured O_2 A-band under the assumption that clouds are Lambertian reflectors with a high albedo.

In Figure 1 the frequency distribution of globally and monthly averaged cloud pressures from SCIAMACHY is shown for 2002. The figure shows a superposition of two modes in the distribution of global cloud pressure: one mode at about 500 hPa (high clouds) and one at about 850 hPa (low clouds). These two modes are not seen in the data from the International Satellite Cloud Climatology Project (ISCCP), which is based on thermal IR satellite data. Apparently, the optical O_2 A-band cloud pressures behave differently from IR cloud pressures, which are more dominated by high thin clouds, like cirrus. The SCIAMACHY results agree well with GOME results using the same FRESCO algorithm. This means that we can make a continuous cloud data record from the two instruments.

Aerosol detection above clouds

Aerosols are important for climate, because of their effects on the radiation balance and their influence on cloud formation. The unique aspect of UV-visible spectrometers like SCIAMACHY and OMI is the capability of detecting absorbing aerosols, like desert dust and smoke, over ocean and land, which are both dark in the UV. Even in the presence of clouds the UV technique of detection of absorbing aerosols works

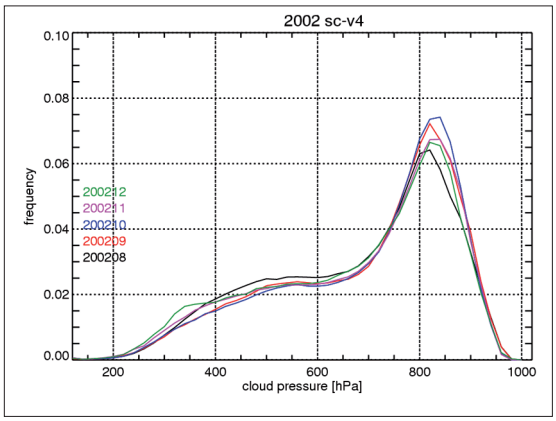

Figure 1. Global frequency distribution of cloud pressure from SCIAMACHY using the FRESCO O_2 A-band algorithm for five months of 2002. Note the bimodal shape, with modes at about 850 hPa and 500 hPa.

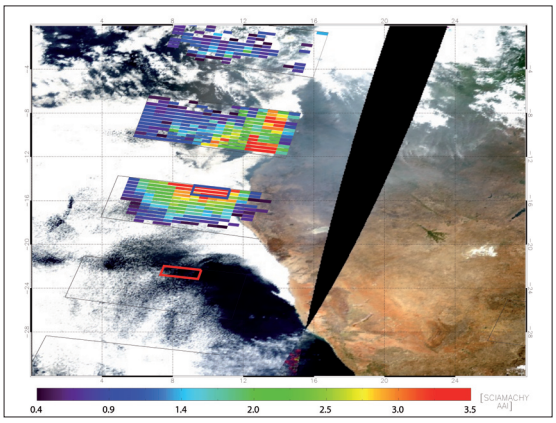

Figure 2. Biomass burning event over Africa, as detected by MODIS imagery (underlying picture) and by the SCIAMACHY absorbing aerosol index (overlying data blocks). The absorbing aerosol index (AAI) can detect absorbing aerosols even over clouds, since it does not use the brightness but the colour of the scene in the UV.

The unique aspect of UV-visible spectrometers like SCIAMACHY and OMI is the capability of detecting absorbing aerosols

well. Most satellite imagers, like MODIS, cannot detect aerosols in bright cloudy scenes. However, when using the UV spectrum the so-called Absorbing Aerosol Index (AAI) can be determined which indicates UV-absorbing aerosols. The AAI is the colour of the scene in the UV (at 340-380 nm) as compared to the colour of a purely Rayleigh scattering atmosphere. An example is shown in Figure 2, where the SCIAMACHY AAI is shown on top of a MODIS image of biomass burning aerosol off the west coast of Africa[4,5]. The reflectance spectrum of a cloudy pixel with smoke on top of it is shown in Figure 3, which illustrates the deviation in the spectral shape of the polluted pixel.

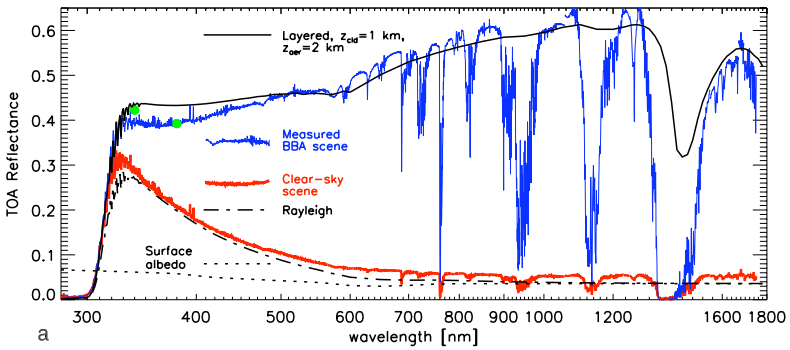

Figure 3. Reflectance spectra of a biomass burning aerosol (BBA) scene with clouds and a clear sky scene, measured by SCIAMACHY (see Figure 2). The absorbing aerosols cause a much lower reflectance in the UV-visible part of the spectrum as compared to a normal cloudy scene, which is spectrally flat. The measured spectrum can be simulated (solid line) by assuming a thin layer of absorbing aerosols (optical thickness τ=0.3) on top of a non-absorbing cloud (τ =20).

Scientific highlights of the Ozone Monitoring Instrument

The Ozone Monitoring Instrument (OMI) is a UV/VISIBLE nadir solar backscatter spectrometer onboard NASA's EOS-Aura satellite, which was launched in July 2004. OMI measurements constitute a major contribution to our understanding of ozone trends, the global impact of air pollution and the interaction between atmospheric chemistry and climate by virtue of the unique capability of measuring important trace gases with daily global coverage and a small footprint (13 km × 24 km at nadir)[6,7]. OMI measures trace gases including O_3, NO_2, SO_2, HCHO, BrO and OClO as well as aerosols, clouds, and UV irradiance at the surface. All anticipated OMI algorithms have been published and the products are produced operationally. Most products are publicly available via the NASA Data and Information Services Center (http://disc.gsfc.nasa.gov/Aura/OMI). Currently the final round of a large

validation effort takes place, which will result in a special issue of the Journal of Geophysical Research on Aura validation to be published in 2007.

OMI monitors high-latitude ozone depletion events and the stratospheric ozone recovery predicted by chemical models. Figure 4 shows the high-latitude ozone record measured by various satellite instruments including the Total Ozone Mapping Spectrometer (TOMS). This time series is continued by OMI's ozone measurements starting from the year 2005. OMI's ozone measurements have been delivered to the IPCC[8]. OMI's high spatial resolution enables monitoring of tropospheric pollution including four of the US EPA's (Environmental Protection Agency) criteria air pollutants. Below, we discuss two OMI products developed by KNMI, namely nitrogen dioxide and aerosols.

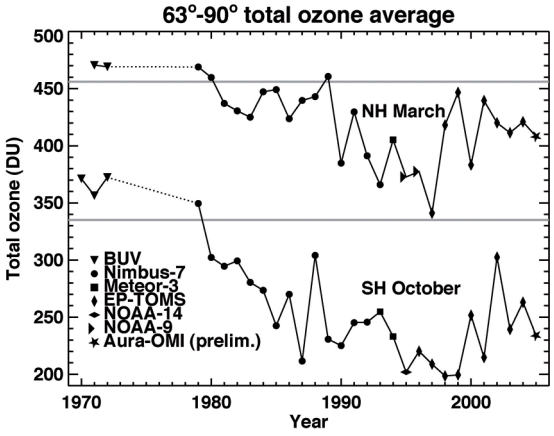

Figure 4. Average column ozone poleward of 63° latitude in the springtime of each hemisphere (March for the NH and October for the SH), in Dobson units, based on data from various satellite instruments as indicated. The figure is updated from the IPCC/TEAP Special Report 2005 by including the data points for 2006 from OMI measurements.

Air Pollution above the Netherlands measured by OMI

KNMI developed a tropospheric nitrogen dioxide product from OMI measurements which can be run in Near-Real-Time (NRT). NO_2 is a well known

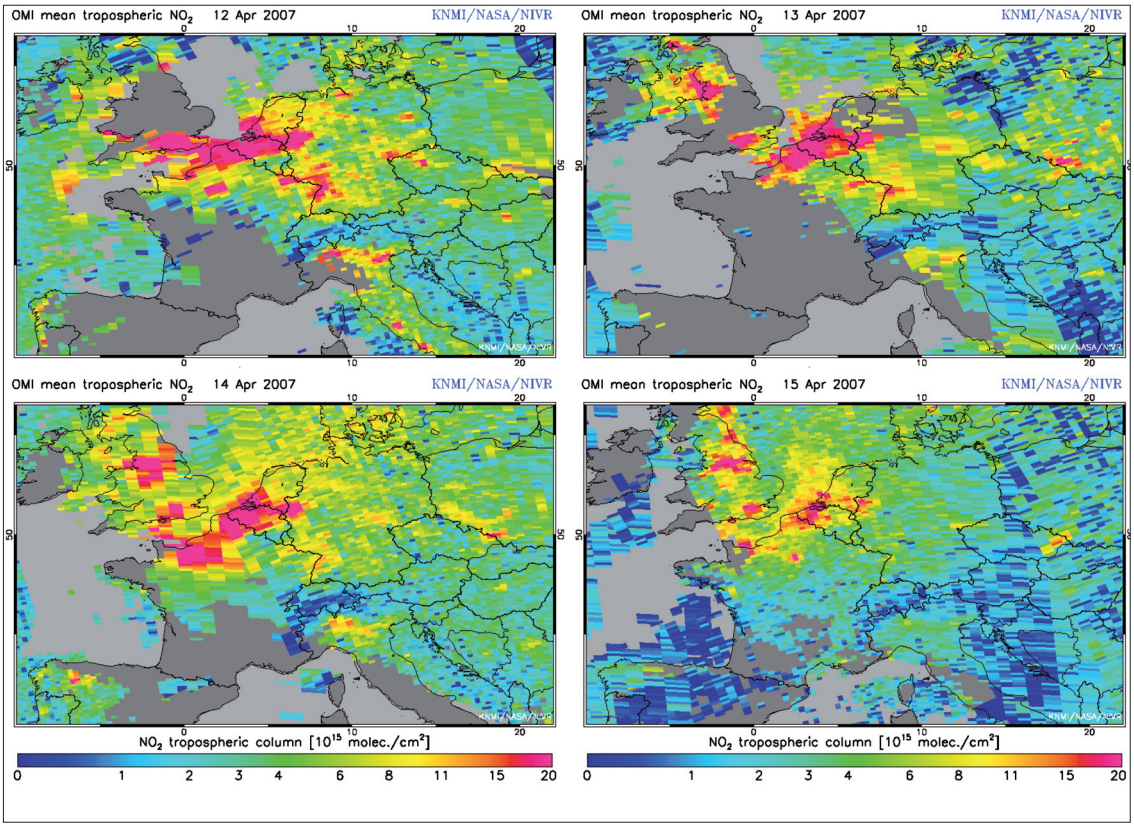

Figure 5. Tropospheric NO_2 observations by OMI for 12-15 April 2007. High concentrations of NO_2 are observed for densely populated areas such as the Randstad and the Ruhr area. On Sundays (e.g. 15 April 2007, lower right panel) the concentration of NO_2 is significantly lower due to the less road traffic.

The high spatial resolution from OMI enables for the first time detection of air pollution at urban scales on a daily basis with global coverage

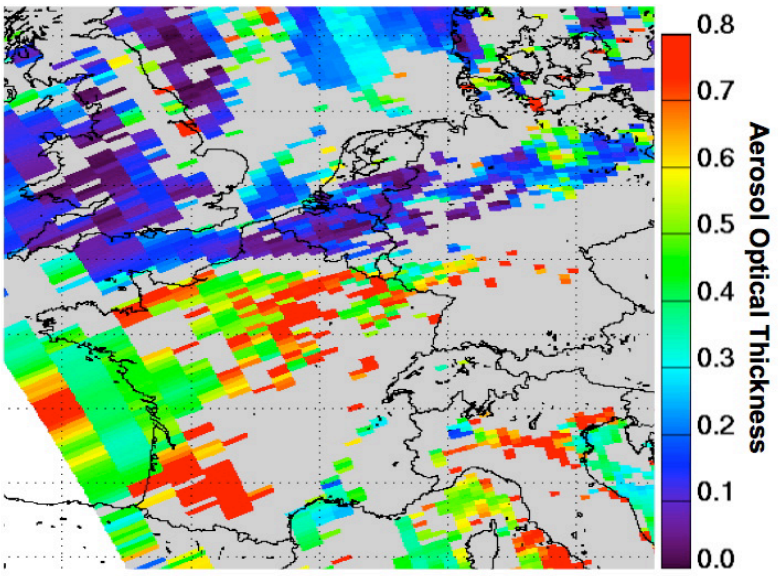

Figure 6. Aerosol optical thickness retrieved from OMI measurements using the multi-wavelength algorithm. The strong contrast between clean air over England, Benelux and North Germany and aerosol loaded air further south has been observed as well by other aerosol sensors.

atmospheric pollutant, of which in The Netherlands 60 % is produced by road traffic. NO_2 also plays a prominent role as precursor of the air pollutant tropospheric ozone. The NRT products are available within 3 hours after measurement on the TEMIS website (*http://www.temis.nl*) and are part of the air quality forecast developed by KNMI, RIVM and TNO. The algorithm was already developed for SCIAMACHY NO_2 retrieval and has been adapted to OMI[9]. The high spatial resolution from OMI is unprecedented in atmospheric composition measurements from space and enables for the first time detection of air pollution at urban scales on a daily basis with global coverage. In Figure 5 a set of OMI measurements of nitrogen dioxide is shown for continuous cloud-free days above The Netherlands. These measurements were taken during the earliest days with summertime temperatures in The Netherlands ever recorded. High temperatures in combination with low wind-speeds lead to the formation of smog, which can be seen in the high NO_2 values. Also the characteristic low NO_2 on Sunday, April 15, due to less traffic, is clearly visible.

OMI's high spatial resolution increases the likelihood of observing cloud-free scenes which facilitates the monitoring of tropospheric pollution. Whereas OMI can measure day-to-day variations in NO_2, GOME and SCIAMACHY are limited to monthly or yearly averages of NO_2 pollution because of their low spatial resolution and limited coverage. Also high regional dependency of pollution can be seen by OMI, as is shown in Figure 5.

New aerosol algorithm from OMI improves distinction of aerosol type

A multi-wavelength aerosol algorithm has been developed at KNMI to retrieve aerosol properties from OMI spectral reflectance measurements. This algorithm uses spectral information from both the visible and the UV parts of the spectrum, which improves the distinction between weakly absorbing aerosols, biomass burning aerosols and desert dust aerosols. In particular desert dust aerosols can be distinguished from other aerosol types due to the strong absorption of mineral dust in the UV. The multi-wavelength algorithm provides information about the aerosol optical thickness, which is a measure of the amount of aerosols, and the aerosol type[10]. Aerosol climate forcing depends strongly on the aerosol radiative effect as well as on aerosol-cloud interactions, which can differ significantly for different aerosol types. In Figure 6 the retrieved aerosol optical thickness is shown for Central Europe for July 14, 2006. The strong contrast on that day between clean air over England, the Benelux and Northern Germany, and aerosol loaded air further south was verified by ground based measurements. In conclusion, the new aerosol product from OMI will provide information on the tropospheric composition useful for climate and air quality monitoring.

1) Koelemeijer, R.B.A., P. Stammes, J.W. Hovenier and J.F. de Haan, 2001. *A fast method for retrieval of cloud parameters using oxygen A band measurements from GOME.* J. Geophys. Res., **106**, 3475-3490.
2) Fournier, N., P. Stammes, M. de Graaf, R. van der A, A. Piters, M. Grzegorski and A. Kokhanovsky, 2006. *Improving cloud information over deserts from SCIAMACHY Oxygen A-band measurements.* Atmos. Chem. Phys., **6**, 163-172. http://www.copernicus.org/EGU/acp/acp/6/163/acp-6-163.htm.
3) Wang, P., P. Stammes, N. Fournier and R. van der A, 2006. *Fresco+: An Improved Cloud Algorithm for GOME and SCIAMACHY.* Proc. Atmospheric Science Conf., ESRIN, Frascati Italy. H. Lacoste and L. Ouwehand, (Eds), ESA SP-628.
4) Graaf, M. de, 2006. *Remote sensing of UV-absorbing aerosols using space-borne instruments.* PhD Thesis, Vrije Universiteit, Amsterdam, The Netherlands.
5) Graaf, M. de, P. Stammes and E.A.A. Aben, 2007. *Analysis of reflectance spectra of UV-absorbing aerosol scenes measured by SCIAMACHY.* J. Geophys. Res., **112**, D02206. doi:10.1029/2006JD007249
6) Levelt, P.F., E. Hilsenrath, G.W. Leppelmeier, G.H.J. van den Oord, P.K. Bhartia, J. Tamminen, J.F. de Haan and J.P. Veefkind, 2006. *Science Objectives of the Ozone Monitoring Instrument.* IEEE Transactions on Geoscience and Remote Sensing, **44**, No.5, 1199-1208.
7) Levelt, P.F., G.H.J. van den Oord, M.R. Dobber, A. Mälkki, H. Visser, J. de Vries, P. Stammes, J.O.V. Lundell and H. Saari, 2006. *The Ozone Monitoring Instrument.* IEEE Transactions on Geoscience and Remote Sensing, **44**, No.5, 1093-1101.
8) IPCC/TEAP Special Report, 2005. *Safeguarding the ozone layer and the global climate system: Issues related to the hydrofluorocarbons and perfluorcarbons,* Summary for Policy Makers. WMO/UNEP.
9) Boersma, K.F., H.J. Eskes, J.P. Veefkind, E.J. Brinksma, R.J. van der A, M. Sneep, G.H.J. van den Oord, P.F. Levelt, P. Stammes, J.F. Gleason and E.J. Bucsela, 2006. *Near-real time retrieval of tropospheric NO_2 from OMI.* Atm. Chem. Phys., **7**, 2103-2118.
10) Veihelmann, B., P.F. Levelt, P. Stammes and J.P. Veefkind, 2007. *Simulation study of the aerosol information content in OMI spectral reflectance measurements.* Atmos. Chem. Phys., **7**, 3115-3127.

Recovery and disclosure of historical meteorological observations (Hisklim)

Theo Brandsma

Introduction

In the year 2000 KNMI started a programme on data rescue, digitising and time series homogenisation, named Hisklim[1)] (*htpp://www.knmi.nl.onderzk/hisklim*). The aim of the programme is to make historical land and sea climate data from Dutch sources digitally accessible, with the highest possible time resolution and quality. The data extend back into the 17th century and stem from a variety of ship and station observations (see Figure 1 for the main types of data and time periods covered by Hisklim). The resulting high-quality datasets are needed to properly assess climate change and variability. Moreover, the datasets are also required to validate climate models. The output of these models is the basis for the development of climate change policies and climate scenarios for the 21st century, which are increasingly being used in climate change impacts and adaptation studies. All historical data disclosed by Hisklim is freely available for research, engineering, and the general public from the KNMI website at *http://www.knmi.nl/klimatologie*.

In the first part of this chapter we present examples of the digitisation projects. Digitisation is a labour-intensive task that needs to be carried out with care. Figure 2 shows a specimen of an 18th century

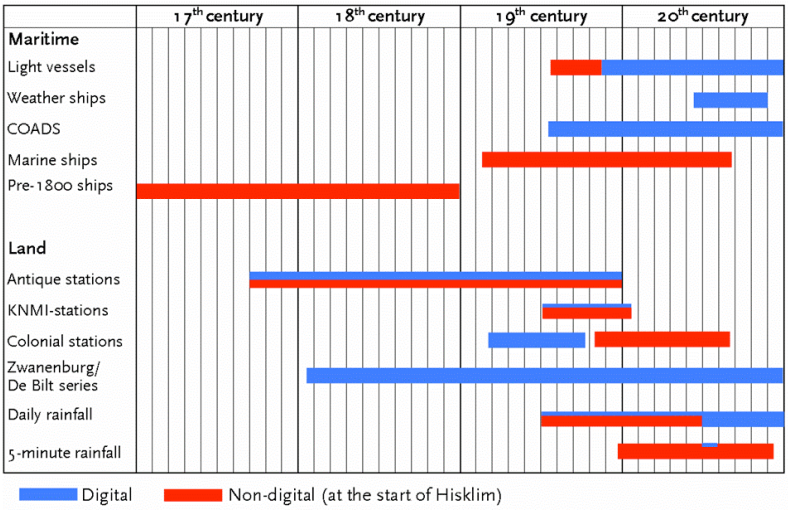

Figure 1. Types of data and time periods covered by Hisklim.

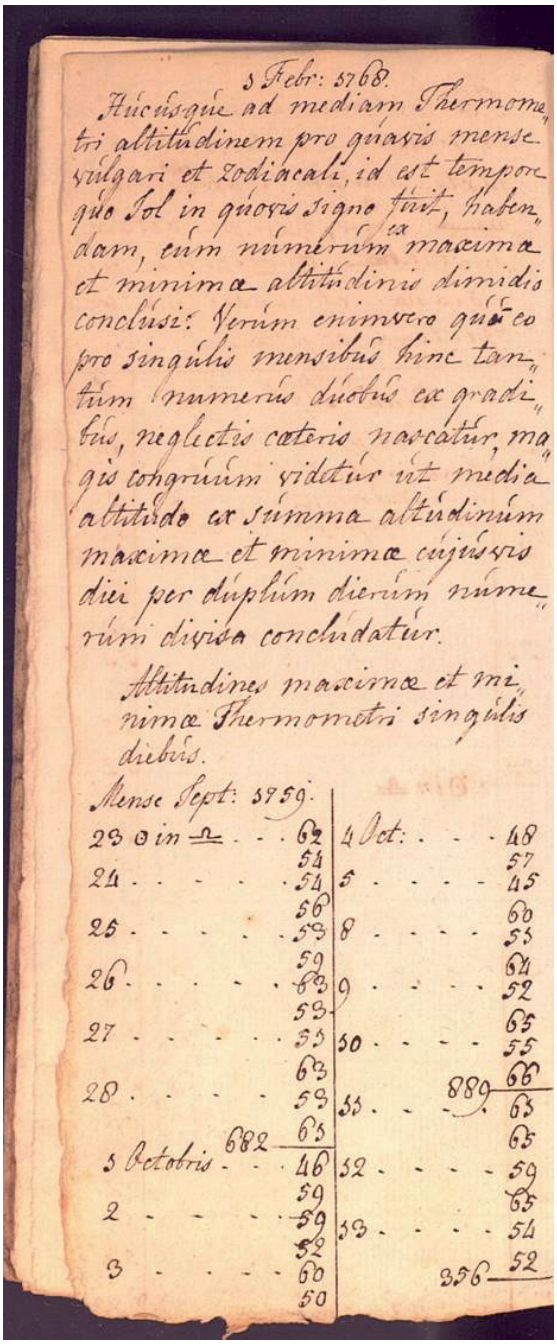

Figure 2. Specimen from the weather diary of Jan Carel van der Muelen. The weather observations (partly in Latin) and measurements are taken partly in Utrecht and partly in Driebergen and cover the period 1759–1810.

hardcopy data source available in the archive of KNMI. This kind of data is digitised by making an electronic copy (jpeg-images), which is used to type the data into a spreadsheet. Both the images and the data are made accessible via the internet. The work is embedded internationally: from 2001-2004 the digitisation of pre-1850 ship logs got a boost from the KNMI participation in the EU-funded project CLIWOC (Climatological Database for the World's Oceans 1750-1850; (*http://www.knmi.nl/cliwoc*). From March 2005 until March 2009, part of the work is being funded through the KNMI participation in the National project Climate changes Spatial Planning (*http://www.klimaatvoorruimte.nl*).

In the second part of the chapter, we present some examples of current work on homogenisation of climatological time series and datasets. Inhomogeneities result from e.g. changes in instrumentation, repositioning of instruments (both horizontally and vertically), changes in the surroundings like the growth of trees and the expansion of cities, and changes in measurement practices. We focus on improving homogenisation methods by studying the weather-dependence of inhomogeneities. An important goal is to obtain a homogeneous version of the so-called Zwanenburg/De Bilt subdaily temperature time series that covers the period 1706 until present. The digitisation efforts presented here are partly meant to obtain parallel time series for homogenising that series. To address deficiencies in present-day homogenisation methods, an EU COST action ES0601 (*http://www.cost.esf.org/*) started in 2007. KNMI participates in this action.

Digitisation

KNMI yearbooks
The 19th century KNMI yearbooks are an important source of information. The meteorological observations in these books constitute a crucial link between the pre-1850 measurements (before the founding of KNMI) and the modern post-1900 observations. The observations consist of (mostly) three measurements a day of air temperature, air pressure, humidity, wind speed and direction, cloudiness, and of daily measurements of precipitation of a varying number of stations (23 in total) distributed across the Netherlands. In the year 2006 we completed the digitisation of these data. About 0.6 million records (550 station-years) were digitised and quality controlled. About 40% of the data is now available via the KNMI website and the remainder will become available in 2007.

Amsterdam City Water Office
From about the year 1675 onwards, the Amsterdam City Water Office was responsible for the water management of the canals in the city. At that time, Amsterdam was situated along the open sea, and the canals in the city, which also served as sewer system, had to be flushed using the tide. Meteorological measurements were made by employees of the office to support this work. These measurements are unique in the sense that in the 1784-1963 period the measurements were taken hourly. In the beginning air temperature, windspeed and direction were measured. From 1824 onwards, air pressure was added. In the 1784-1963 period, the office moved three times to a new location. The handwritten observer logbooks were put on microfilms in 1984 by the Amsterdam City Archive and KNMI obtained a copy. Recently, we transformed the films into jpeg-images which were subsequently used as a basis for digitizing all 1.6 million observations. The first part of the work was finished in 2004[2)], the second part, including Quality Control (QC), in 2006. In 2007 the data will become available.

Daily rainfall 1850-1950
KNMI measures daily rainfall since about 1850. In the 1850-1950 period, the network gradually increased to its present density of about 300 rain gauges. The measurements are taken by voluntary observers every morning. In the first decade of the 20th century a standardization of the measurements was implemented. In contrast to the post-1950 period, where all observations are digitally available, only about 10% of the observations were digitally available in the 1850-1950 period. In the years 2005 and 2006 we digitized all pre-1951 daily data, amounting to about 4.7 million observations (13500 station-years). It took two man-years of typing in the data. The data will become available in 2008 after QC and homogeneity testing.

Rainfall strip charts and paper rolls
Self-recording rain gauges (Figure 3) have been

Figure 3. Specimen of a self-recording rain gauge (without lid).

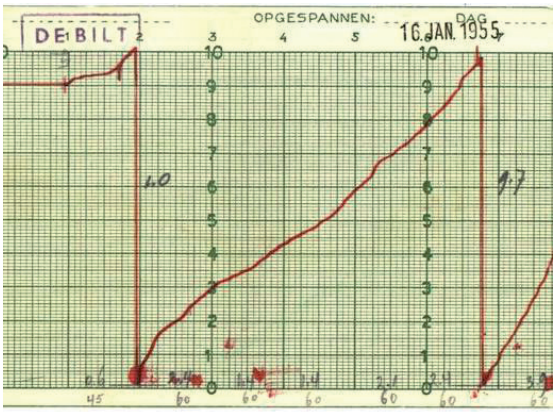

Figure 4. Part of the rainfall strip chart of De Bilt of 16 January 1955.

applied for continuous rainfall measurements at a selected set of KNMI stations since the end of the 19th century. At first, rainfall was recorded on daily (Figure 4) and sometimes weekly rainfall strip charts. Thereafter, from about 1980 through 1993, paper rolls were used to register rainfall for about 10-20 days per roll. From 1994 onwards, rainfall measurements are transferred electronically and operationally stored at 10-minutes resolution (for some selected stations at 1-minute resolution). Until now, the strip charts and paper rolls have been used mainly for extracting hourly values. In infrastructural design (e.g. sewer systems, tunnel drainage) there is, however, a need for long rainfall series with much higher resolution than 1 hour. Fortunately, the charts and rolls can be used to extract rainfall with a time resolution of about 5 to 10 minutes.

We are developing a procedure that largely automates the labor-intensive extraction work for rainfall strip charts and paper rolls. Although developed for rainfall, it can be applied to other elements as well. The procedure consists of four basic steps: (1) scanning of the charts and rolls to high-resolution digital images, (2) applying automatic curve extraction software in a batch process to determine the coordinates of cumulative rainfall lines on the images, (3) visually inspecting the results of the curve extraction, (4) post-processing of the curves that were not correctly determined in step (3). Although KNMI is still perfecting the software, several tens of station-years have succesfully been digitised. The time resolution is about 5 minutes. In total 321 station-years are being digitised using the stations De Bilt, Eelde, Den Helder/De Kooy, Vlissingen, Beek and Amsterdam. When the digitisation is completed, the number of station-years with digital 5-minute rainfall series will be increased by a factor of 25. The data will become available in 2009.

Homogenisation and quality control

Thermometer screen intercomparison

Thermometer screens protect thermometers against unwanted impacts like direct or indirect radiation and rainfall. On the other hand, the screens may complicate the measurement of the real air temperature by restriction of the air flow and self-heating. To obtain a homogeneous version of the Zwanenburg/De Bilt temperature series (1706 until present), it is therefore important to know and understand the effects of changes in thermometer screens. One of our activities to study this topic has been to reanalyse the results of a thermometer screen intercomparison that took place at the KNMI terrain in the period 1989-1995. The objective of the analysis was to obtain weather-dependent corrections for past changes in screen types[3,4]. Ten screens (Figure 5) were compared. All were equipped with fast-responding sensors. Figure 6 presents an example of inter-screen temperature differences for the summer. For some of the screens, the figure clearly shows that the differences strongly depend on the weather. Despite the sometimes large temperature differences on specific days, the annual

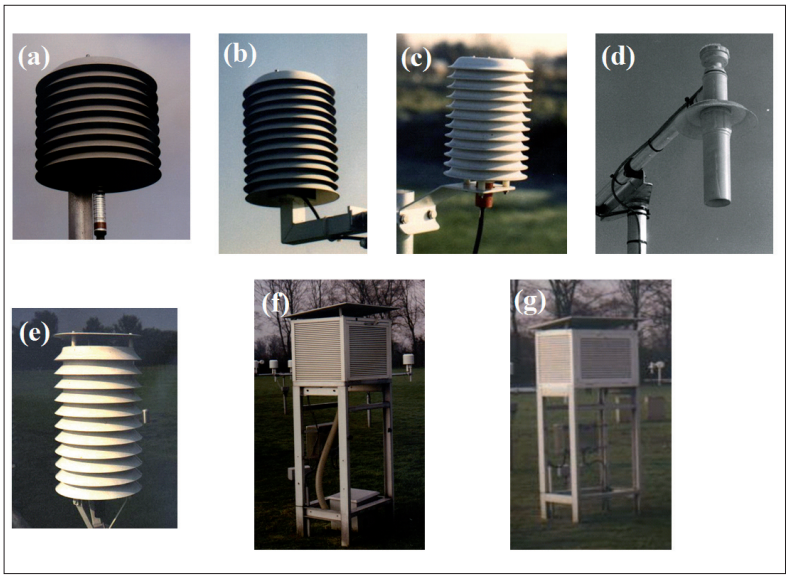

Figure 5. Overview of screens used in the comparison: (a) KNMI multi-plate, (b) Vaisala multi-plate, (c) Young Gill multi-plate, (d) Young aspirated, (e) Socrima multi-plate, (f) Stevenson PVC, and (g) Stevenson wood. Screens (a) and (f) have an aspirated and natural ventilated version. The natural ventilated version of (a) is the present operational screen and acts as the reference Knmi.ref.

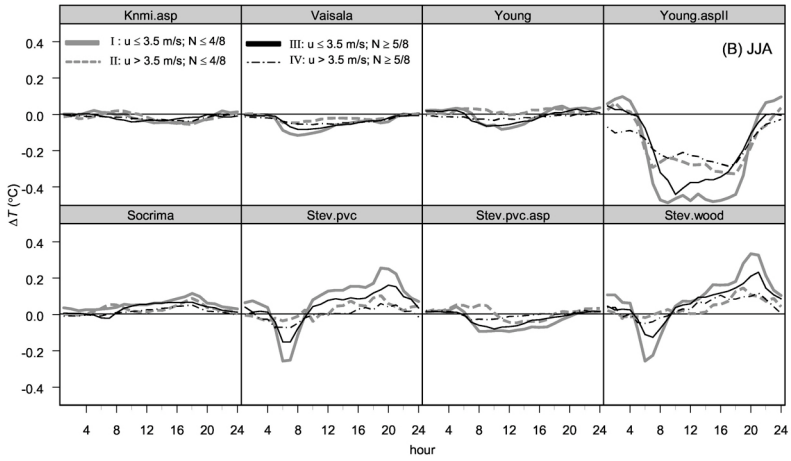

Figure 6. Mean diurnal cycles of the hourly temperature differences ΔT (screen – Knmi.ref) for four combinations of windspeed (u) and fraction of cloudiness (N) for the three summer months (JJA) for the eight screens.

mean differences for daily maximum, minimum and mean temperature rarely exceed 0.1°C. The strongly aspirated Young screen (Young.aspII) is an exception, with annual mean maximum temperatures 0.28°C below the reference. Comparison of modern-day screens with older (e.g. 19th century) screens, however, reveals annual mean differences of the order of 1.0°C[5]. For a transition of the natural ventilated synthetic Stevenson screen to the present round-shaped multi-plate operational screen, we successfully developed transfer functions. These functions may be used for correcting inhomogeneities in times series resulting from screen changes.

Site intercomparison

Besides the effects of screen changes on tempera - ture measurements, it is also important to know the impact of changes in the location of the screen. We therefore compared five temperature measurement sites at the KNMI terrain in De Bilt[6] (see Figure 7), among others the current operational site (DB260), an intended future operational site (Test4) and the site that was used around 1950 (Test1). From May 2003 through June 2005, temperature and wind speed were measured simultaneously at these locations at a height of 1.5 m. Temperature differences are most evident during clear-sky night-time conditions with low windspeeds. Figure 8 shows the mean differences in minimum temperature relative to the Test4 site. Note the relatively large negative values in and around the summer months of 2003 and 2004 for the DB260, Test2 and Test3 sites. Due to a renovation of the nature area west of DB260 in October 2004, the values of these sites in 2005 are close to zero. The results are important for assessing and understanding the impact of past repositionings and for deciding upon a repositioning of the present operational temperature site.

Development of homogenisation techniques

Homogenisation of climate time series and datasets with a daily resolution is a relatively new field of research. We contributed to that research by introducing nearest-neighbour resampling for homogenizing temperature records on a daily to sub-daily level[7]. We developed the method to obtain daily mean and sub-daily temperatures from time series subject to irregular observation frequencies and changing observation schedules. This is especially important when we connect the De Bilt series to the older parts of the Zwanenburg/De Bilt series. The method resamples diurnal temperature cycles from an observed hourly temperature sub-record at the station. Unlike other methods, the technique maintains the variance in a natural way. This is especially important for the analysis of trends and variability of extremes. Nearest-neighbour resampling can successfully be performed, even in situations were the length of the hourly sub-record is an order of magnitude smaller than the length of the series to be homogenized.

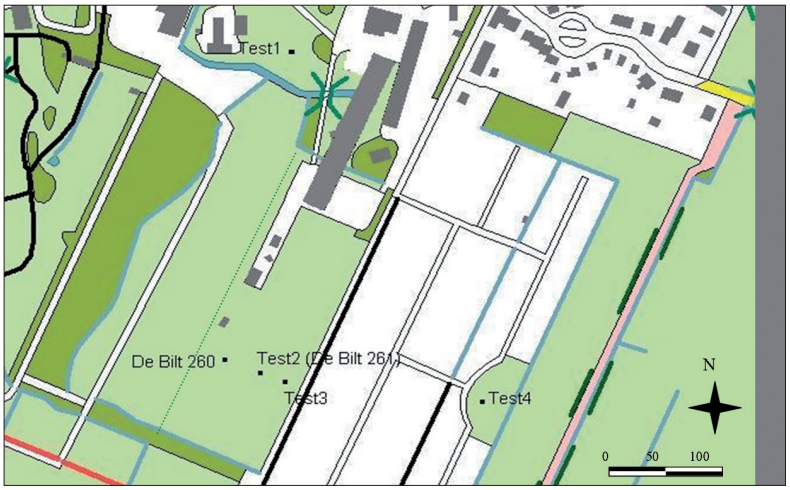

Figure 7. Locations of the screens at the KNMI terrain in De Bilt. Light green is grass cover and dark green trees. The white area that runs from mid bottom to top right consists mainly of vegetable gardens. The KNMI buildings are in gray (left from the vegetable gardens).

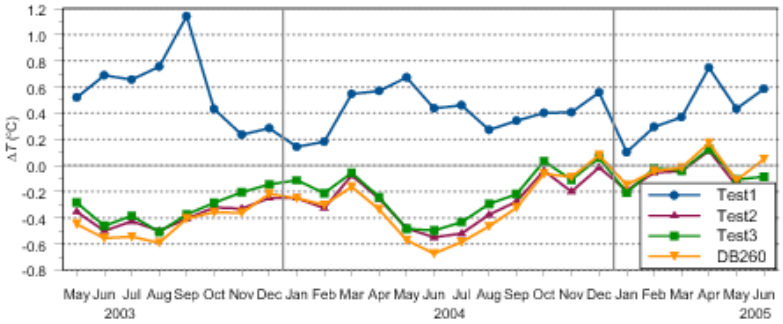

Figure 8. Mean monthly temperature difference ΔT with reference to Test4 for the daily minimum temperature.

Outlook

Our digitisation efforts will continue in the next years. Besides the activities mentioned above, we are also digitising the data from the former Dutch colonies and the remaining part of the old pre-1850 measurements in the Netherlands. Furthermore, from the remainder of the ship logs at KNMI we made digital images that have been sent for digitisation to the US, where funds and labour are available for that work. To support the QC and homogenisation work, we are making digital images of the complete hardcopy metadata archive at KNMI. The images facilitate the digitisation of metadata relevant for homogenisation studies.

The work on the homogenzation of the daily Zwanenburg/De Bilt temperature time series will also continue. A first release of the homogized temperature time of the De Bilt series is available at *htpp://www.knmi.nl/klimatologie* for monthly values. As part of the homogenisation efforts, we also study the effect of urban warming on the temperature measurements in De Bilt. After an initial statistical study[8], we are now performing mobile temperature measurements in a transect containing Utrecht and De Bilt for a period of about one year. Besides temperature, we are also working on pressure observations. We recovered a 17th century series of daily air pressure readings from Leiden (1697-1698)[9]. This is one of the very few pressure series that extend back into the 17th century that may help to reconstruct the daily atmospheric circulation for Western Europe in that period. We are also working on a homogeneous daily air pressure time series for the Netherlands (1712 until present). Finally, we are contributing to the QC of the maritime US Maury collection.

Together with other international efforts similar to Hisklim, the work presented here will help to place the current climate in the right historical perspective.

1) Brandsma, T., F. Koek, H. Wallbrink and G.P. Können, 2000. *Het KNMI-programma Hisklim (HIStorisch KLIMaat)*. KNMI Publication 191, also Hisklim 1, 72 pp.
2) Riepma, H.W., 2004. *DIGISTAD, Digitaliseren Stadswaterkantoor.* KNMI-Memorandum, also Hisklim 6, 26 pp.
3) Meulen, J.P. van der and T. Brandsma. *Thermometer Screen Intercomparison in De Bilt (the Netherlands), Part I: Understanding the weather-dependent temperature differences.* Int. J. Climatology., in press.
4) Brandsma, T. and J.P. van der Meulen. *Thermometer Screen Intercomparison in De Bilt (the Netherlands), Part II: Description and modeling of mean temperature differences and extremes.* Int. J. Climatology, in press.
5) Parker, D.E., 1994. *Effects of changing exposure of thermometers at land stations.* Int. J. Climatology, 14, 11, 1–31.
6) Brandsma, T., 2004. *Parallel air temperature measurements at the KNMI-terrain in De Bilt (the Netherlands)* May 2003 - April 2005 (interim report). KNMI Publication 207, also Hisklim 7, 29 pp.
7) Brandsma, T. and G.P. Können, 2006. *Application of nearest-neighbour resampling techniques for homogenizing temperature records on a daily to sub-daily level.* Int. J. Climatology, **26**, 1, 75-89. doi:10.1002/joc.1236
8) Brandsma, T., G.P. Können and H.R.A. Wessels, 2003. *Empirical estimation of the effect of urban heat advection on the temperature series of De Bilt (The Netherlands)*. Int. J. Climatology, **23**, 7, 829-845, doi: 10.1002/joc.902
9) Können, G.P. and T. Brandsma, 2005. *Instrumental pressure observations from the end of the 17th century: Leiden (The Netherlands)*. Int. J. Climatology, **25**, 8, 1139-1145. doi:10.1002/joc.1192

ADAGUC: a project to provide convenient access to the data treasures of KNMI

John van de Vegte, Wim Som de Cerff and Bert van den Oord

Introduction

In its role as a National Data Centre the Royal Netherlands Meteorological Institute is hosting a true treasure in the form of many unique datasets. These datasets grow every day but it is a common property of treasures that accessing them can be difficult. Historically the atmospheric, meteorological and seismological communities are separate worlds with their own data formats and tools for data handling, making sharing of data difficult and cumbersome. On the other hand, KNMI data is increasingly becoming of interest to the outside world because of the continuously improving spatial and temporal resolution of e.g. model and satellite data and the interest in historical datasets. New user communities have come into existence that use geographically based datasets from many different fields in a cross-fertilizing way. This development is supported by the progress made in Geographical Information System (GIS) software. Almost all KNMI datasets contain the geospatial dimension and could be offered to the outside world in a scientifically correct and GIS-friendly way making it less cumbersome to work with.

The ADAGUC project[1)] (Atmospheric Data Access for the Geospatial User Community), an international consortium created and led by KNMI, aims at reducing the need for users to invent their own converter and mapping tools. Selected space borne atmospheric datasets will be made accessible by GIS to allow easy data comparison, resampling, selection, manipulation and visualization. Representatives of the (inter) national user communities are strongly involved in the project to guarantee proper accommodation of the user requirements. Next to developing easy access to KNMI datasets for the outside world, the (international) operational meteorology and meteorological research can profit from the introduction of GIS technology (see e.g. COST 719[2)]). Within ADAGUC emphasis will be laid on interoperability and harmonization of data resources such that a 'GIS -enabled' user can work with these datasets. ADAGUC serves as a pilot for applying GIS-technology in the future to the seismological, meteorological and climatology datasets of KNMI. Scientists and developers at KNMI are gaining hands on experience to improve the access to datasets in a scientific correct manner.

The ADAGUC project will aim at delivering the following: Open Source conversion tools for conversion of selected atmospheric datasets into an Open Standard GIS format, to publish atmospheric datasets in the previous mentioned GIS format, and a web service to demonstrate the usability of the above to the geospatial and atmospheric community. Dissemination of results is pursued by publications, workshops and international co-operation. The challenge is to create a solution that has the potential to become the next generation operational environment, dealing with international frameworks, standards, and cross domain end-users.

The world of GEO-ICT

In general (geo) data usage is accomplished by tools that are provided by third parties, for instance commercial companies or government institutes that see profit in or need for geospatial solutions. Other stakeholders are working on the standardization of data formats, metadata descriptions and services that can be used to interchange geospatial information. The most relevant developments in tooling, standards and services are discussed below.

Tools: Google Earth

Google Earth made the public aware of the importance of geospatial information. As a next step, third parties, commercial and non-profit organizations, are exploring the possibilities to place their own products into the Google Earth system. A wealth of geo-information is becoming available via Google Earth, ranging from holiday pictures, hotels, forest fires, earthquakes and meteorological forecasts. An example (Figure 1a and 1b) with Sciamachy data can be found at the SRON website[3)]. Google Earth uses the KML (Keyhole Markup Language) standard. This standard is under control of Google Earth and is turned into a propriety format thereby limiting the development of an open user community. Moreover, for scientific and professional applications Google Earth is of limited use despite its important role for GIS-awareness.

Tools: Geographical Information Systems

A well established set of GIS tools is a necessary framework to deal with different kinds of spatial data.

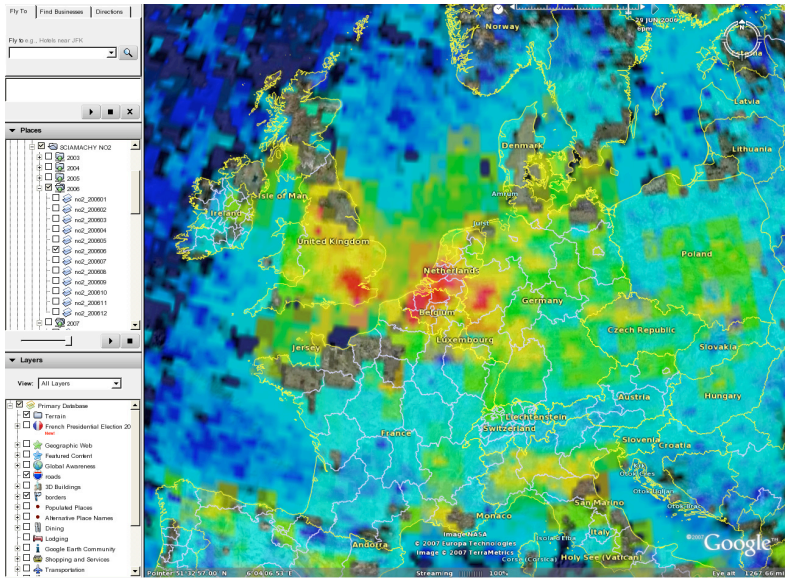

Figure 1a. Monthly average of Sciamachy NO2 tropospheric columns over Europe visualized in Google Earth.

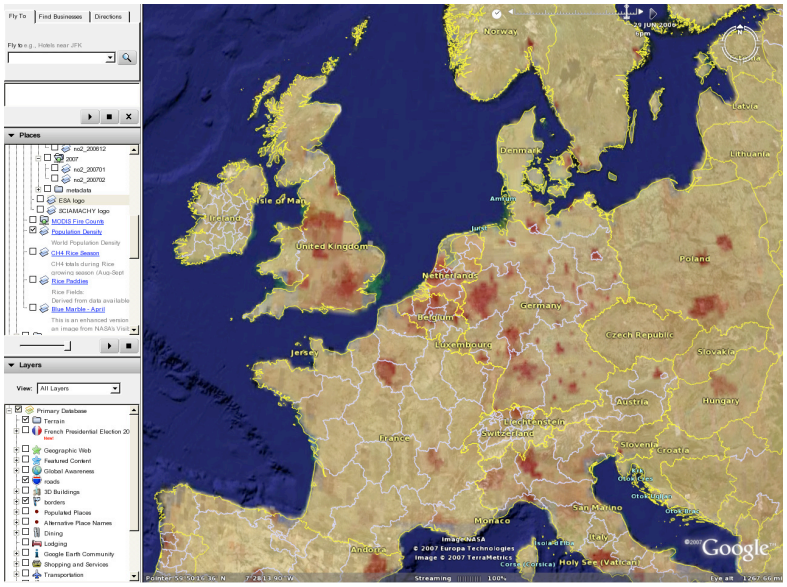

Figure 1b.
Population density for the same area that clearly show a correlation with the NO_2 distribution in figure 1a.

Since the 1960's GIS has evolved from digital cartography into geo-ICT and offers standardized ways to store, process, analyze and visualize spatial data. The current (commercial and free) GIS software cannot deal with the large data volumes and the temporal aspects of atmospheric data yet, although these issues are being addressed because of pressure from user interest groups. A good example of this is the support of NetCDF (Network Common Data Form) COARDS (Cooperative Ocean/atmosphere Research Data Service) and CF (Climate and Forecast Metadata Convention) in ArcGIS 9.2 (commercial GIS system from ESRI). NetCDF is a set of software libraries that enable the (technical) information interchange unambiguous across different computer platforms. COARDS and CF are metadata definitions (descriptions) to promote the exchange of information stored in NetCDF files by using a common standard. The incorporation of NetCDF in ArcGIS was promoted by the National Centre for Atmospheric Research[4] (NCAR) and ESRIs Atmospheric Special Interest Group[5].

Tools: ESRI ArcGIS

ESRI is the world leader in professional GIS software. ESRI provides solutions to deal with geospatial problems. Their software products serve the 'earth bound' communities like governments (e.g., cadastre like tasks), road and traffic organizations, petrochemical industries, soil and vegetation related institutes. ESRI's next step is to fulfil the wishes of the atmospheric data users: importing of atmospheric data formats, satellite view transformations and time resolutions from centuries to seconds are all on the list of being investigated by ESRI for future releases (Figure 2).

Standards: The Open Geospatial Consortium (OGC)

The OGC[6] deals with standardization of all geo related issues; their focus is on defining specifications by open working groups to create a common ground for interoperability. In this way the interpretation of geographical information becomes identical for all OGC compliant software making it easier to work with datasets and exchange these (Figure 3). OGC is for the interoperability of GIS what W3C (World Wide Web consortium) is for internet technology.

The challenge is to create an environment that has the potential to become the next generation operational solution, dealing with international frameworks, standards, and cross domain end-users

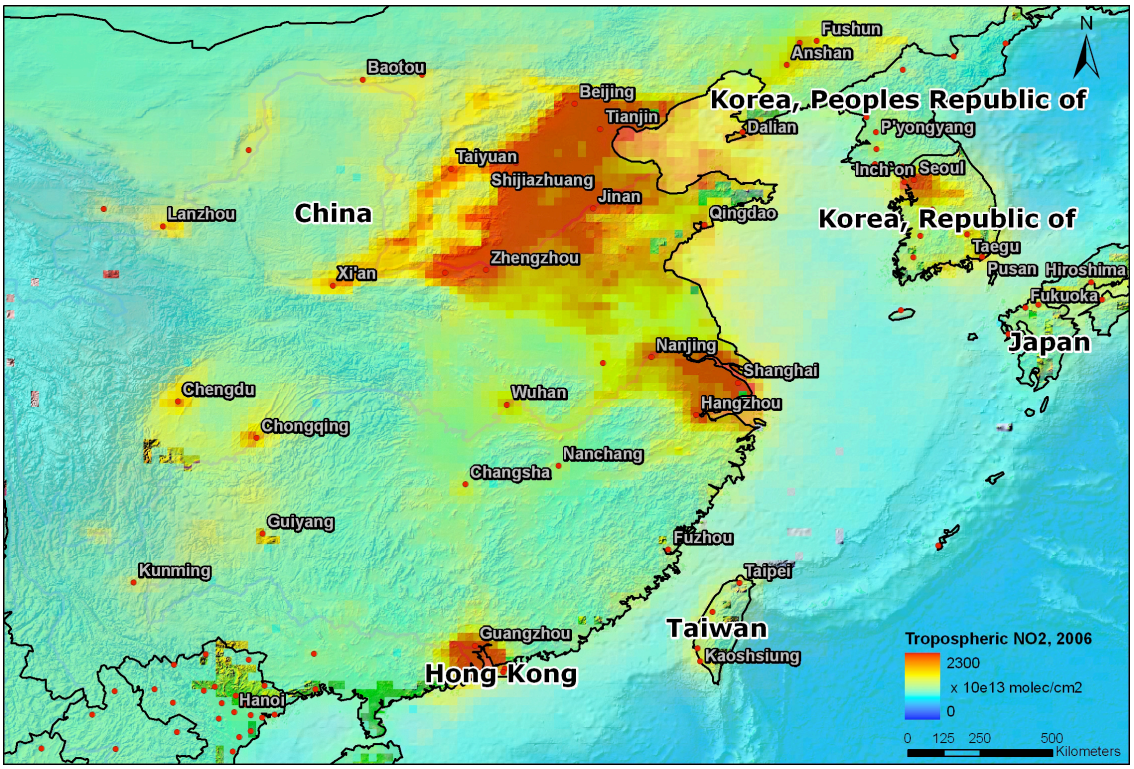

Figure 2. Tropospheric NO2 distribution from Sciamachy combined with the orography of eastern China with major cities, in ESRI's ArcGIS.

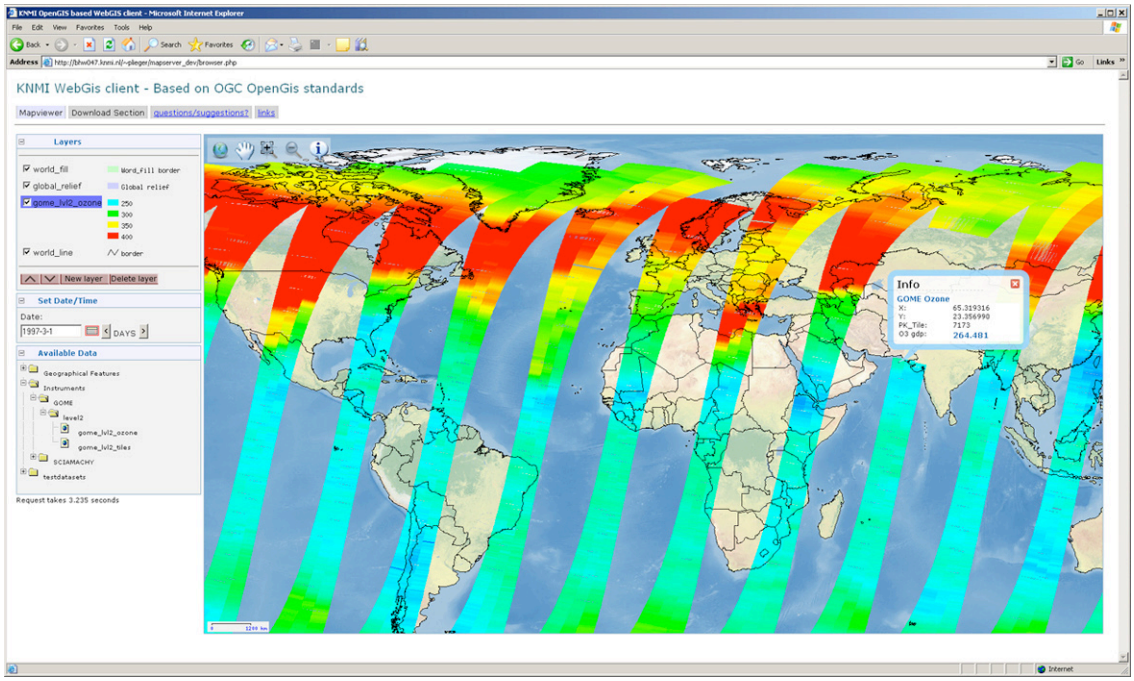

Figure 3. Example of an OGC based web service displaying features of ozone measurements from GOME that are stored in a PostgreSQL spatial database.

Being able to exchange information according to international standards is an important scientific, social and economic benefit for different communities

Since the 1960's GIS has evolved from digital cartography into geo-ICT and offers standardized ways to store, process, analyze and visualize spatial data. The current (commercial and free) GIS software cannot deal with the large data volumes and the temporal aspects of atmospheric data yet, although these issues are being addressed because of pressure from user interest groups. A good example of this is the support of NetCDF (Network Common Data Form) COARDS (Cooperative Ocean/atmosphere Research Data Service) and CF (Climate and Forecast Metadata Convention) in ArcGIS 9.2 (commercial GIS system from ESRI). NetCDF is a set of software libraries that enable the (technical) information interchange unambiguous across different computer platforms. COARDS and CF are metadata definitions (descriptions) to promote the exchange of information stored in NetCDF files by using a common standard. The incorporation of NetCDF in ArcGIS was promoted by the National Centre for Atmospheric Research[4] (NCAR) and ESRIs Atmospheric Special Interest Group[5].

Tools: ESRI ArcGIS

ESRI is the world leader in professional GIS software. ESRI provides solutions to deal with geospatial problems. Their software products serve the 'earth bound' communities like governments (e.g., cadastre like tasks), road and traffic organizations, petrochemical industries, soil and vegetation related institutes. ESRI's next step is to fulfil the wishes of the atmospheric data users: importing of atmospheric data formats, satellite view transformations and time resolutions from centuries to seconds are all on the list of being investigated by ESRI for future releases (Figure 2).

Standards: The Open Geospatial Consortium (OGC)

The OGC[6] deals with standardization of all geo related issues; their focus is on defining specifications by open working groups to create a common ground for interoperability. In this way the interpretation of geographical information becomes identical for all OGC compliant software making it easier to work with datasets and exchange these (Figure 3).
OGC is for the interoperability of GIS what W3C (World Wide Web consortium) is for internet technology.

Standards: Infrastructure for Spatial Information in the European Community (INSPIRE)

On 25 April 2007 the European Parliament adopted the INSPIRE directive which aims at establishing coordination between the users and providers of spatial information to ensure that the information and knowledge from different sectors can be combined. The directive applies to spatial data held by or on behalf of public authorities and to the use of spatial data by public authorities in the performance of their public tasks. In the forthcoming years INSPIRE will define the standards on data, metadata and services to which the European spatial information infrastructure must comply. INSPIRE implementation rules should be based, where possible, on international standards; in fact, these rules shall take account of relevant, existing international standards and user requirements, in particular with relation to validation metadata. The guidelines of all the standardizing bodies (e.g. WMO) require an overall vision and adequate participation to evaluate the potential impacts for KNMI.

Standards: Metadata, ISO19100 series

Optimal search and order capabilities rely on the use of homogeneous and uniform descriptions of metadata. ISO[7] has developed a series of standards (the 19100 series) for defining, describing and managing geographic information that includes a standard for metadata. This standard has been adapted by organisations like the WMO and the OGC. INSPIRE recommends the use of this standard for metadata. In the Netherlands GeoNovem[8], has defined the Dutch Metadata Standard for Geography based on the ISO standards. Within KNMI the ISO 19100 series has for the first time been used for the KNMI Operational Data Center[9] (KODAC) datasets metadata descriptions (ISO 19115). Currently the KODAC metadata is also compliant with Dutch Metadata Standard for Geography and available in both Dutch and English.

Standards: GIS compliant (meta-) data formats

The exchange of information is more then moving data from A to B. One has to be sure that the data is interpreted in a correct manner by all users and that the interpretation is independent of the user community. Data formats like NetCDF and HDF

(Hierarchical Data Format, developed by the National Center for Supercomputing Applications) are self-explanatory in terms of a file's content, which is in sharp contrast with the older binary files. The latter suffer from the fact that unfamiliar (remote or new) users cannot easily relate content and description, rendering them useless unless additional information is available. A similar aspect applies to the meta-data of a data collection. When meta-data descriptions are not uniform in terms of content and format, searching and ordering of data is cumbersome and often results in incomplete and erroneous results.

Services: Service Oriented Architecture (SOA)

Service Oriented Architecture is a concept in which many 'small', loosely coupled, distributed services interact to create a larger infrastructural service that is better maintainable and scalable: A change in one service has low impact on the overall service / production chain. SOA focuses on the interfaces and not on the implementation inside a service which is the responsibility of the owner. SOA is the opposite of the traditional monolithic architectures in which scalability and additional functionality can have considerable (cost) impact. An example of SOA in practice is the KODAC service that has completed its second phase by disclosing extra KNMI datasets via additional services.

The ADAGUC User Communities

The first ADAGUC workshop was organized at KNMI on 3-4 October 2006. Four distinct user communities, based on their specific needs for reliable and flexible access to atmospheric data, were identified:

- Policy Makers are interested in long term averaged/forecast products and maps that are archived for easy access. Many (inter)national stakeholders provide atmospheric data to their governments to develop policies with respect to the social and political impact of i.e. climate change.
- Earth System Scientists and Atmospheric Scientists are interested in data of the highest possible quality and resolution, both archived and real-time. The atmospheric users are particularly interested in aerosols, clouds and trace gases like NO_2 and SO_2.
- GIS Users are interested in high quality and averaged data, including archived datasets. GIS users are characterized as being non-experts in the field of atmospheric research; their focus is more on earthbound features and earth-atmosphere interactions.
- Risk assessment community is interested in mapped data, preferably in (near-) real time. These users are interested in products at an urban scale that are focused on industrial calamities, like gas leakage or chemical fires. The combination of inter-comparable data sources provides vital input to crisis management teams.

These communities are reflected in the five use cases defined by users in the ADAGUC team: 1) Air quality information based on satellite images; 2) Distribution maps of trace gases; 3) Relating remote sensing data with land use and vegetation data; 4) Improving river basin simulation models, and 5) Weather related disaster management. All these use cases are documented and made available to the communities and will be used as a starting point in identifying the specific user requirements. Implementation of the required services is planned in the next phase.

Conclusions

The project ADAGUC allows for improved exchange of information according to international standards, thus having important scientific, social and economic benefits. In the forthcoming years new standards for data exchange and data services will be legally imposed by means of the INSPIRE directive. The ADAGUC project is a pilot that aims at preparing KNMI, amongst others, for these upcoming changes. The project has a set of well-defined deliverables. Moreover KNMI becomes visible as a stakeholder in the GIS community and knowledge-sharing networks. The use of GIS also introduces a number of science-related challenges: mapping, gridding and projecting data must be done in such a way that the scientific integrity of the data is preserved. The ADAGUC project will identify these problems and seek for solutions.

The ADAGUC consortium consists of the following partners: Royal Netherlands Meteorological Institute (KNMI, lead), Netherlands Institute for Space Research (SRON), Wageningen University and Research Centre (WUR), Vrije Universiteit Amsterdam (VU), Institute for Marine and Atmospheric research Utrecht (IMAU), European Space Agency (ESA), National Center for Atmospheric Research (NCAR), Harvard University, Institute of Environmental Physics Heidelberg (IUP), UNIDATA programme, Institute of Methodologies for Environmental Analysis (IMAA)

ADAGUC is funded by the Space for Geo-Information Programme (RGI) (www.rgi.nl)

Relevant websites:

1) ADAGUC project web site: http://adaguc.knmi.nl
2) COST-719, the use of GIS in climatology & meteorology http://www.knmi.nl/samenw/cost719/
3) SCIAMACHY Products in Google Earth by J.M. Krijger: http://www.sron.nl/~krijger/google_earth/google_earth.html
4) National Centre for Atmospheric Research: http://www.ncar.ucar.edu
5) ESRI Atmospheric Special Interest Group: http://www.gis.ucar.edu/sig
6) Open Geospatial Consortium: http://www.opengeospatial.org
7) International Organization for Standardization http://wwww.iso.org
8) GEONOVUM: http://geonovum.nl
9) KNMI Operational Data Center: http://kodac.knmi.nl

Changes in the Atlantic Meridional Overturning Circulation

Sybren Drijfhout

Introduction: the concept of the MOC

Climate models project a slow down of the Atlantic Meridional Overturning Circulation (MOC) in the twenty-first century. This slow down is expected to affect climate over Europe. In particular, it damps the temperature rise due to the emission of greenhouse gases. The MOC is associated with the thermohaline circulation (THC), which is the large-scale ocean circulation driven by fluxes of heat and freshwater at the surface. It is difficult to define the THC exactly. In the real world we cannot disentangle the various driving forces of the ocean circulation, and exclude, for instance, the wind forcing. Even in idealized models in which the wind stress is neglected, a THC which only responds to the 'push' of surface waters, becoming convectively unstable and sinking, cannot be sustained. Also the 'pull' by small-scale mixing, that gradually lightens the deep waters, is necessary. And the main energy source for the small-scale mixing is mechanical (winds and tides). Clearly, the THC is only a theoretical concept. For practical purposes, oceanographers prefer to speak of the MOC: The zonally-integrated mass transport in the ocean. In the Atlantic Ocean it consists of northward flowing water above and southward flowing water below (Figure 1). This typical 'estuarine circulation' captures the essential part of the THC. In the North Atlantic, surface water cools and sinks, forming North Atlantic Deep Water which spreads southward into the deep ocean. As a result, the MOC is associated with a large northward heat flux: North of 30°N, the MOC dominates global ocean heat transport[1]. The loss of heat from the ocean to the atmosphere in the North Atlantic keeps North-Western Europe relatively mild.

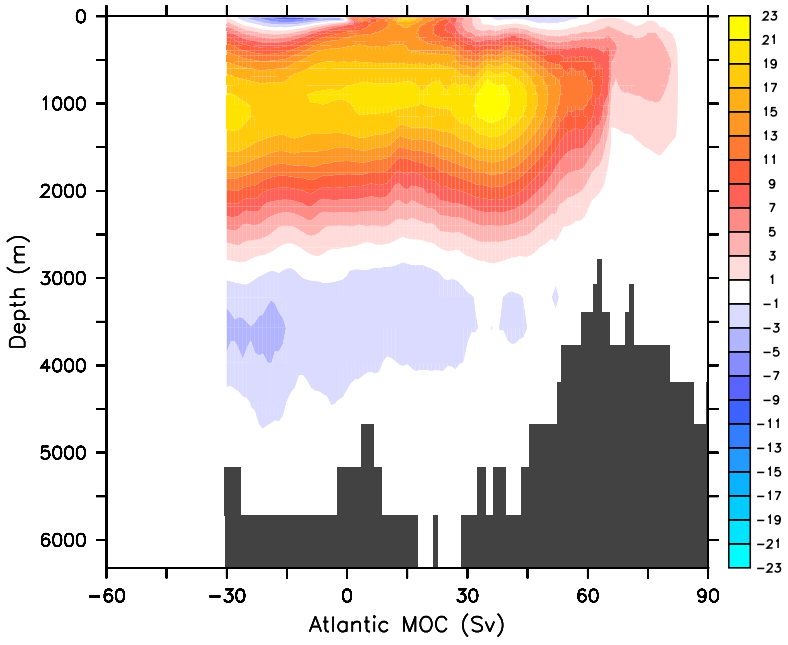

Figure 1. The present day ensemble mean MOC estimated from an ensemble of coupled model integrations carried out with the Max Planck Institute climate model within the ESSENCE project run at KNMI (in Sv = 10^6 m^3 s^{-1}).

The thermal and salt-driven part of the MOC is essentially nonlinear: Small changes in the thermohaline forcing (temperature and salt) can have large effects. As a result, the THC can be subject to sudden transitions. In the popular literature this is often phrased in terms of whether the 'Gulf Stream' will halt or not. In reality, the Gulf Stream is the western boundary current of a large wind-driven subtropical gyre, that will continue to flow as long as the earth rotates and the winds keep blowing. But the wind-driven gyre is not part of the MOC. The part that branches off between 30°N and 40°N and flows further northward along the West European and Scandinavian coastline constitutes the MOC, and this branch is vulnerable to anthropogenic climate change. In the media this branch is often identified with the Gulf Stream; in reality it is one of its many extensions. Here, we report on a number of studies performed at KNMI on the driving mechanisms of the MOC, its potential change and climate impact, and the detection of a slow down induced by anthropogenic climate change.

Forcing of the MOC and abrupt transitions

The Atlantic MOC is dominated by one large, basin-wide circulation of northward flowing waters between 0 and 1500 m depth, and southward flowing waters between 1500 and 3000 m depth. The strength of the MOC is surprisingly well related to the thermohaline forcing, although the MOC itself is partly wind-driven. The sinking branch occurs where water at the surface becomes sufficiently dense. In the present climate this happens in the Labrador Sea and Greenland-Iceland-Norwegian basin, because of cooling. The circulation intensifies when the cooling becomes stronger. It turns out that the circulation

depends on the (air) temperature-difference between the tropics and the subpolar regions, just south of the sea-ice margin. However, not only the temperature, but also the salinity affects the density of water. At the surface, the salinity is changed by evaporation, precipitation, and the growth or melt of sea ice. In the tropics evaporation makes the water dense, in the subpolar regions precipitation lightens water. The combination of these salinity-related forcings tends to drive an opposite circulation. Without temperature-effects the MOC would reverse, with sinking in the tropics and rising in the subpolar regions.

So, when the thermal forcing dominates, the result is a strong MOC characterized by northern sinking. When the haline forcing dominates, a much weaker MOC with sinking in the tropics occurs. Most interesting is the regime where both forcings are of comparable strength. In this regime both states are possible, that is, the MOC is bi-stable. The actual state depends on the history of the MOC. When it was already dominated by thermal forcing, it prefers to stay so; the same holds for the haline state. Such behaviour is called hysteresis[2]. Then, a thermohaline perturbation can induce an abrupt transition from one state to the other within a few decades. The most conceivable perturbation is a freshwater pulse in the North Atlantic (e.g., by glacier or ice-cap melting), which will always tend to bring the MOC from the thermally forced state to the haline state at which the MOC is strongly reduced in strength or even reversed.

Abrupt MOC reduction in future climate

Anthropogenic forcing due to rising emissions of greenhouse gases tends to weaken the thermal forcing: Polar and subpolar temperatures will rise much faster than tropical temperatures in the twenty-first century[3]. At the same time the haline forcing counteracting the MOC is expected to increase. In a warmer world the hydrological cycle is intensified and sea and land-ice will melt. As a result, most climate models project a decrease of the MOC between 0 and 50% for the next century, although none of them simulates a collapse[3]. But the concern remains that the MOC not only weakens; also its stability could decrease in the future because it approaches, or further penetrates into the bi-stable regime.

The transition point where the mono-stable, thermally forced state changes to the bi-stable state, at which an abrupt transition can take place, is marked by the sign of the net freshwater transport into the Atlantic basin by the MOC[4]. The Atlantic is a net evaporative basin; easterly trade winds carry water vapour from the Atlantic to the Pacific across the narrow isthmus of Panama. This water vapour loss is compensated for by the ocean circulation. We discriminate two mechanisms by which the ocean circulation can import freshwater into the Atlantic. When at the southern boundary the upper layers are fresher than the lower layers, the MOC imports freshwater. When at 30°S the water at the eastern boundary has lower salinity than the water at the western boundary, the wind-driven, azonal circulation imports freshwater into the Atlantic. When the MOC imports freshwater into the Atlantic it is mono-stable. This can be understood as follows: Let us assume a positive freshwater anomaly in the north, for instance as a result of increased sea-ice melt. This anomaly decreases the surface density. As a result, the sinking of deep water reduces and the MOC is weakened. If the MOC *imports* freshwater, a weaker MOC will make the Atlantic more saline; the (positive) freshwater anomaly is damped. Also a negative freshwater anomaly will be damped. But if the MOC *exports* freshwater, the opposite occurs and freshwater anomalies in the north are amplified by the response of the MOC. In this case the MOC is bi-stable. It is possible that a positive freshwater anomaly induces a collapse of the MOC. A freshwater export by the MOC is possible when the wind-driven circulation imports enough freshwater to allow for freshwater loss by both the MOC and through net evaporation. Although the error bars are large, a best estimate from the observations indicates that the latter is the case in present climate.

A recent analysis of a suite of coupled models used for paleoclimate research has revealed that nearly all models are biased towards the mono-stable regime[4]. In these models the evaporation over the Atlantic is too large, and freshwater import by the azonal circulation is too small. In a follow-up study we have repeated this analysis for a series of IPCC-class climate models that simulate both the present as well future climate. The same bias appears again, but more interesting, the MOC tends to shift in the future towards the bi-stable regime in (nearly) all models, despite the future increase of net evaporation over the Atlantic basin which all models predict (Figure 2). This result suggests two important facts: In present-day climate models the Meridional Overturning Circulation is too stable; The risk of abrupt climate change induced by a sudden strong reduction of the MOC due to the enhanced greenhouse effect, is increasing.

KNMI and the University of Utrecht, in collaboration with SARA, have performed a series of climate change

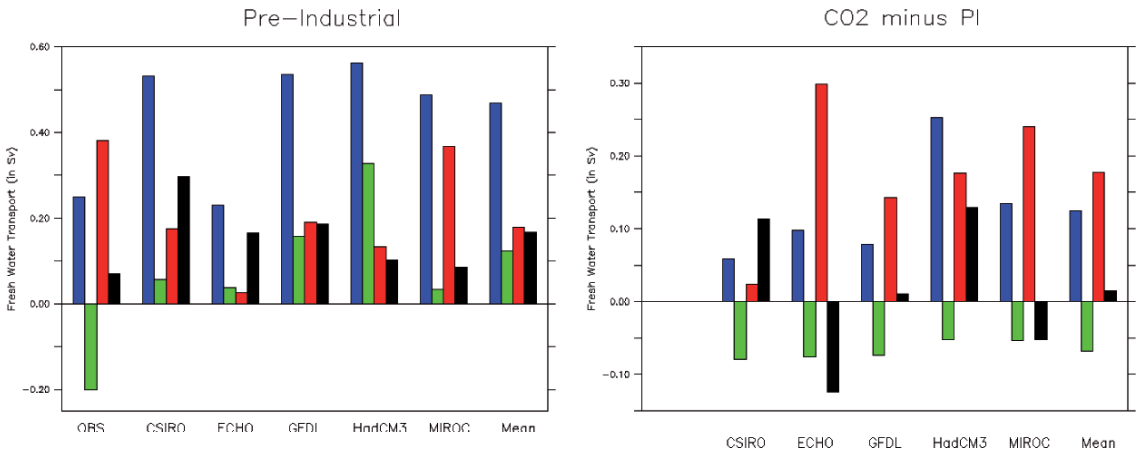

Figure 2. The terms of the Atlantic freshwater budget for the pre-industrial control state (left panel) and the difference between the quadrupled CO_2 state and the control state (right panel) for the simulations indicated on the horizontal axis. The terms (in Sv) are net evaporation (blue), freshwater transport by the MOC (green), transport by the azonal circulation (orange) and drift (black). Open bars denote 'observed' values. From de Swaluw et al., manuscript in preparation.

In present-day climate models the MOC is too stable for perturbations; the risk of abrupt climate change induced by a strong reduction of the moc increases due to the enhanced greenhouse effect is underestimated

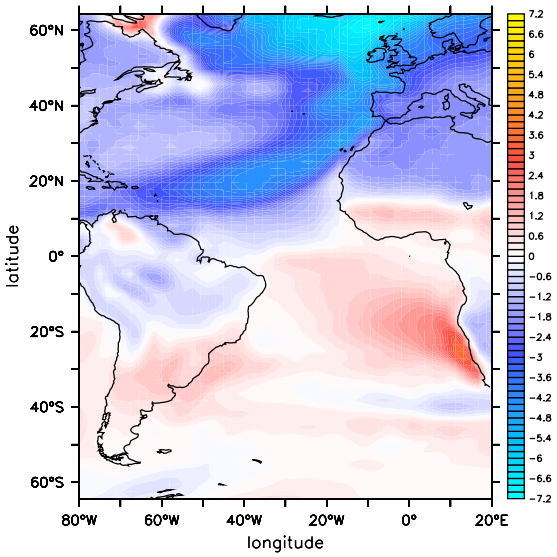

Figure 3. The ensemble mean temperature difference in degrees Celsius between a series of runs with and without imposing a MOC collapse, 90 years after the collapse has been induced by a freshwater pulse (difference between 2100 and 2010 after collapse between 2010 and 2040). The coupled model integrations have been carried out with the Max Planck Institute climate model within the ESSENCE project run at KNMI.

scenario runs with an IPCC-class model in which a MOC collapse was artificially forced, to study its impact on climate (Figure 3). We recover a 3°C cooling over Western Europe which is a well known result. Together with anthropogenic warming this would result in a cooling of only 0.5°C in 2050. Of specific interest is the pattern of the temperature change: Cooling over the North Atlantic, heating over the South Atlantic. The associated Sea Surface Temperature (SST)-anomaly induces a shift in the Inter Tropical Convergence Zone, the net precipitation, and the Hadley circulation. Climate models tend to underestimate the atmospheric response (and possible feedbacks) to such a collapse, as simulated oceanic mixed layers in the tropical Atlantic are too deep and the SST changes are too weak there. Also, such heating patterns might induce a shift in the Atlantic storm tracks inducing additional cooling of North-Western Europe[5], but this response is very sensitive to the amplitude and pattern of the SST-anomaly

Detecting changes in the MOC

Recently a slowing of the MOC over the past fifty years was reported[6] that was much stronger than simulated by any climate model. The reported

decrease, however, may have been severely biased by under-sampling of the natural variability of the MOC. The analysis was based on five 'snapshot' measurements over a period from 1950 to 2005 (in situ hydrographic sections across the Atlantic by research vessels). In general, before a long-term change can be detected, one must be able to estimate whether the change is associated with a real trend, or whether it represents a fluctuation that results from the high-frequency internal variability. For a more complete continuous observational assessment of the MOC, a mooring-array was deployed by the UK and USA in 2004.

We simulated the detection problem by analyzing the anthropogenic signal and noise associated with the natural variability of the MOC in a large, 62-member ensemble of climate model simulations, all forced with increasing levels of greenhouse gas concentrations in the atmosphere. We also estimated the noise associated with the measurement error[7]. The signal-to-noise ratio was separately estimated for snapshot measurements and continuous monitoring. The signal-to-noise ratio peaks near 30°N and 30°S at 2000 m depth, confirming the rationale for the mooring-array at 26°N. Also, detection occurs much faster when the MOC is continuously monitored, due to the decrease in noise (Figure 4). The apparent slow-down of the MOC that was recently suggested[6] must have been due to unresolved internal variability.

Conclusions

Based on observations the present-day MOC seems to reside in the bi-stable regime. Nearly all IPCC-class climate models appear to be biased towards a too stable MOC. The apparent stability of the MOC over the last 8000 years, however, suggests that the risk of a collapse in this century is not large. The impact of a of the Meridional Overturning Circulation on European climate would be significant but not dramatic; together with the present anthropogenic warming both effects will neutralize each other in Europe between 2050 and 2100. Detection of the anthropogenic MOC-trend on the basis of episodic measurements appears impossible before 2055. With continuous monitoring, detection becomes possible after 30-35 years of observation. Detection times are shortest near 25°N and 30°S.

The impact of a MOC collapse on European climate would be significant but not dramatic; together with the present anthropogenic warming both effects will neutralize each other in Europe between 2050 and 2100

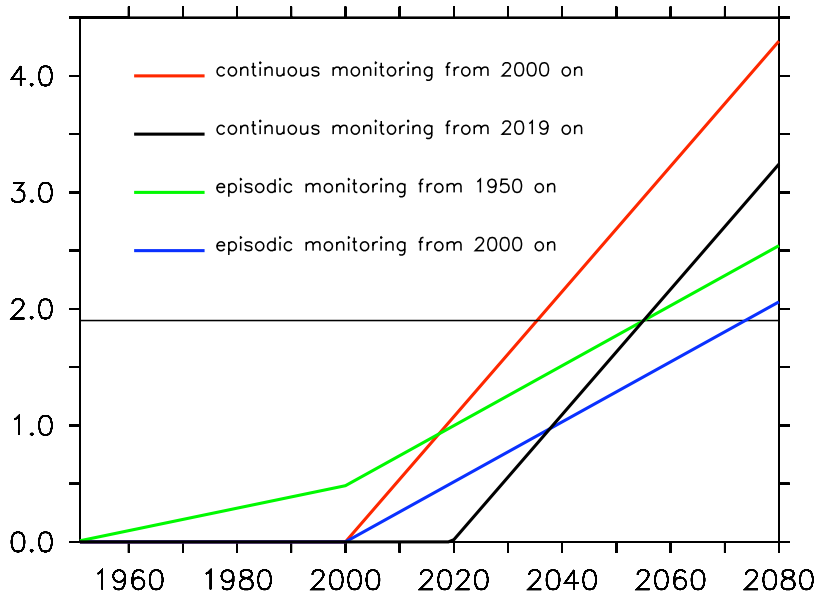

Figure 4. The signal-to-noise ratio of the anthropogenically forced decline of the MOC at 26°N, as a function of time. Estimates are based on sustained measurements starting in 2000 (red) and 2019 (black), and based on snapshot measurements starting in 1950 (green) and 2000 (blue), respectively. The horizontal line marks the signal-to-noise ratio of 1.96, where detection becomes possible.

1) Ganachaud, A. and C. Wunsch, 2003. *Large-scale ocean heat and freshwater transports during the World Ocean Circulation Experiment.* J. Climate, **16**, 696-705.
2) Ramstorf, S., 1995. *Bifurcation of the Atlantic thermohaline circulation in response to change in the hydrological cycle.* Nature, **378**, 145-149.
3) *IPCC fourth assessment report: Climate change 2007.*
4) Weber, S.L., S.S. Drijfhout and PMIP-members, 2007. *The modern and glacial overturning circulation in the Atlantic Ocean in PMIP coupled model simulations.* Climate of the Past, **3**, 51-64.
5) Schrier, G. van der, S.S. Drijfhout, W. Hazeleger and L. Noulin, 2007. *Increasing the Atlantic subtropical jet cools the circum North-Atlantic.* Meteor. Z., **16**, in press.
6) Bryden, H.L., H.R. Longworth and S.A. Cunningham, 2005. *Slowing of the Atlantic meridional overturning circulation at 25°N.* Nature, **438**, 655-657.
7) Drijfhout, S.S. and W. Hazeleger, 2007. *Detecting Atlantic MOC changes in an ensemble of climate change simulations.* J. Climate, **20**, 1571-1582.

An integral approach for the representation of Turbulence, Convection and Clouds in weather and climate models

A. Pier Siebesma and Wim de Rooy

Introduction

Notwithstanding the ever increasing computer resources, it is probably fair to state that most of the crucial processes in the clear and cloudy boundary layer will remain unresolved for both Numerical Weather Prediction (NWP) and climate models in the foreseeable future. Nevertheless, these unresolved processes, such as turbulence, convection, cloud dynamics and precipitation determine to a large extent the daily weather and climate conditions in which we live. It is therefore crucial to include these processes consistently in a parameterized way in both NWP and climate models and the design and implementation of such a coherent parameterization has been identified as a common key issue in both the climate and the weather research department of the KNMI. To bind expertise and to make optimal use of the limited resources at KNMI for model development, research efforts have been joint together in an internal project MESOMOD. The central aim of this project is the design of an integral approach for the representation of the most important sub-grid processes, namely turbulence, convection and cloud processes.

The term integral approach here refers to two issues. Firstly, the turbulence, convection and cloud parameterization are developed as one integral module. This will facilitate the exchange between different target models. Secondly, the physical parameterizations are tightly interlinked. Turbulence and convection are even described in one formulation in the so-called Eddy Diffusivity/Mass Flux (EDMF) approach[1, 2, 3]. Furthermore, convection and turbulence processes provide information on the subgrid variability of moisture that is used in a statistical cloud parameterization to estimate cloud cover and cloud water content. By applying an integral approach to all these processes, the interactions between clouds, convection and turbulence can be taken into account in a physical consistent manner.

The ultimate goal is to use this scheme operationally for both operational NWP and climate scenario purposes by implementing it in both the non-hydrostatic high resolution NWP model HARMONIE-MESO and in the regional atmospheric climate model RACMO. The latter activity is part of an externally funded project Climate Changes, Spatial Planning (CCSP). The initiative for this approach was initiated at ECMWF while the first author was working there as a consultant. Similar developments are being pursued at ECMWF and more recently also at Météo France for use in the French non-hydrostatic model AROME. It is for this reason that the development of this unified turbulence-convection-cloud scheme is done in close collaboration with these two institutes.

In the next two sections we highlight two recent model developments that contribute to the integral boundary layer scheme.

The Eddy Diffusivity Mass Flux (EDMF) approach

The traditional way to parameterize turbulent transport in the clear and cumulus topped boundary layer is to use an eddy-diffusivity approach for the clear boundary layer and the subcloud layer, whereas an advective mass flux approach is used for the convective transport in the cumulus cloud layer. This rather ad-hoc split up has led to numerous problems such as double counting of transport processes and unrealistic transitions between the clear and cloudy boundary layer. Moreover, the use of a simple eddy-diffusivity approach in the clear boundary layer has been criticized for decades because it merely assumes turbulent transport to be down-gradient. Therefore this method is unable to describe non-local mixing in the upper part of the convective boundary layer, where often a slightly stable potential temperature profile is observed.

In order to overcome these drawbacks a new method has been proposed that combines the advective mass-flux approach and the eddy-diffusivity method in a coherent way, so that it paves the way for a unified parameterization of turbulent transport in the cloud topped boundary layer. The whole concept is based on a separate treatment of the organized strong updrafts and the remaining turbulent field. The non-local updrafts are described by an advective mass-flux approach whereas the remaining turbulent part is represented by an eddy-diffusivity approach

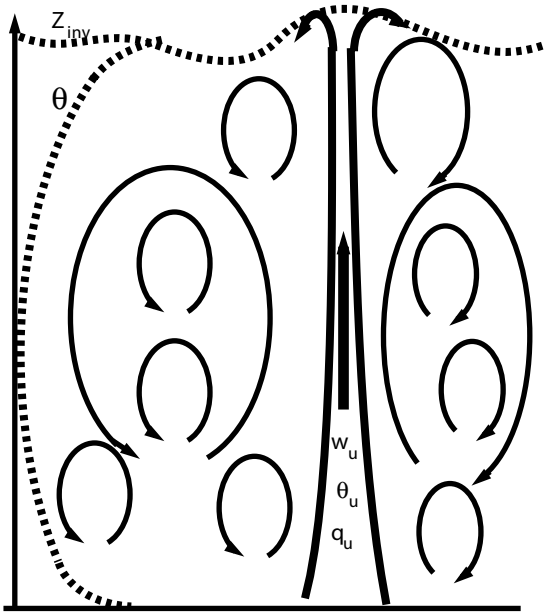

Figure 1. Sketch of a convective updraft embedded in a turbulent eddy structure.

(see Figure 1). The basic idea has been formulated in[1, 3] and practical applications of this approach to the cloud topped boundary layer have been discussed in[2].

In short, by assuming that strong updrafts occupy only a small spatial fraction, it can be derived that the turbulent flux of any conserved variable ϕ, can be well approximated by

$$\overline{w'\phi'} \approx -K\frac{\partial\bar{\phi}}{\partial z} + M\left(\phi_u - \bar{\phi}\right)$$

where the subscript u refers to the strong updrafts, overbars denote a spatial average, primes deviations from this average, K the eddy diffusivity. The mass flux is defined as $M \equiv a_u\left(w_u - \bar{w}\right)$, i.e. the product of the updraft velocity and the updraft area a_u. The first term on the right hand site describes the small scale turbulence while the second term, i.e. mass flux term, describes the non-local organized transport due to the strong updrafts. It should be noted that this mass flux term will be active in both the clear and the cloudy boundary layer case so that a continuous transition between the clear and cloudy boundary layer is possible and a triggering mechanism for the onset of cumulus convection is not necessary anymore. Moreover, in clear conditions the mass flux term describes the countergradient transport and is able to create a realistic slightly stable temperature profile in the upper part of the convective boundary layer.

Finally we need to obtain coefficients for the eddy-diffusivity K, the mass-flux M and a model for the updraft fields ϕ_u. Although the optimal choice of these coefficients is still an active field of research, simple assumed profiles for the eddy diffusivity K and the mass flux M already give surprisingly good results. As a demonstration Figure 2a compares the development of the boundary layer height parameterized by the EDMF scheme with Large Eddy Simulation (LES)

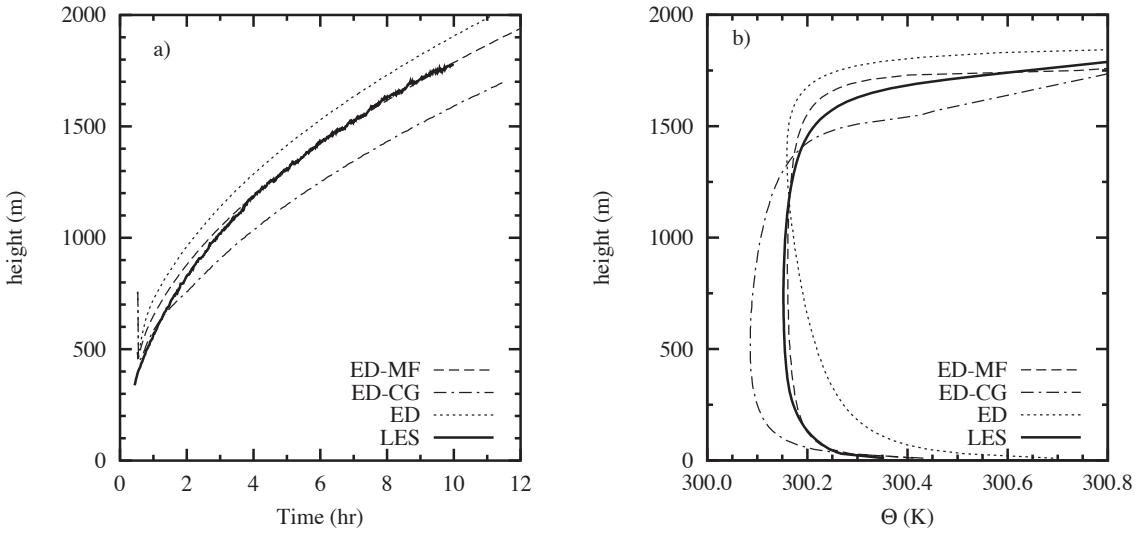

Figure 2. a) Boundary layer growth determined by: the single Eddy-Diffusivity approach (dotted), Eddy-Diffusivity combined with a countergradient term (dash-dotted) and by the EDMF approach along with the LES results as a reference. b) The mean potential temperature profile after 10 h of simulation for all three approaches.

The whole concept is based on a separate treatment of the organized strong updrafts and the remaining turbulent field

model results. It shows superior behaviour when compared with the traditional eddy diffusivity (ED) approach or with the eddy-diffusivity-countergradient (EDCG) method. Moreover Figure 2b shows that the temperature profile structure is also best represented by the EDMF method. For a further physical explanation of this performance we refer to the literature[3].

A simple parameterization for detrainment in shallow cumulus[4]

Virtually all shallow cumulus convection parameterizations use a mass flux concept. Within the mass flux framework the upward mass transport is usually described by a simple budget equation

$$\frac{\partial M}{\partial z} = (\varepsilon - \delta)M$$

where M denotes the upward mass flux, the fractional entrainment coefficient ε describes the inflow of environmental air into the cloudy updraft while the fractional detrainment δ describes the outflow of cloudy air into the environment. Recently there has been renewed interest in the parameterization of especially the fractional entrainment rate. However, little attention has been paid to the parameterization of the detrainment process although this counterpart of the cloud mixing process is, as this study shows, even more important for obtaining realistic mass flux profiles in cumulus convection.

The most simple and still widely applied description of lateral mixing in a mass flux concept is the use of fixed fractional entrainment and detrainment rates. With 'fixed' we mean constant values or some fixed function with height. Siebesma and Holtslag[5] demonstrated that well-chosen constant detrainment and entrainment rates are adequate for the relatively simple steady-state BOMEX shallow convection case[6]. However, Single Column Model (SCM) results with the same fixed ε and δ for the more complex ARM case[7], with varying cloud depths and environmental conditions, reveal large discrepancies with LES results. To explain these differences between the LES model and SCM, we analyze the lateral exchange in the LES model for three different shallow convection cases.

The LES results show that from hour to hour and case to case, the fractional entrainment rate shows little variation and it can be demonstrated that one fixed function, namely ε=1/z[8] performs very well for a wide range of conditions (see Figure 3a for the complex

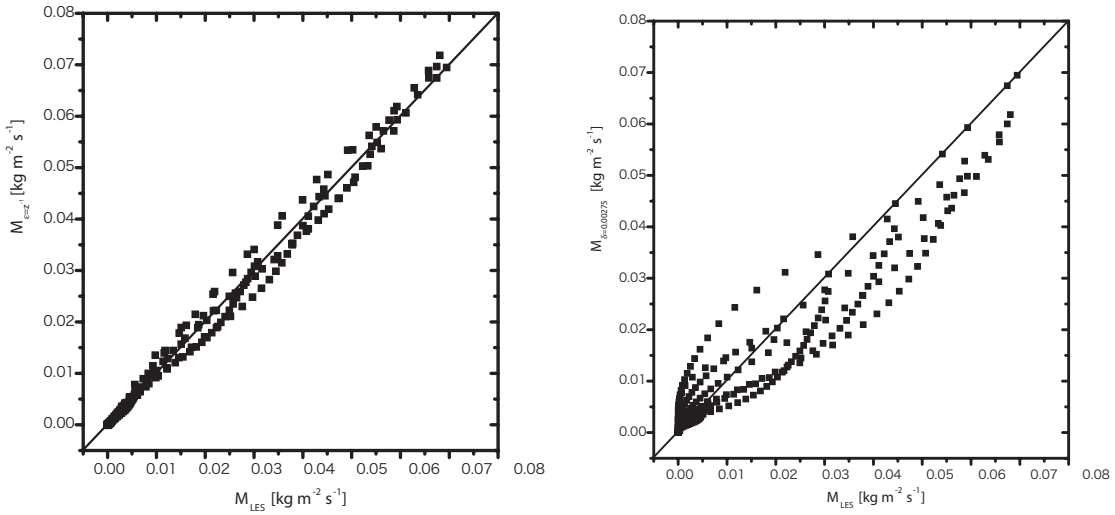

Figure 3. Comparison of the mass flux M for the ARM case[7] as directly diagnosed from LES with (a) the mass flux obtained using a fixed ε = 1/z along with the dynamical LES diagnosed δ or (b) with the mass flux obtained using δ = 2.75·10⁻³ m along with the dynamical LES diagnosed ε.

ARM case). We therefore adopt this fixed function for ε in our parameterization. On the other hand LES results also reveal much more variation in the fractional detrainment rate with a strong influence on the mass flux profile (see Figure 3b). The value of δ seems to depend mainly on two factors. Firstly, δ depends on the cloud layer depth. Under normal conditions a shallow convection scheme in a NWP or climate model represents an ensemble of clouds, leading to a decreasing mass flux profile with height and zero mass flux at the top of the cloud layer[9]. However, if we apply fixed fractional entrainment and detrainment rates we also fix the mass loss per meter. Figure 4 shows how fixed rates based on the BOMEX case (with a cloud layer depth of 1000m) lead to a non-zero mass flux at cloud top for a shallower cloud layer while applying these rates on a deeper cloud layer result in an almost zero mass flux already halfway the cloud layer, all in disagreement with the cloud ensemble and LES. With an approximately fixed function for the entrainment coefficient it can be simply understood that this calls for smaller detrainment rates for deeper cloud layers, as also confirmed by LES. Nevertheless, current mass flux schemes ignore this cloud layer height dependence, evidently leading to erroneous mass flux profiles. In our approach the mass flux profile is considered in a non-dimensionalized way, therewith dealing with the effect of the cloud layer height.

The second important factor changing δ is the environmental condition. Many studies (see e.g.[10]) showed the influence of the relative humidity of the environmental air surrounding the updrafts. If the surrounding air is moister, less evaporative cooling will occur if this air is mixed with cloudy air and this leads to less detrainment. However, besides the humidity of the environment also the buoyancy excess of the updraft air determines whether the mixture becomes negatively buoyant and consequently detrains. This combined effect is nicely captured by the so-called critical fraction χ_c of the environmental air[10]. This parameter is defined as the fraction of environmental air that is needed to make a mixture of environmental and updraft air neutrally buoyant. Figure 5 reveals how in our approach χ_c is used in a bulk sense to describe the effect of environmental conditions on the non-dimensionalized mass flux profile and therewith on the fractional detrainment rate. With this distinct relation based on LES for three different shallow convection cases, our detrainment parameterization is closed.

Current mass flux schemes ignore this cloud layer height dependence, evidently leading to erroneous mass flux profiles

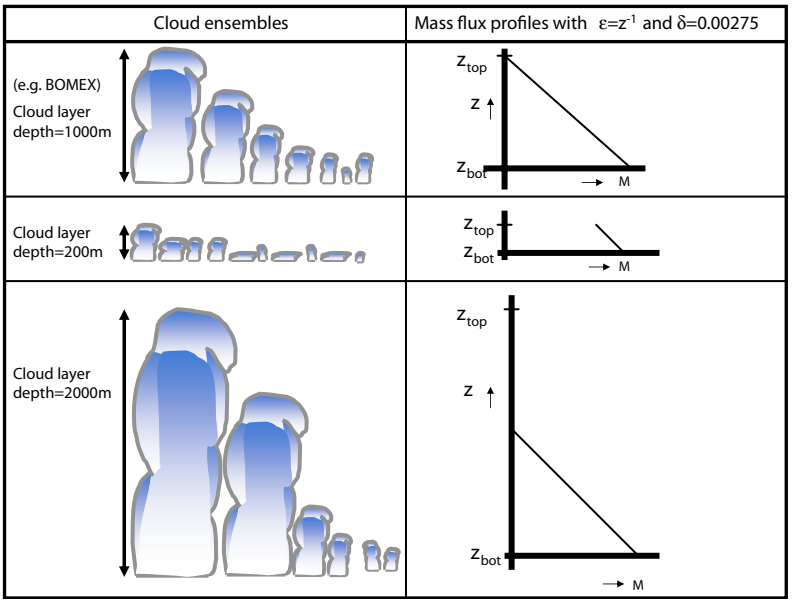

Figure 4. Cloud ensembles for different cloud layer depths and the corresponding mass flux profiles using fixed ε and δ based on a cloud layer depth of 1000m (BOMEX[6]).

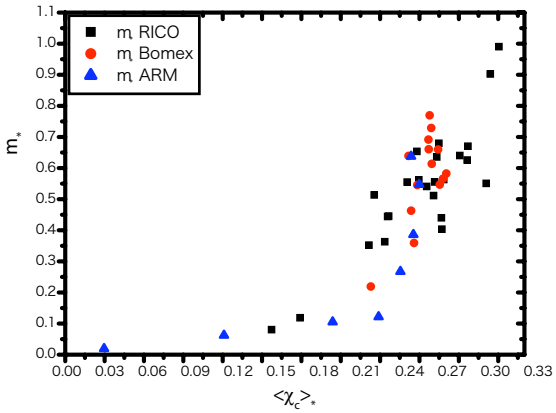

Figure 5. LES results showing for three different shallow convection cases the relation between m_* and $<\chi_c>_*$, where m_* is the non-dimensionalized mass flux (M/Mb where Mb is the cloud base mass flux) half way the cloud layer, and $<\chi_c>_*$ is χ_c (see text) averaged over the corresponding layer, i.e. the lower half of the cloud layer.

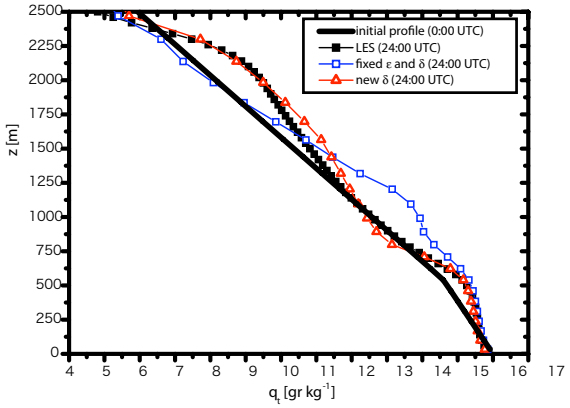

Figure 6. Total water specific humidity profiles after 24 hrs of simulation during the RICO case11) for the LES model and for the SCM using fixed ε and δ or the new detrainment parameterization.

Results with the new parameterization in a Hirlam SCM for a wide range of shallow cumulus convection cases (BOMEX[6], ARM[7] and RICO[11]) illustrate the strength of this new detrainment parameterization. As an example, we show in Figure 6 the total specific humidity profile of the RICO case after 24 hours of simulation. Presented are the results of an LES model, a SCM with fixed fractional entrainment and detrainment coefficients as known from literature (based on LES results for BOMEX), and finally a SCM with the new detrainment parameterization. The new parameterization gives an almost perfect match with the LES humidity profile. There is also a large improvement on the results with fixed entrainment and detrainment coefficients which can be explained by the relatively deep cloud layer and favourable conditions for updrafts during the RICO case which leads to relatively small fractional detrainment values and thus strong convection.

Results from LES and SCM show clearly the potential of our approach for a wide range of shallow convection cases. The new parameterization can be seen as a robust alternative for more complex buoyancy sorting based convection schemes without some of the disadvantages. Moreover, the new parameterization is computationally cheap and can be easily included in existing mass flux schemes.

Conclusions and outlook

A unified and integral parameterization approach is essential for the description of the clear and cloudy boundary layer. The EDMF approach presented here provides an excellent framework to accomplish this. Within this framework a number of processes still need to be further parameterized. For example, for the convective transport in the cloud layer, a realistic representation of the mass flux is crucial and it is predominantly determined by the detrainment rate. The new developed detrainment parameterization presented above, is therefore an important step to the application of the EDMF approach in operational climate and NWP models.

Within MESOMOD and in international cooperation we are developing and evaluating the various EDMF components[12, 13]. Perhaps the most important hurdle that has to be tackled at this moment is the use of a Turbulent Kinetic Energy (TKE) scheme for the Eddy Diffusivity part and its interaction with the mass flux component.

1) Siebesma, A.P. and J. Teixeira, 2000. *An advection-diffusion scheme for the convective boundary layer, description and 1d-results.* Proc. 14th Symposium on Boundary Layers and Turbulence, August 7-11, 2000, Aspen, USA, 133-136.

2) Soares, P.M.M., P.M.A. Miranda, A.P. Siebesma and J. Teixeira, 2004. *An Eddy-Diffusivity/Mass-flux parameterization for dry and shallow cumulus convection.* Quart. J. Royal Meteor. Soc., **130**, 3365-3384.

3) Siebesma, A.P., P.M.M. Soares and J. Teixeira, 2007. *A Combined Eddy-Diffusivity Mass-Flux Approach for the Convective Boundary Layer.* J. Atmos. Sci., **64**, 1230-1248.

4) Rooy, W. C. de and A.P. Siebesma, 2007. *A simple parameterization for detrainment in shallow cumulus.* Mon. Wea. Rev., in press.

5) Siebesma, A. P. and A.A.M. Holtslag, 1996. *Model impacts of entrainment and detrainment Rates in Shallow Cumulus Convection.* J. Atmos. Sci., **53**, 2354-2364.

6) Holland, J.Z. and E.M. Rasmusson, 1973. *Measurement of atmospheric mass, energy and momentum budgets over a 500-kilometer square of tropical ocean.* Mon. Wea. Rev., **101**, 44-55.

7) Brown, A.R. and 12 co-authors, 2002. *Large-eddy simulation of the diurnal cycle of shallow cumulus convection over land.* Quart. J. Royal Meteor. Soc., **128(B)**, 1075-1094.

8) Siebesma, A.P. and 13 co-authors, 2003. *A large eddy simulation intercomparison study of shallow cumulus convection.* J. Atmos. Sci., **60**, 1201-1219.
9) Siebesma, A. P. and J.W.M. Cuijpers, 1995. *Evaluation of parametric assumptions for shallow cumulus convection.* J. Atmos. Sci., **52**, 650-666.
10) Kain, J.S. and J. M. Fritsch, 1990. *A one-dimensional entraining/detraining plume model and its application in convective parameterization.* J. Atmos. Sci., **47**, 2784-2802.
11) www.knmi.nl/samenw/rico
12) Neggers, R.A.J., M Köhler and A.C. Beljaars. *A dual Mass Flux Framework for boundary layer convection; Part 1: Transport.* Submitted to Mon. Wea. Rev..
13) Neggers, R.A.J., M Köhler and A.C. Beljaars. *A dual Mass Flux Framework for boundary layer convection; Part 2: Clouds.* Submitted to Mon. Wea. Rev..

Assessing methane emissions from global spaceborne observations

Michiel van Weele

Introduction

In the past two centuries, atmospheric methane (CH_4) concentrations have more than doubled. Despite the about 200 times smaller atmospheric burden of methane compared to carbon dioxide (CO_2) this increase constitutes about 20% of the anthropogenic climate forcing by greenhouse gases (0.48 ±0.05 Wm^{-2}; IPCC 4th assessment report, 2007), because on a per molecule basis methane is a much more effective greenhouse gas than CO_2. Remarkably, the methane growth rate has decreased markedly since the early 1990s, and global concentration levels have remained relatively constant since 1999 (Figure 1). The possible causes of this leveling off are subject of intense scientific debate[1,2,3].

An obvious explanation would be that the total global methane emissions have been more or less constant since the end of the 1980s (apart from some anomalous years such as 1993 and 1998), and that the chemical sinks have reached equilibrium with the sources during the 1990s. However, even if this would be true most important questions remain. Assumed anthropogenic emission reductions by improved agricultural practices and waste treatment may be counteracted by increased emissions from fossil fuel production and consumption. Climate changes and land-use changes, e.g., tropical deforestation, are likely to change the natural emissions, though possibly with different signs. The lifetime of methane in the atmosphere is controlled by oxidation, mainly in chemical reaction with the hydroxyl radical (OH) which correlates strongly with solar ultraviolet radiation[4], modulated by overhead ozone (O_3) and clouds. OH levels may get enhanced by increases in water vapour, tropospheric ozone and nitrogen oxides (NO_X), but reduced by increases in carbon monoxide (CO) and methane itself. Recent redistributions of anthropogenic emissions, mainly from Europe and N-America to Asia, may also affect the methane trend. Therefore, in order to answer

Anthropogenic sources (in Tg/year)		**Natural sources** (in Tg/year)		**Sinks** (in Tg/year)	
Fossil *(coal/oil/gas)*	102	Wetlands	145	Tropospheric *OH*	523
Rice	80	Termites	20	Soils	30
Burning	45	Ocean	15	Stratospheric	40
Animals	98	Geologic	18		
Waste	70	Plants	?		
Totals	395		198		593

Table 1. The global methane budget. Methane sources and sinks estimates[5]. A new, so far unaccounted, plant source has been reported recently [10]. A closed global budget has been assumed (no trend). Anthropogenic emissions (about two-third) are reasonably well constrained by the combination of pre-industrial methane concentration levels from ice cores and bottom-up estimates based on socio-economic statistics of anthropogenic activities. Natural sources (about one third) are much more uncertain. These emissions vary considerably in time and space and available ground-based measurements are sparse, albeit precise, and hardly representative for larger scales. Oxidation, mainly in chemical reaction with OH radicals, leads to an atmospheric lifetime of 8.7±1.3 years (IPCC 4th assessment report).

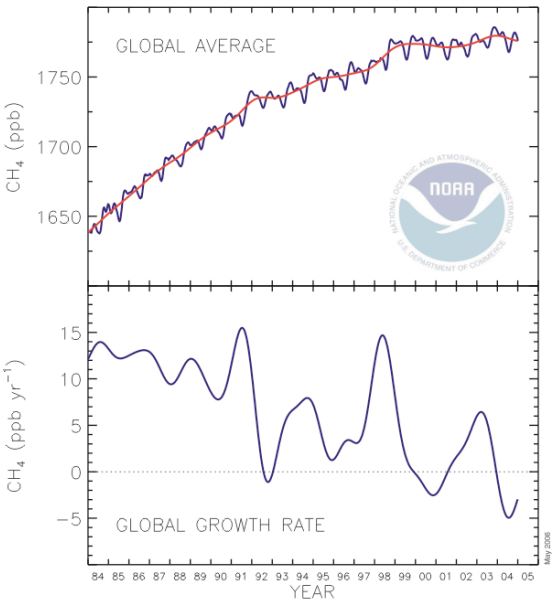

Figure 1. The decrease in the methane growth rate. Top: Global average methane mixing ratios (blue line) determined from the NOAA/GMD cooperative air sampling network (since 1984). The red line represents the long term trend. Bottom: Global average growth rate for methane. Source: Dr. Ed Dlugokencky, NOAA/ESRL; http://www.esrl.noaa.gov/gmd/.

Remarkably, the methane growth rate has decreased markedly since the early 1990s, and global concentration levels have remained relatively constant since 1999

the question on how global methane concentrations will develop in the coming decades better insight is required in the global methane budget. Table 1 summarizes current estimates[5] for the most important terms in the global methane budget. Anthropogenic source estimates are mainly based on socio-economic statistics.

Since the launch of ESA's environmental satellite ENVISAT in 2002, with onboard the German-Dutch-Belgian instrument SCIAMACHY, methane observations are being made using spaceborne shortwave infrared absorption spectroscopy that allow the global detection of spatial and temporal variations in atmospheric methane concentrations including variations near the surface. These observations enable identification of emission distributions, which is particularly worthwhile over tropical land regions that are poorly sampled by existing surface networks. This was the subject of a paper by Frankenberg et al., in cooperation with KNMI, which appeared in Science in 2005. Here the main findings of this paper are highlighted.

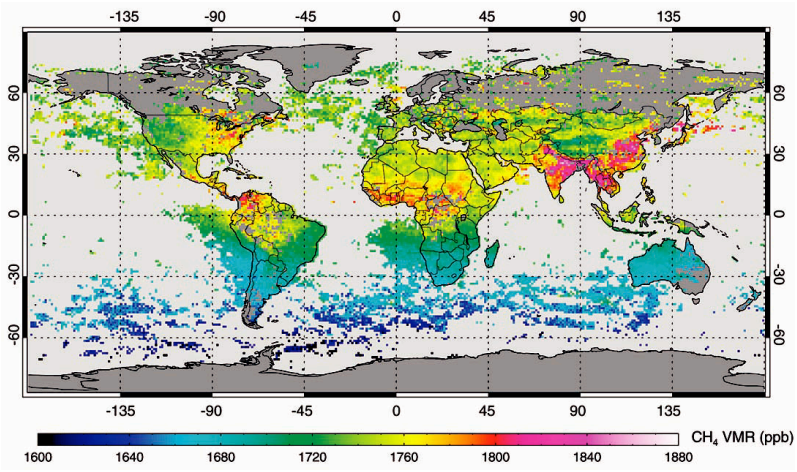

Figure 2. The unequal global distribution of atmospheric methane showing, amongst others, significant sources of methane over Asia. The figure is based on SCIAMACHY measurements of column-averaged methane volume mixing-ratios (VMR) in units of parts per billion (ppb). The measurements are averaged over the time period of August through November 2003 on a 1°x1° horizontal grid. At least 5 measurements (up to 150) are taken for each grid cell. Only few observations are available over the ocean, since low ocean reflectivity substantially reduces the quality of the retrieval leading, in turn, to unreliable measurements that are discarded. Occasionally, sun glint or clouds at low altitudes allow measurement over the ocean.

SCIAMACHY methane observations

Methane not only absorbs thermal radiation from the Earth system causing radiative forcing, but also solar radiation in the near-infrared. Hence, it can be measured by means of differential optical absorption spectroscopy (DOAS). The SCIAMACHY (SCanning Imaging Absorption spectroMeter for Atmospheric CHartographY) instrument onboard ESA's European environmental research satellite ENVISAT records the intensity of solar radiation, reflected from the Earth's surface or the atmosphere, in more than 8000 spectral channels between 240-2390 nm. ENVISAT operates in a nearly polar, sun-synchronous orbit at an altitude of 800 km, crossing the equator at 10:00 AM local time. In nadir mode the instrument points down almost perpendicular to the Earth's surface, detecting reflected sunlight. The spatial extent of the ground pixels of the near-infrared spectrometers is 60 km (East-West) by 30 km (North-South). Global coverage is achieved every six days. The SCIAMACHY column-averaged dry volume mixing ratio (VMR) of CH_4 is derived from the ratio of the retrieved CH_4 and CO_2 vertical columns, multiplied by a constant global and annual mean CO_2 column-averaged VMR of 370 ppm. The measured CO_2 vertical column is used as a proxy for the changes in the light path by orography, (partial) cloud cover and aerosols. A minor retrieval bias is introduced because the CO_2 column-averaged VMR varies globally and seasonally over a range (minimum to maximum) of about 11 ppmv or 3%. Using a lower threshold for the CO_2 vertical column, measurements can be discarded exhibiting substantial cloud cover at altitudes significantly above the ground. Details on the retrieval, data selections and error estimates are described elsewhere[6,7,8].

A resulting subset of SCIAMACHY column-averaged methane concentrations for the time period from August to November 2003 is shown in Figure 2. In comparison to surface concentrations column-averaged methane concentrations exhibit less variation and are slightly lower due to reduced methane concentrations in the stratosphere. The latitudinal gradient is clearly seen. It is strongest across the Inter-Tropical Convergence Zone (ITCZ). Strong regional methane enhance-

Unexpectedly high methane concentrations over tropical rainforests reveal that emission inventories considerably underestimate methane sources in these regions during the time period of investigation

ments are observed over the Gangetic plains of India, South-East Asia and parts of China. According to emission inventories, these regional sources in this time period can be attributed to rice cultivation, and, to a lesser extent, to domestic cattle (ruminants). Wetlands presumably cause the observed high abundances in central Africa and Manchuria in China. Fossil fuel production can be associated with enhanced methane over the industrialised Yellow-river basin in China and the Appalachian basin (coal mining) in the eastern USA. Waste-treatment related emissions are likely to contribute in populated areas.

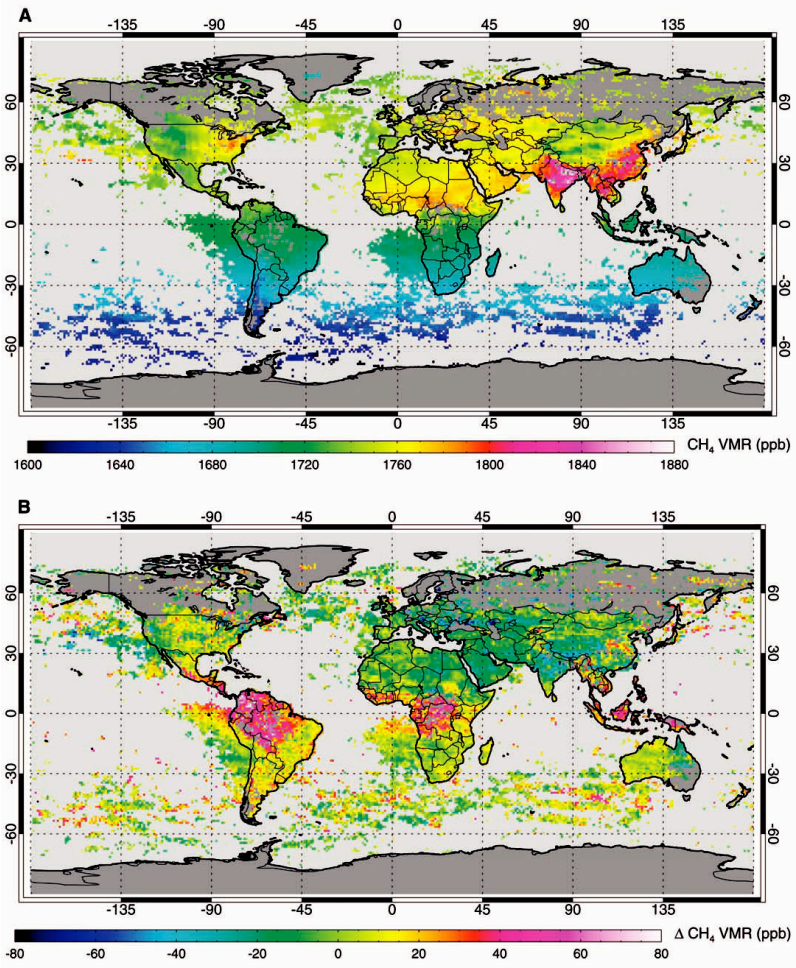

Figure 3. The sources of methane in tropical areas have been systematically underestimated. This conclusion could be drawn from simulation of the SCIAMACHY methane observations with a model (upper panel). The red and purple areas in the lower panel show where most important differences with the model (our current understanding) are found. Units as in Figure 2.

Unexpectedly high methane concentrations over tropical rain forests

To further substantiate the interpretation of the observations these were compared with methane concentration fields simulated using the global chemistry-transport model TM3 that takes current emission inventories into account[9]. In Figure 3 the upper panel shows the modelled fields and the lower panel shows the absolute differences with the SCIAMACHY observations. Modelled enhancements in the USA and Asia as well as the north-south gradient strongly resemble SCIAMACHY observations in magnitude and spatial extent. Some of the observed enhancements can be traced to long-range transport, e.g. over the Pacific, east of Japan. While the general agreement between the measurements and the model is very good, there are discrepancies in India and in the tropics (Figure 3, lower panel). The measured lower abundances over India probably indicate that the applied rice emissions in the model (amounting to 80 Tg/year) are an overestimation.

In the tropics SCIAMACHY observations are up to 4% (70 ppb) higher than predicted by the model. This can be explained either by tropical methane emissions not considered in the model, a regional CO_2 depression relative to the annual global mean, or a combination of both. It was found that the discrepancy cannot be attributed to a retrieval error dependent on solar zenith angle, light-path changes or albedo. Also a model bias, such as an underestimation of the stratospheric methane abundances or large errors in the modelled distribution of OH radicals, could be excluded. Although CO_2 flux estimates in the tropical landmasses are uncertain, the required depression in the CO_2 column of 3-4% would be of an improbably high magnitude. Hence, it was concluded that tropical CH_4 sources in the model have been underestimated.

A strong spatial correlation was found between the tropical discrepancies and the presence of broadleaf evergreen forest. Model simulations indicate that an additional tropical source of around 30 Tg over the considered time period (August-November) is needed if the discrepancy is fully to be assigned to methane

sources. For comparison: the tropical source in our model is 45 Tg. An additional methane source of 30 Tg in four months is large but can be accommodated by the uncertainties in the global budget (Table 1). It is important to note that surface methane observations are not in disagreement with an additional tropical source. Methane emitted in the tropics is generally rapidly uplifted by convection, so that the surface stations, which are located at remote ocean sites, are only to a limited extent sensitive to these emissions.

What are potential candidates for the enhanced tropical source? Wetlands, biomass burning, termites, cattle breeding in pastures? Or maybe a hitherto unknown methane source that might be directly related to the broadleaf evergreen forest? Recently, a hitherto unknown plant source was reported[10]. Termites constitute a significant but poorly constrained tropical methane source. Tropical fires are characterized by a molar CH_4/CO_2 ratio that is more than twice the ratio of their respective background concentrations. Hence, the SCIAMACHY observations are sensitive to these fires. Wetland emissions, in particular in the Amazon Basin, appear to be underestimated in the TM3 model. However, the investigated period coincides with the dry season in most of the tropics, when wetland emissions are supposed to be lowest. In the dry season unaccounted biomass burning can contribute to the discrepancy. Further validation measurements and process-based investigations for the considered season in the evergreen forests of tropical South America, Africa and Indonesia are needed to conclude which source type(s) is/are responsible for the discrepancies between the observations and model simulations over these areas.

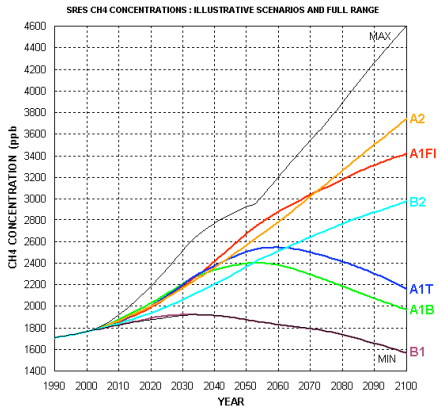

Figure 4. Illustrative CH4 concentrations in the 21th century for the six groups of IPCC/SRES emission scenarios applied in the 3rd and 4th IPCC assessment reports; http://www.ipcc.ch/pub/pub.htm.

Conclusion and Outlook

In conclusion, SCIAMACHY methane observations have become available which show large-scale patterns of anthropogenic and natural methane emissions. Unexpectedly high methane concentrations over tropical rainforests reveal that emission inventories considerably underestimate methane sources in these regions during the time period of investigation (August-November 2003).

Without improved understanding of the relative contributing factors to the trend in methane over the past decades it is hard to make predictions for the future. Several counteracting effects are likely to mask future changes in anthropogenic sources, natural sources, and chemical lifetime, similar as has been suggested for the recent past[9,11]. Methane concentration scenarios in climate assessments so far have been based on IPCC/SRES anthropogenic methane emission scenarios, such as presented in Figure 4. However, there is no doubt that future methane concentrations will as much depend on changes in natural emissions and chemical lifetime.

The EU project HYMN (2006-2009), lead by KNMI, will further contribute to our understanding of the methane budget, variability, and trend. Improved methane emission distributions can be expected from inverse modelling[12,13]. Within HYMN 4D-var data assimilation techniques will be applied to better constrain methane sources based on the SCIAMACHY data record. The framework of the global climate model EC Earth will allow better studying of the chemistry-climate interactions for methane. These include direct forcing, feedbacks via natural sources and OH, and impacts on stratospheric water and the ozone layer.

1) Bousquet, P. and 17 co-authors, 2006. *Contribution of anthropogenic and natural sources to atmospheric methane variability.* Nature, **443**, 439-443. doi:10.1038/nature05132
2) Dlugokencky E.J., S. Houweling, L. Bruhwiler, K.A. Masarie, P.M. Lang, J.B. Miller and P.P. Tans, 2003. *Atmospheric methane levels off: Temporary pause or a new steady-state?* Geophys. Res. Lett., **30**, 1992. doi:10.1029/2003GL018126
3) Fiore, A.M., L.W. Horowitz, E.J. Dlugokencky and J.J. West, 2006. *Impact of meteorology and emissions on methane trends, 1990–2004.* Geophys. Res. Lett., **33**, L12809. doi:10.1029/2006GL026199
4) Rohrer, F. and H. Berresheim, 2006. *Strong correlation between levels of tropospheric hydroxyl radicals and solar ultraviolet radiation.* Nature, **442**, 184-187. doi:10.1038/nature04924
5) Houweling, S., T. Röckmann, I. Aben, F. Keppler, M. Krol, J.F. Meirink, E.J. Dlugokencky and C. Frankenberg, 2006. *Atmospheric constraints on global emissions of methane from plants.* Geophys. Res. Lett., **33**, L15821. doi:10.1029/2006GL026162
6) Frankenberg, C., U. Platt and T.Wagner, 2005. *Iterative maximum a posteriori (IMAP)-DOAS for retrieval of strongly absorbing trace gases: Model studies for CH_4 and CO_2 retrieval from near infrared spectra of SCIAMACHY onboard ENVISAT.* Atmos. Chem. Phys., **5**, 9-22.
7) Frankenberg, C., J.F. Meirink, M. van Weele, U. Platt and T. Wagner, 2005. *Assessing methane emissions from global space-borne observations.* Science, **308**, 1010-1014. doi:10.1126/science.1106644
8) Frankenberg, C., J.F. Meirink, P. Bergamaschi, A.P.H. Goede, M. Heimann, S. Koerner, U. Platt, M. van Weele and T. Wagner, 2006. *Satellite chartography of atmospheric methane from SCIAMACHY on board ENVISAT: Analysis of the years 2003 and 2004.* J. Geophys. Res., **111**. doi:10.1029/2005JD006235
9) Dentener, F., W. Peters, M. Krol, M. van Weele, P. Bergamaschi and J. Lelieveld, 2003. *Interannual variability and trend of CH_4 lifetime as a measure for OH changes in the 1979–1993 time period.* J. Geophys. Res., **108**, 4442. doi:10.1029/2002JD002916
10) Keppler, F., J.T.G. Hamilton, M. Brass and T. Röckmann, 2006. *Methane emissions from terrestrial plants under aerobic conditions.* Nature, **439**, 187-191. doi:10.1038/nature04420
11) Dentener,F., M. van Weele, M.C. Krol, S. Houweling and P. van Velthoven, 2003. *Trends and inter-annual variability of methane emissions derived from 1979-1993 global CTM simulations.* Atmos. Chem. Phys., **3**, 73-88.
12) Bergamaschi, P. M. Krol, F. Dentener, A. Vermeulen, F. Meinhardt, R. Graul, M. Ramonet, W. Peters and E.J. Dlugokencky, 2005. *Inverse modelling of national and European CH4 emissions using the atmospheric zoom model TM5.* Atmos. Chem. Phys., **5**, 2431-2460.
13) Meirink, J.F., H.J. Eskes and A.P.H. Goede, 2006. *Sensitivity analysis of methane emissions derived from SCIAMACHY observations through inverse modelling.* Atm. Chem. Phys., **6**, 1275-1292.

The impact of emissions from shipping, aviation and road traffic on atmospheric composition and climate

Peter van Velthoven

Introduction

Fossil fuel combustion by aviation, shipping and road traffic contributes about one fifth of the total global anthropogenic emissions of CO_2. These emissions are growing more rapidly than those by other sectors such as power generation and industry. This rapid growth could make it difficult to meet the emission targets agreed upon within the EU, the Kyoto Protocol, and its possible follow-up. In addition to CO_2, the transport sectors also emit nitrogen oxides (NO_x=NO+NO_2), carbon monoxide (CO), and hydrocarbons (HCs) that lead to further perturbations of the atmospheric concentrations of the greenhouse gases ozone and methane. The emissions of particles and particle precursors by the transport sectors change the optical depth and properties of aerosols, which affects the radiation balance of the atmosphere regionally. The total climate impact of aviation emissions (excluding the uncertain impact on natural clouds) was estimated to be a factor 2-3 higher than that of CO_2 from aircraft alone. While the climate impact of the aviation sector has already been assessed quite extensively, e.g. in the IPCC Special Report on Aviation and the Global Atmosphere[1)], the impact of other modes of transport has received much less attention. Calculation of the individual impacts of sectors would allow an intercomparison as well as an evaluation of the efficacy of possible mitigation measures.

Shipping emissions occur in a relatively clean environment and it is not clear to what extent this affects their impact on climate. Until recently, also the impact of road traffic emissions was quite uncertain because of uncertainty about vehicle emission factors, and lack of information about road traffic intensities in developing countries.

KNMI participates in the EU Integrated Project Quantify (Quantifying the Climate Impact of Global and European Transport Systems; see http://www.ip-quantify.eu), which aims at reducing these uncertainties and quantifying the impact of the transport sectors on atmospheric composition and climate. The Port of Rotterdam participates in the project as an advisor for shipping. Within Quantify new emission inventories for road transport, aviation and shipping have been constructed for the year 2000 as well as emission scenarios up to 2100. The year 2000 emissions have been used as input to atmospheric chemistry models, such as the KNMI TM4 model, to calculate the impact of the transport sectors on the global distributions of the greenhouse gases ozone and methane. Here we summarize some of the first findings.

Emissions by transport modes

Emissions from fossil fuel combustion by aviation (~2%), shipping (~14%) and road traffic (~22%) contribute together about 38% of the total global anthropogenic emissions of NO_x (excluding biomass burning). Road traffic has been estimated to contribute between about 8-15 % of the total emissions of CO. The contributions of shipping and aviation to global CO emissions are estimated to be much smaller, likely due to more efficient fuel combustion.

Road traffic emissions occur mostly over the land surfaces of the eastern US, Europe, the Far East and India. In these regions also other, non-traffic, sources are important. Ship emissions are largest over the North Atlantic and along the coastlines of the US, Europe, and East Asia. Aviation emissions peak over the east and west coasts of the US, and Western Europe. At upper levels the aircraft emissions in the North Atlantic Flight Corridor constitute an important perturbation. Overall, the east coasts of the US and Asia, and Western Europe, including the North Sea, are regions with a relatively high emission contribution by transport.

Model simulations

In order to calculate the current impact of aviation, shipping and road traffic, five simulations were performed with the atmospheric chemistry models involved in Quantify: a) a base simulation b) three simulations with aviation, shipping and road traffic emissions respectively reduced by 5% c) a simulation with the emissions from all transport modes (aviation+shipping+road traffic) reduced by 5%. It was chosen to apply 5% perturbations, instead of 100% ones, because atmospheric ozone chemistry is non-linear for perturbations where e.g. road traffic is

completely switched off. The relative impact of the different transport sectors on ozone and methane for the present-day background composition of the atmosphere was obtained by scaling back to 100% perturbations. The fifth simulation allowed us to check the validity of the assumption of linearity and additiveness for the perturbations. This assumption was found to be satisfied almost everywhere to within 1%. As background emissions the EDGAR3.2 FT 2000 emissions described by Olivier et al.[2] (see also *http://www.mnp.nl/edgar*) were used. The production of NO_x by lightning in the models was scaled to 5 Tg (N)/year, which is in the range of current best estimates.

The simulations for the year 2003 were analysed but the models were run from January 2002 in order to allow for sufficient spin-up of the new emissions. The results of the base simulation were also used to evaluate the models against observations for 2003 collected in the ETHmeg observational database (http://www.megdb.ethz.ch). This model evaluation against ozone soundings showed that the KNMI TM4 model was performing relatively well with respect to tropospheric ozone in comparison to other European models. One of the reasons may be that a significant improvement in the description of the stratospheric influx of ozone has been implemented recently by Van Noije et al.[3]. TM4 was underestimating tropospheric ozone over Africa in 2003, perhaps due to an underestimate of NO_x emissions in the EDGAR3.2 FT2000 biomass burning inventory which is based on the Global Fire Emissions Database (GFED) constructed by Van der Werf et al.[4]. The emission factor for NO_x in EDGAR3.2 FT2000 was taken from a recent update by Andreae (pers. comm., 2004) yielding a 40% lower value for savannah fires than in previous inventories that used estimates made by Andreae and Merlet[5].

Effects on global ozone and methane

Figure 1 shows the zonal mean distribution of ozone and the perturbations caused by aviation, road traffic, shipping, and all transport modes together, as calculated by the TM4 global atmospheric chemistry model for July 2003. Although the NO_x emissions from aviation are an order of magnitude smaller than those from road traffic and shipping, they cause the largest ozone perturbation. This is because the lifetime of NO_x increases with height, making catalytic ozone formation by NO_x more efficient in the upper troposphere and lowermost stratosphere. The ozone perturbation due to aviation thus maximizes at cruise altitudes in the northern hemisphere. Road traffic emissions have a significant effect in the mid-latitude upper troposphere in summer because they can be rapidly transported upward by summertime convection over warm continental surfaces. In winter (not shown) their impact on the upper troposphere is much smaller. Ship emissions are transported much less efficiently upward than road traffic emissions because there is much less convection over the oceans than over land at mid-latitudes. However, there is some upward transport of ship emissions by tropical deep convection, giving a relatively more important contribution from shipping to tropical upper tropospheric ozone. As a result of the geographical distribution of all emissions, the increase of the ozone column due to transport is largest in the northern extra-tropics (north of 30°N), with a regional maximum of about 3.5 DU over the central North Atlantic in January, and of about 4.5 DU over western Europe in July.

The lifetime of methane in the base simulation with TM4 was 9.1 years. Aviation reduces this lifetime by about 0.8%, road traffic by about 1.9%, and shipping by about 4.5%. Especially, ship emissions are quite effective in reducing methane levels because they occur in the relatively clean marine environment. Hence, emissions by transport have counteracting effects on ozone and methane. Globally averaged the ozone perturbation dominates, giving a net positive radiative forcing (warming). However, it should be noted that the ozone and methane perturbations have different geographical patterns, so that even a zero net radiative forcing might still lead to significant regional climate changes.

Acidification

The ultimate fate of nitrogen and sulphur compounds emitted by transport modes is removal by dry deposition to the earth's surface or by wet deposition by precipitating clouds. Since sources and sinks of nitrogen and sulphur more or less balance when considering a full year, total annual deposition is almost equal to the total emissions for each sector. Road traffic annually emits about 6.8 Tg N and about 2.2 Tg S, and shipping emits about 4.4 Tg N and about 6 Tg S

Emissions by transport have counteracting effects on ozone and methane

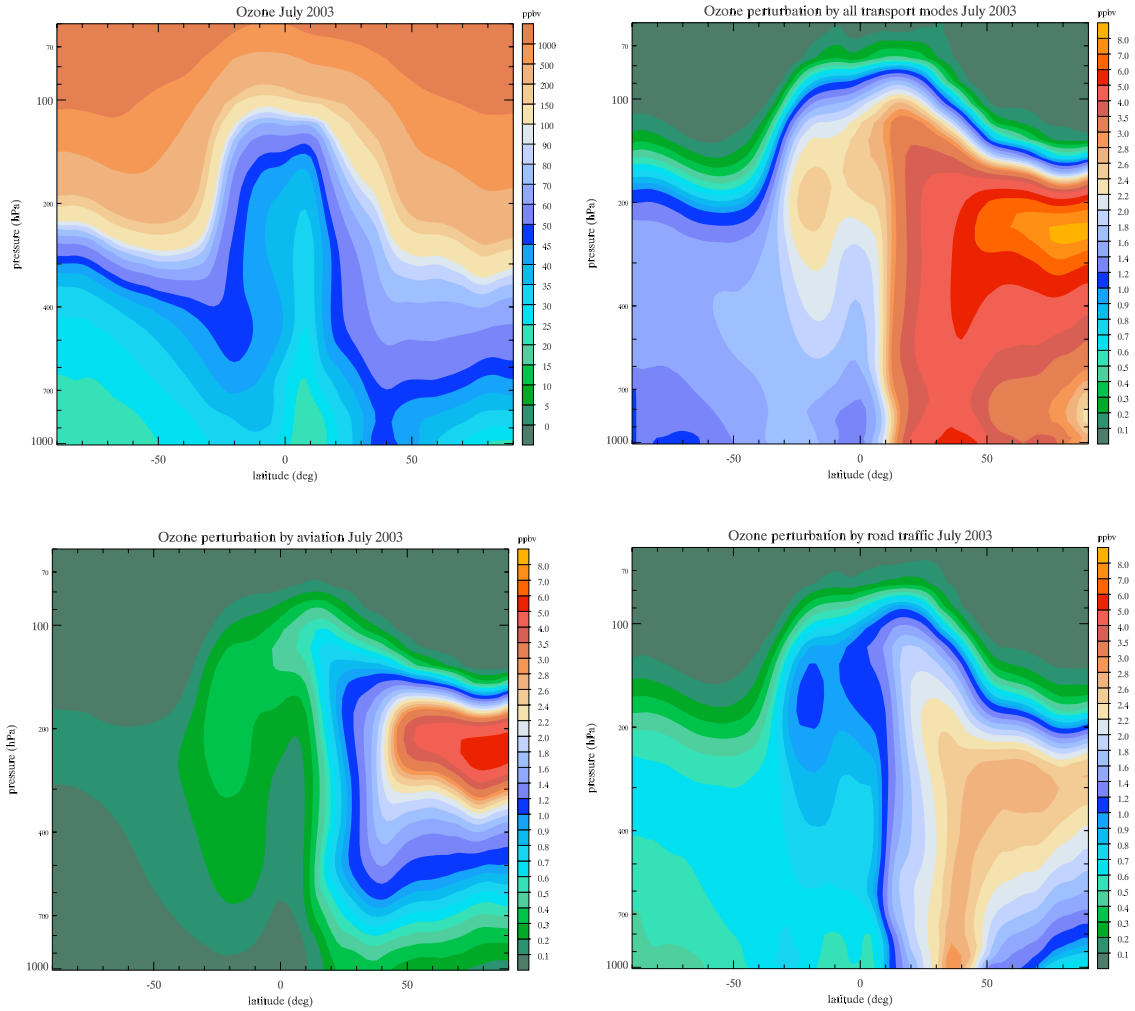

Figure 1. Zonal mean background distribution of ozone, and the perturbations caused by aviation, road traffic, shipping, resp. all transport modes together, for July 2003. Units are ppbv. The colour scales of the perturbation plots are identical, but different from the plot of the background distribution.

compounds. In view of its total emission of about 0.76 Tg N and 0.07 Tg S, aviation is much less relevant for acidification than road traffic and shipping. The calculated deposition maps in Figure 2 show that the deposition of nitrogen compounds from transport is concentrated in a few specific geographical regions. The same is true for sulphur compounds emitted by the transport modes (not shown). Most nitrogen deposition occurs over Western Europe and the east coasts of the US and Asia, close to the major emission sources from shipping and road traffic. Due to emissions from transport in total about 12 Tg N and about 8 Tg S is deposited globally. This is about one tenth of the total global sulphur deposition and about a quarter of the total global nitrogen deposition.

Conclusions and outlook

Emissions by the transport sector (aviation, road traffic and shipping) are of concern because they grow more rapidly than those from other sectors. The emissions of NO_x by transport lead to an increase in ozone in the northern extratropical troposphere and a global decrease in methane. The effect of NO_x emissions by shipping on methane was larger than expected, probably because they occur in a relatively clean environment. In summer, road traffic emissions have an appreciable impact on ozone up to the tropopause due to upward transport by convective clouds over land. The acidifying effects of emissions by transport are mostly concentrated in a few regions, including Western Europe and the east coast of the US and Asia.

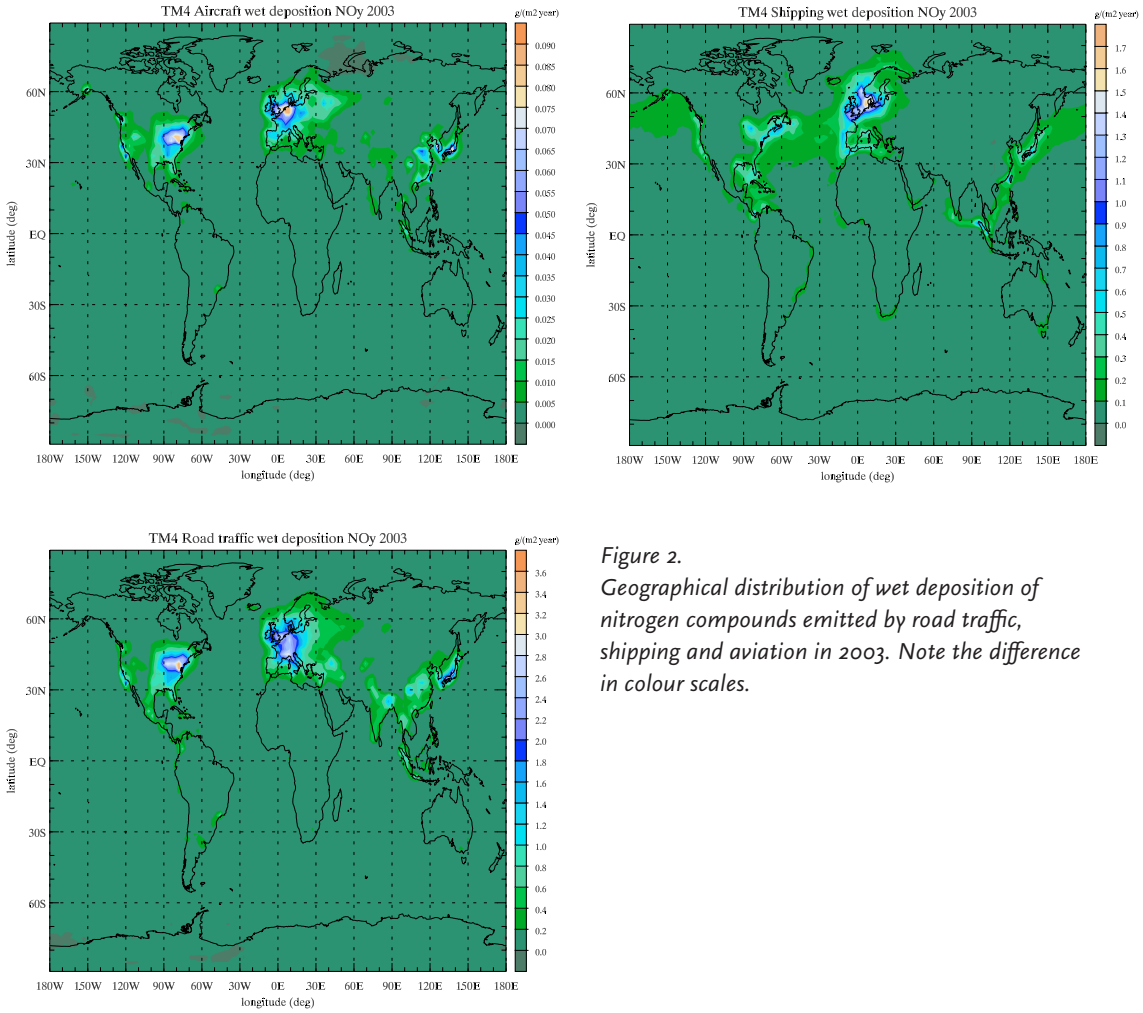

Figure 2.
Geographical distribution of wet deposition of nitrogen compounds emitted by road traffic, shipping and aviation in 2003. Note the difference in colour scales.

The deposition of nitrogen (and sulphur) compounds from transport is concentrated in a few specific geographical regions

The 5 year EU project Quantify is now almost halfway. Following the calculation of the current impact also the future impact will be calculated based on scenarios linked to the IPCC SRES scenarios, but with timelines adapted to the technical, economic and geographic development of the transport sectors. Also the influence of climate change on the calculated impacts will be assessed, and the effect of a few mitigation options will be quantified. For shipping it will be especially important to quantify the effect of the expected increase in Arctic routes, especially during fall, winter and spring when ozone and other pollutants have relatively long lifetimes, and thus could cause an appreciable acceleration of Arctic climate warming[6]. Presently, ozone values in the Arctic are still a factor 2-3 smaller than at northern mid-latitudes.

1) IPCC, 1999. *Special report on Aviation and the Global Atmosphere.* Cambridge University Press.
2) Olivier, J.G.J., J.A. Van Aardenne, F. Dentener, V. Pagliari, L. Ganzeveld and J.A.H.W. Peters, 2005. *Recent trends in global greenhouse gas emissions: regional trends (1970-2000) and spatial distribution of key sources in 2000.* Environmental Sciences, **2**, 81-99.
3) Van Noije, T.P.C., A.J. Segers and P.F.J. van Velthoven, 2006. *Time series of the stratosphere-troposphere exchange of ozone simulated with reanalyzed and operational forecast data.* J. Geophys. Res., **111**, D03301. doi:10.1029/2005JD006081
4) Werf, G.R. van der, J.T. Randerson, G.J. Collatz and L. Giglio, 2003. *Carbon emissions from fires in tropical and subtropical ecosystems.* Global Change Biology, **9**, 547-562.
5) Andreae, M.O. and P. Merlet, 2001. *Emissions of trace gases and aerosols from biomass burning.* Global Biogeochemical Cycles, **15**, 955-966.
6) Shindell, D., G. Faluvegi, A. Lacis, J. Hansen, R. Ruedy and E. Aguilar, 2006. *Role of tropospheric ozone increases in 20th-century climate change.* J. Geophys. Res., **111**, D08302. doi:10.1029/2005JD006348

Improved forecasts of extreme weather events by future space borne Doppler wind lidar

Gert-Jan Marseille

Introduction

An important goal in operational weather forecasting is to reduce the number of forecast failures, in particular those with large socio economic impact. Forecast failures of high-impact weather are often due to lack of observations over data sparse areas, such as the Southern Hemisphere, Tropics and Northern Hemisphere oceans, over a prolonged period prior to the extreme event. International programmes such as the observing system research and predictability experiment (THORPEX[1]) show a growing interest in defining an observational network focussing on increased accuracy of high-impact weather forecasts. This network definition addresses fundamental questions related to observation strategies such as the relative merit of new polar orbiting satellites, giving a uniform global coverage of observations, versus e.g. targeting strategies where additional observations are constrained to pre-determined meteorologically sensitive areas. To answer these questions simulation experiments with state-of-the-art numerical weather prediction (NWP) models have proved great value to test future meteorological observing systems a priori on their ability to improve meteorological analyses and subsequently reduce the probability of forecast failures, which would make them a cost-effective investment.

A well established method is the Observing System Simulation Experiment (OSSE), but this requires many human and computational resources and strong international collaboration. Recently, a big step forward was made by the United States National Centers of Environmental Prediction (NCEP). A new set of OSSEs was prepared, based on a one-year high resolution synthetic true atmospheric state. This was generated by the European Centre for Medium-Range Weather Forecasts (ECMWF) by integrating the high resolution model over a one-year period, the so-called nature run. The research community working on data assimilation and the design of future observing systems will benefit from this effort since it provides a platform to participate in internationally collaborative OSSEs using the same nature run.

In this chapter, a new effective method, called Sensitivity Observing System Experiment (SOSE), is described to assess the impact of future observing systems for NWP. An example demonstrates the added value of future space borne Doppler wind lidar (DWL) to reduce forecast failures of extreme weather events.

SOSE – Sensitivity Observing System Experiment

For lack of an established methodology to test the potential impact of prospective extensions to the Global Observing System (GOS), a new method called SOSE was developed. Because the density of the GOS is non-uniform it is of interest to investigate the benefit of complementary observing systems filling its gaps. Forecast errors on the short term (up to 48 hours) are mainly due to the evolution of errors in the forecast initial state (analysis). A major component of SOSE is the determination of a so-called adapted analysis, also denoted as 'pseudo true atmospheric state', that

- improves the 2-day forecast,
- is realistic in the sense that the spatial structures of the analysis adaptation resemble those of real analysis errors,
- is not in conflict with the existing (real) observations.

To generate such a pseudo truth fulfilling these requirements a methodology has been developed based on adjoint sensitivity structures[2] that represent the part of the analysis error that grows most rapidly in time and potentially causing the large forecast failures if not observed. The pseudo true atmospheric state is subsequently used for the simulation of the prospective observing system(s), i.e. the atmospheric state is interpolated to the observation locations of these prospective observing systems to generate 'perfect' observations. Next, realistic instrument and representativeness errors are added to these perfect observations to generate the synthetic observations. These synthetic observations are used together with real observations from the existing GOS in a state-of-the-art NWP model to assess the potential added value of the prospective observing system. Note that the analysis adaptation that defines the pseudo-truth represents the part of the analysis error that is not observed by the existing network. Obviously, when the new observing system

is capable of (partly) resolving the analysis adaptation, the 2-day forecast will improve.

Unlike a full-blown OSSE, SOSE can be applied to real extreme events that were 'badly' forecast operationally and it only requires the simulation of the additional prospective instrument. This property makes SOSE an effective tool to define observation requirements to reduce deficiencies in the current GOS, e.g. to maximize the probability to observe rapidly evolving meteorological structures with a large forecast impact, as shown in Figure 1. The observation requirements may be used to define observation strategies such as the design of a network including prospective observing systems. An application of the SOSE method is the assessment of the impact of future space borne Doppler wind lidar.

Space borne Doppler wind lidar

Despite continuous progress in the observation of meteorological variables from space by satellites, the meteorological observing system still lacks a uniform global coverage of wind profile observations. It has been recognized for a long time that lack of wind profile observations over the oceans is a major deficit of the current observing system network. In particular over the oceans additional wind observations can improve weather forecasting substantially. The European Space Agency (ESA) Atmospheric Dynamics Mission (ADM), featuring the satellite named ADM-Aeolus[3] is a first step to fill in this gap and will provide wind profiles in otherwise data sparse areas (Figure 2) and thus may reduce the number of forecast failures. ADM-Aeolus is a demonstration mission scheduled for launch in 2009 and will be operational for three years.

ADM-Aeolus is a polar orbiting satellite carrying a Doppler wind lidar (DWL) for wind profile measurements all over the globe. A DWL emits laser light into the atmosphere and as the light propagates through the atmosphere part of the signal is scattered back to the instrument by atmospheric particles and molecules that are moving with the wind velocity. These moving particles cause the frequency of the backscattered signal to be Doppler shifted with respect to the transmitted signal. The time lag between the transmitted and received signal determines the distance of the scattering particle to the instrument. The frequency shift is related directly to the wind velocity along the laser beam line-of-sight (LOS). Consequently, ADM measures profiles of single horizontal line-of-sight (HLOS) wind components rather than the complete wind vector. The priority of this so-called explorer mission is on quality rather than quantity of retrieved winds. Anticipating on its success, there is a need to specify already wind observation requirements (both quality and quantity)

Forecast failures of high-impact weather are often due to lack of observations over data sparse areas

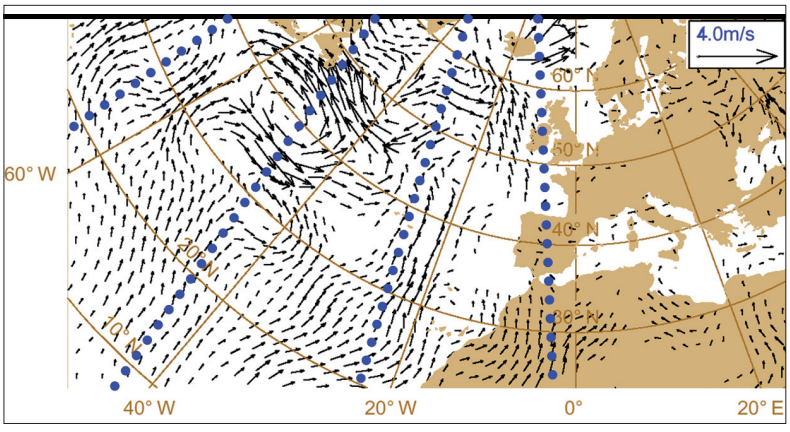

Figure 1. Typical 500 hPa wind structure over the North Atlantic not observed by the current global observing system, but causing a large forecast error over Europe 48 hours later. Overlaid, the sampling of future Doppler wind lidar profiles by the ADM-Aeolus mission.

Figure 2. Artist impression of the ESA earth explorer mission ADM-Aeolus that will provide a global coverage of wind information for the first time in history (courtesy ESA).

for the definition of an operational network of space borne DWL in the post-ADM era, beyond 2012, and projects have been initiated for this purpose.

In the PIEW (Prediction Improvement of Extreme Weather) project the SOSE method was used to test various DWL scenarios[4] on their capability to sample meteorologically sensitive areas not well captured by the current GOS, in particular over the Northern Hemisphere oceans. These scenarios included

- Dual-perspective; the data coverage of this scenario is identical to ADM-Aeolus but the complete wind vector is determined by measuring two line-of-sights with a 90 degree difference in azimuth angle,
- Tandem-Aeolus; a tandem of two ADM-Aeolus satellites, with one line-of-sight, and in one orbit plane separated by 180 degrees, giving twice the coverage of Aeolus, as shown in Figure 3. The number of wind component profiles measured by this scenario is twice the number of only one ADM-Aeolus and equals the number of singlecomponent profiles of the dual-perspective scenario.

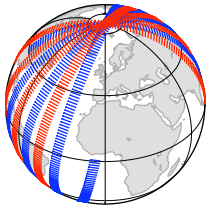

Figure 3. 12 Hours observation coverage for a tandem-Aeolus DWL scenario. Arrows start at measurement locations and point along the line of sight. Blue and red arrows correspond to the two Aeolus satellites.

To determine the measure of impact by the SOSE method, forty cases were selected from a database of worst ECMWF forecasts issued during the period 1998-2004, covering all seasons. For each case and both DWL scenarios a SOSE was conducted. Figure 4 shows the mean impact of the additional wind observations on the analyses and Figure 5 the subsequent impact on the 2-day forecasts. From these and other experiments it was concluded that Aeolus is capable to resolve part of the analysis adaptation in the data sparse areas giving an improved forecast after 2 days and beyond. In addition, it was found that

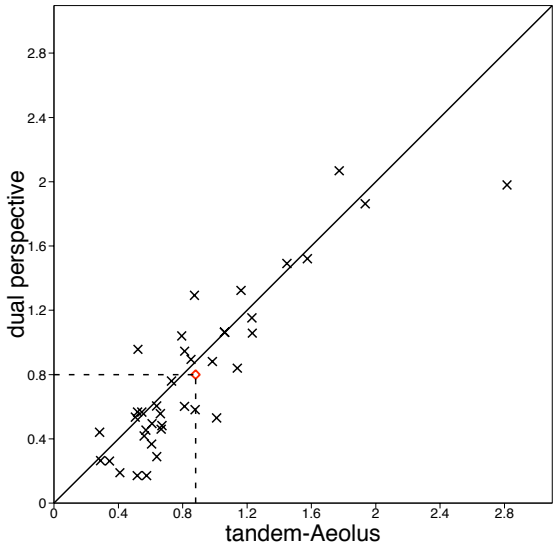

Figure 5. Scatter plot of 2-day forecast improvement of 500 hPa geopotential height (m) for the tandem-Aeolus and dual-perspective DWL scenarios. Each cross corresponds to one of the 38 cases; the red diamond denotes the mean value. The added value of the tandem-Aeolus scenario is larger than the dual-perspective scenario on average.

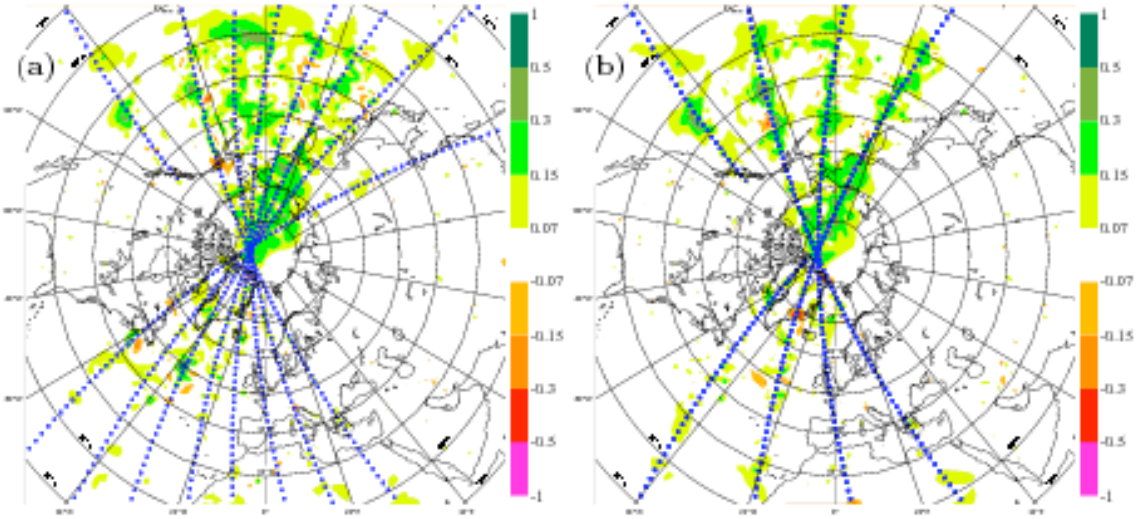

Figure 4. Mean 500 hPa wind (m/s) analysis impact for the tandem-Aeolus (left panel) and dual-perspective (right panel) DWL scenarios. Green/red spots denote positive/negative impact; the blue spots denote the DWL observation locations.

ADM-Aeolus is a first step to fill in this gap and will provide wind profiles in otherwise data sparse areas

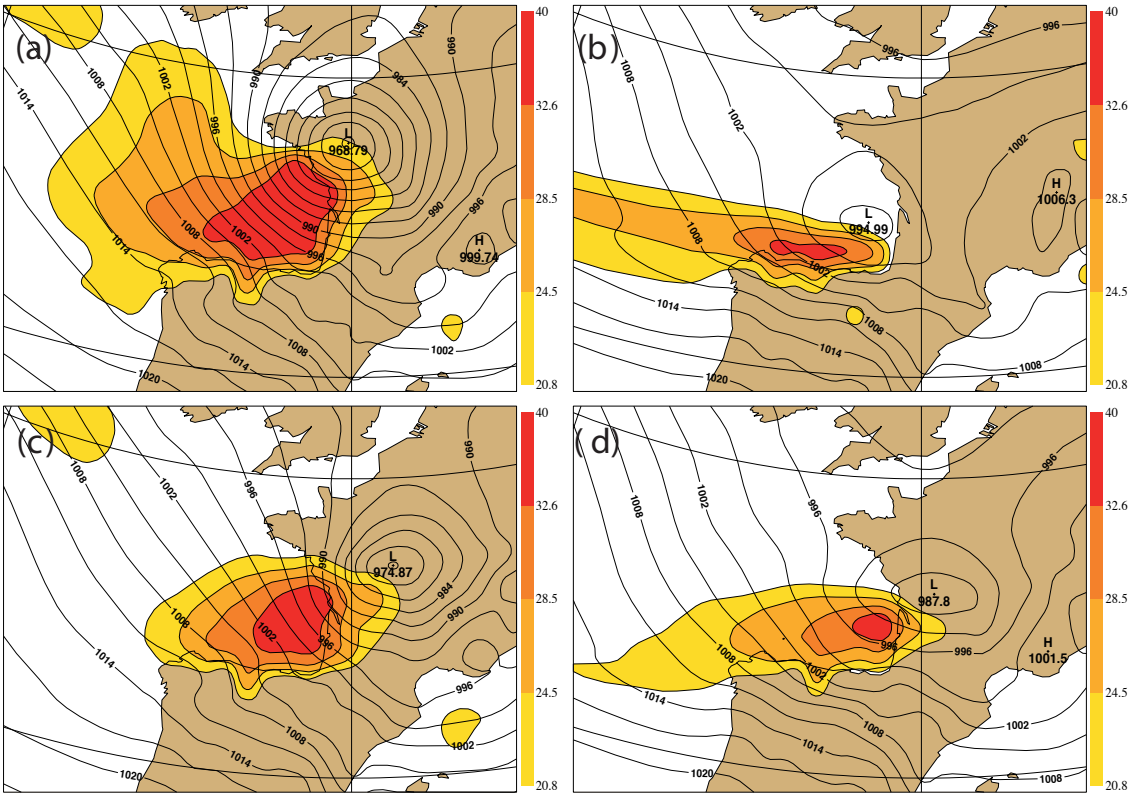

Figure 6. Christmas 1999 storm 'Martin'. Surface pressure and wind gust at verification time 27 December 1999 18UTC for: a) the verifying analysis, b) the control 48-hour forecast, c) the pseudo-truth 48-hour forecast and d) the DWL (tandem-Aeolus scenario) 48-hour forecast. Solid lines denote the mean sea level pressure with 3 hPa contour interval. Shaded areas denote the surface wind gust (m/s) covering the range 9-12 Bft.

maximum impact is obtained by spreading the available information over extended areas, as achieved by a tandem-Aeolus scenario, rather than focussing on larger but more localized analysis improvements as achieved by the dual-perspective scenario. It was also found that the additional impact of an additional third ADM-Aeolus to the tandem-Aeolus is less than for an additional second Aeolus in the same orbit, demonstrating redundancy when flying more Aeolus-type instruments.

The 1999 Christmas storms

The December 1999 Christmas period was characterized by two storms named 'Lothar' and 'Martin' causing much havoc in Western Europe. Almost all operational NWP models failed completely to forecast these storms even on the short (48-hour) term[5]. Here, we zoom in on the second Christmas storm 'Martin' that made landfall in Brittany (France) on 27 December 18 UTC (see Figure 6a), causing much damage over France and Germany in the following 24 hours. From Figure 6b it is clear that the 48-hour operational forecast from ECMWF starting on 25 December 18UTC completely failed to predict the location and intensity of the storm.

To answer the question whether additional DWL observations would have improved the forecast, the SOSE method was adopted and extended to a cycled mode implementation to generate a pseudo true trajectory[6]. This enables the simulation of DWL observations over a prolonged period prior to the forecast initial time and thus making full benefit of nowadays operational data assimilation systems to

propagate information from observations forward in time to next cycles in a constructive manner.

The forecast initiated with the 25 December 18UTC pseudo-truth represents the best achievable forecast in a cycled SOSE experiment and does predict a storm as shown in Figure 6c. Figure 6d shows that additional 60 hours of DWL observations from a tandem-Aeolus scenario over the period 23 December 06UTC until 25 December 18UTC improves the forecast substantially, reducing the forecast error by 62% relative to the maximum achievable reduction (from the pseudo-truth forecast). Although this result clearly demonstrates the added value of a DWL, the forecast in Figure 6d still does not predict a severe storm.

To complete this case, an ensemble experiment was conducted to quantify the probability of the occurrence of a severe storm. An ensemble of forecasts is generated by adding growing structures to the analysis. The subsequent spread in the ensemble forecasts is a measure for the predictability of the event. Two 50-member ensemble experiments were conducted, one for the control experiment including all existing observing systems (but without DWL), the so-called NoDWL experiment, and the other with synthetic DWL. For the NoDWL experiment 5 out of 50 members showed a storm in the Gulf of Biscay and over the French mainland in the 2-day forecast initiated at 25 December 18UTC. For the DWL experiment 11 members show a storm, meaning more than a doubling of the probability of forecasting this storm when DWL observations would have been available. For the 54-hour forecast, when the storm has moved further over the French mainland, again 5 members show a storm in the NoDWL experiment against 15 members in the DWL experiment, clearly demonstrating the substantial impact an additional DWL would have had to forecast the Christmas 1999 storm 'Martin'.

Conclusions and outlook

Simulation experiments using state-of-the-art NWP models demonstrate the high potential to test a priori prospective meteorological observing systems on their ability to improve meteorological analyses and subsequently to reduce the probability of forecast failures. A flexible, effective and computationally efficient experimental tool is provided by SOSE as discussed in this paper. SOSE has been used to test ADM-Aeolus and various optional post-ADM DWL scenarios on their capability to improve numerical weather forecasts. An example demonstrates that space borne DWL would have improved the forecast of the Christmas 1999 storm 'Martin' substantially. SOSE experimental results may be used to determine observation requirements culminating in instrument design concepts for prospective (space borne) observing systems to extend the GOS. New experiments based on SOSE are in preparation, in collaboration with United States institutes, focussing on the definition of an operational network of space borne Doppler wind lidar in the post-ADM era beyond 2012.

1) Shapiro, M. and A. Thorpe, 2004. *THORPEX International Science Plan, vs.3*. WMO/TD-No.1246, WWRP/THORPEX No.2, 57 pp.
2) Marseille, G.J., A. Stoffelen and J. Barkmeijer, 2008. *Sensitivity Observing System Experiment (SOSE) – A New Effective NWP-based Tool in Designing the Global Observing System*. Tellus **60A**.
3) Stoffelen, A., P. Flamant, E. Källén, J. Pailleux, J.M. Vaughan, W. Wergen, E. Andersson, H. Schyberg, A. Culoma, M. Endemann and P. Ingmann, 2005. *The Atmospheric Dynamics Mission for Global Wind Fields Measurement*. Bull. Amer. Meteor. Soc., **86**, 73-87.
4) Marseille, G.J., A. Stoffelen and J. Barkmeijer, 2008. *Impact assessment of prospective space borne Doppler wind lidar observation scenarios*. Tellus, **60A**.
5) Tijm, S., 2000. *HiRLAM en de kerststormen (in Dutch)*. Meteorologica, **9**, 1, 13-17.
6) Marseille, G.J., A. Stoffelen and J. Barkmeijer, 2008. *A cycled Sensitivity Observing System Experiment on simulated Doppler wind lidar data during the 1999 Christmas storm 'Martin'*. Tellus, **60A**.

Probabilistic 0-12 h forecasts of (severe) thunderstorms for the purpose of issuing a weather alarm

Maurice Schmeits, Kees Kok, Daan Vogelezang and Rudolf van Westrhenen

Introduction

To improve severe weather forecasting, KNMI has started a special programme, in which a number of research and non-research projects are included. One research project, KOUW (Probabilistic forecasts of thunderstorms for the purpose of issuing a weather alarm), is described here. Another one, MESOMOD, is described elsewhere in this report[1]. The non-research projects of the programme are aimed at better tuning of severe weather information to the needs and wishes of the user, at a clear and consistent communication to the user and media, and at a more dedicated role of the forecaster. In this chapter the most important results of the KOUW project are presented. Because the skill of severe thunderstorm warnings was unsatisfactory, the KOUW project was initiated. The goal of this project was to develop a probabilistic forecast system for (severe) thunderstorms to be used by forecasters as a tool to decide whether a weather alarm should be issued.

Method

In this project the technique of Model Output Statistics (MOS)[2] has been used to derive logistic regression[2] equations for the (conditional) probability of (severe) thunderstorms in the warm half-year (from mid-April to mid-October) in The Netherlands. The MOS technique consists of determining a statistical relationship between a predictand[i] (i.e. the occurrence of a thunderstorm in this case) and predictors[ii] from numerical weather prediction (NWP) model forecasts and possibly from observations. For 12 regions of about 90×80 km² each (Figure 1) and for forecast projections up to

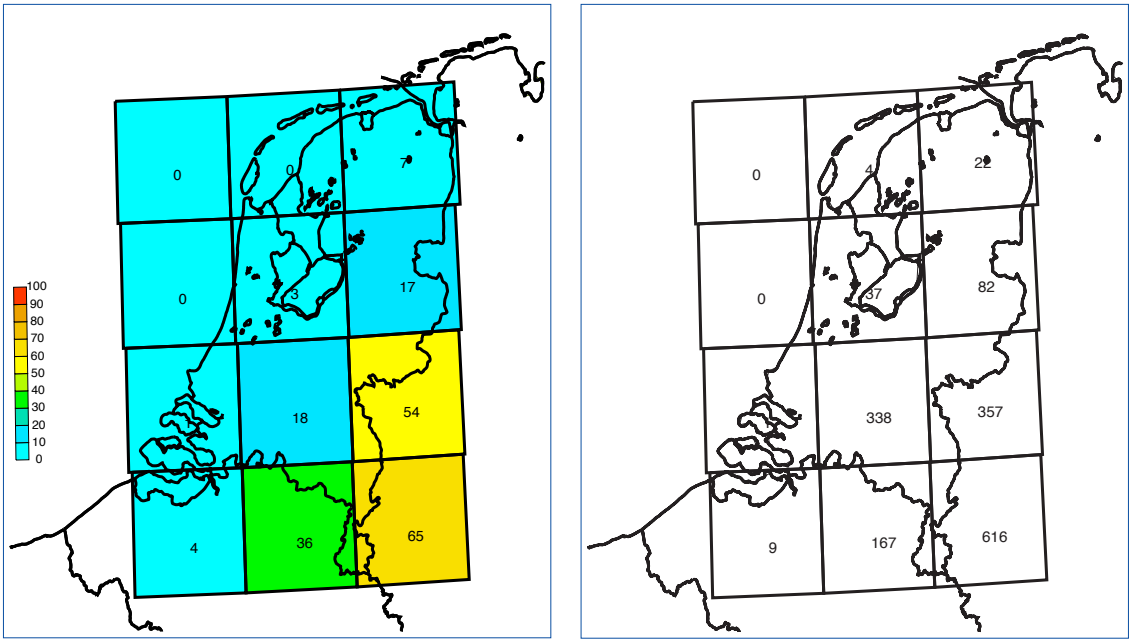

Figure 1. Left panel: 6-12 h conditional probability forecast (%) of maximum lightning intensity ≥ 200 discharges/ 5 min. valid for 15-21 UTC on June 25, 2006. The forecast is based on the 09 UTC run of the MOS system. Right panel: Maximum 5-min. lightning intensity, as detected by the SAFIR network, during the same period.

[i] *Definition of predictand: quantity to be forecast*

[ii] *Definition of predictor: quantity that has forecasting value for the predictand*

12 hours in advance (with 6-hour periods), we have developed these equations using several potential predictor sources. These sources not only consisted of combined (postprocessed) output from two NWP models, as in our previous study[3], but also contained an ensemble of 18 members of advected radar and lightning data for the 0-6 h projections[4]. As a source for the predictands, reprocessed lightning data from the SAFIR network[5,6] have been used. The system was made pre-operational at KNMI in the spring of 2006 and produces an update every 3 hours during the warm half-year.

Predictand definitions

Two predictands are defined, based on (reprocessed) SAFIR[5,6] lightning data. Herewith, both horizontal and vertical lightning discharges are taken into account. One predictand is defined as the probability of a thunderstorm (i.e. > 1 discharge in a 6-h period in a 90×80 km² region). The other predictand is defined as the conditional probability of a severe thunderstorm (with maximum intensity thresholds of 50, 100 and 200 discharges/ 5 min. in a 6-h period in a 90×80 km² region) under the condition that > 1 discharge will be detected in the same 6-h period in the same region. The two highest thresholds are only available for the 12-18, 15-21 and 18-00 UTC periods. The absolute probability of a severe thunderstorm can be computed by multiplying the conditional probability of a severe thunderstorm by the probability of a thunderstorm (> 1 discharge). Note that the predictand definition for severe thunderstorms is different from the one used in the operational severe thunderstorm forecast system[3].

Weather alarm criterion

The current weather alarm criterion for severe thunderstorms (≥ 500 discharges/ 5 min. in any area of 50×50 km²) is met only twice a year on average. For such a rare event it is impossible to derive skilful statistical equations. Therefore, we have investigated what the maximum intensity threshold is that renders a skilful system. This has led to the above mentioned predictand definitions. Not only the intensity thresholds in the KOUW-system are lower than the weather alarm threshold, but the area size is also a factor of 3 larger. The area size is larger, because the thunderstorm frequency would otherwise become so low (in the night and morning) that there would be too few thunderstorm cases left to derive statistical equations. On the other hand, the 90×80 km² regions in the KOUW-system are specified a priori, while the weather alarm criterion is defined for any area of 50×50 km².

Predictors

New compared to the operational thunderstorm forecast system[3] is the use of an ensemble of 18 members of advected radar and lightning data as potential predictor sources for the 0-6 h projections[4]. The lightning and radar images of 02.40, 05.40, 08.40, 11.40, 14.40, 17.40, 20.40 or 23.40 UTC have been used as initial conditions. Subsequently, both the lightning and the radar image are advected using the HIRLAM 700 hPa wind vectors together with vectors computed from previous radar images. Apart from these basic vectors, also vectors that are 25% longer and 25% shorter have been used and vectors whose direction deviates by +10 and -10 degrees, respectively. This leads to a total number of 18 ensemble members.

The remaining potential predictor sets consist of 17 thunderstorm indices, computed from the 22-km HIRLAM reforecasting dataset, ECMWF (postprocessed) direct model output (resolution: 0.5 degree) and the (co)sine of the day of the year. The dataset used to develop the application consists of July 2002 to July 2005 data (warm half-years only) with independent verification datasets consisting of July to mid-October 2005 and mid-April to mid-October 2006 data, respectively. Because the severe thunderstorm sample size is too small for each region separately, all 12 regions have been pooled in the severe thunderstorm forecast system.

After a selection process[4], the most important predictors in the thunderstorm forecast system turned out to be the percentage of the total number of advection ensemble members with ≥ 4 discharges (0-6 h projections only), the ECMWF 6-h convective precipitation sum, the HIRLAM Jefferson index, the HIRLAM CAPE of the most unstable level and the HIRLAM Boyden index (see Table 1 for definitions of the thunderstorm indices). The most important predictors in the severe thunderstorm forecast

Because the skill of severe thunderstorm warnings was unsatisfactory, the KOUW project was initiated

Thunderstorm index	Definition
Boyden index	$0.1(Z_{700} - Z_{1000}) - T_{700} - 200$
Bradbury index	$\theta_{w500} - \theta_{w850}$
Jefferson index	$1.6 \times \theta_{w925} - T_{500} - 11$
Convective available potential energy (CAPE)	$g \int_{LFC}^{LNB} \frac{T_v(\text{parcel}) - T_v(\text{environment})}{T_v(\text{environment})} dz$

Table 1. Definitions of a number of thunderstorm indices, where z is the (geopotential) height, T is the temperature (°C), θ_w is the potential wet-bulb temperature (°C), g is the acceleration due to gravity, LNB is the level of neutral buoyancy, LFC is the level of free convection, and T_v is the virtual temperature (K).

system turned out to be the HIRLAM Bradbury index, a number of predictors from the ensemble of advected lightning data (0-6 h projections only), the ECMWF 3-h convective precipitation sum and the HIRLAM Jefferson index. In the logistic regression [2] equations for the three different thresholds (50, 100 and 200 discharges/ 5 min.) the same predictors are used, but of course with different regression coefficients. The equations contain minimally 2 and maximally 5 predictors. The maximum number of predictors has been set to 5, because more than 5 predictors often appeared to result in overfitting.

Example case: June 25, 2006

Figure 1a shows an example of a probabilistic forecast of severe thunderstorms for 15-21 UTC on June 25, 2006 and Figure 1b shows the observed maximum 5-min. lightning intensity for the same period. In the morning the system already showed high probabilities of severe thunderstorms, especially in the south-eastern regions (Figure 1a). It is found that the 200 discharges/ 5 min. threshold was exceeded in 3 regions (Figure 1b). Inside the Netherlands the weather alarm criterion has not been reached, but just outside (within the most south-eastern region in Figure 1b) it has. In fact this was the only case in 2006 in which the weather alarm criterion was met anywhere within the total area of the 12 regions. Of course, (probability) forecasts cannot be verified using only one single case, so objective verification results for the independent datasets are presented here.

Verification

We conclude from the verification results for 2006 (Figure 2) that the overall skill of the MOS thunderstorm forecast system (> 1 discharge) is good compared to the 2000-2004 climatology. The average Brier skill score (BSS)[2] of the 6 land regions (EMN, MMS, EMS, WXS, MXS and EXS)[3] shows a clear diurnal cycle with the highest skill in the afternoon (12 and 15 UTC) and evening (18 UTC). The average BSS[2] of the 6 coastal regions (WXN, MXN, EXN, WMN, MMN and WMS)[3] shows a diurnal cycle as well, but with a smaller amplitude and a phase shift of approximately 12 h. This can be partly explained by the smaller and

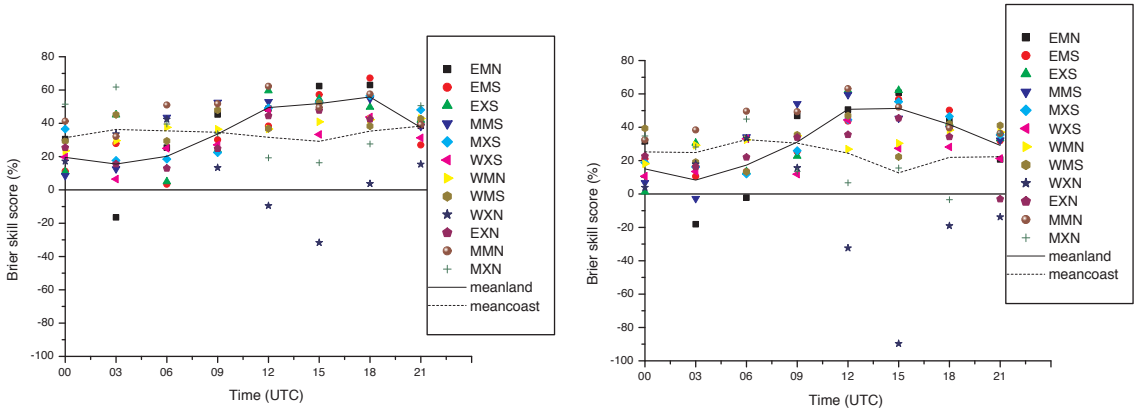

Figure 2. Brier skill score (BSS)[2] with respect to the 2000-2004 climatology, as a function of central verification time for the 8 runs of the MOS thunderstorm forecast system (threshold: 1 discharge) for all 12 regions (indicated by the different symbols). The solid (dotted) line represents the average BSS for the 6 land (coastal) regions (see text). The verification period is from 16 April to 15 October 2006. The left panel shows the 0-6 h forecasts and the right panel the 6-12 h forecasts.

different diurnal cycle in the occurrence of thunder - storms in the coastal regions compared to the land regions. The Brier skill scores for the 6-12 h forecasts (Figure 2b) are generally smaller than those for the 0-6 h forecasts (Figure 2a), as expected. Apart from the fact that the skill of a forecast system decreases with increasing forecast projections, the loss of the most important predictor for the 0-6 h projections (i.e. the percentage of the total number of advection ensemble members with ≥ 4 discharges) is expected to play a role as well. Finally, the Brier skill scores of this new thunderstorm forecast system are generally higher than those of the operational system[3] (not shown).

Severe thunderstorms were relatively rare in the warm half-year of 2006. Because the period July to mid-October 2005, in which their frequency was about the same as in the 2000-2004 period, was more representative, we have verified the MOS system for severe thunderstorms over both periods. In Figure 3 reliability diagrams[2] are shown for the 0-6 h forecasts of 5 runs of the MOS severe thunderstorm forecast system based on the lowest threshold

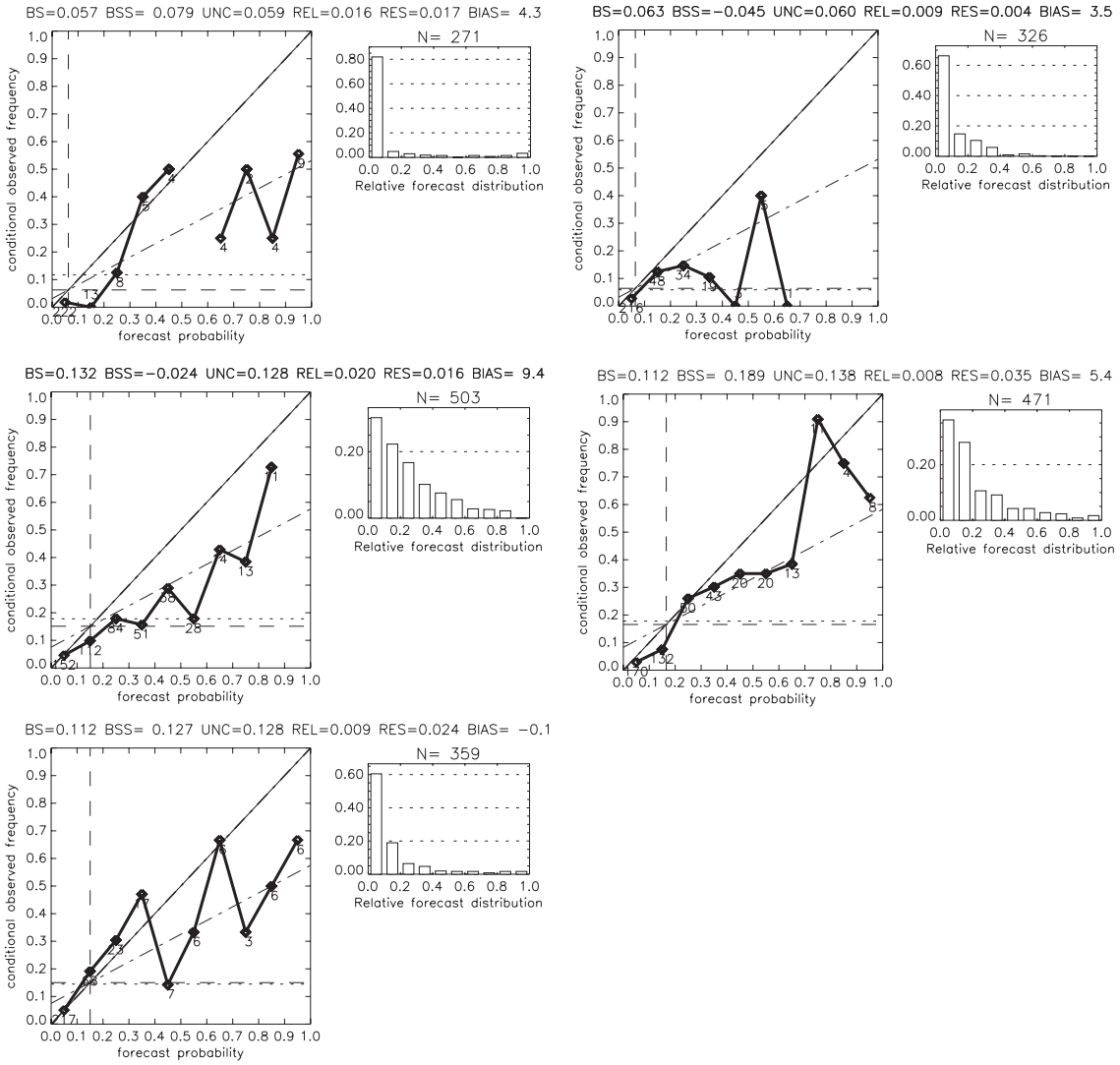

Figure 3. Reliability diagrams[2] for the 0-6 h forecasts of 5 runs of the MOS severe thunderstorm forecast system for the threshold of 50 discharges/5 min. The verification period is from 1 July to 15 October 2005 and from 16 April to 15 October 2006. In these diagrams the observed frequencies are shown as a function of forecast probabilities. The histograms indicate the frequency of the forecast probabilities. Valid for 00-06 UTC (upper left panel), 06-12 UTC (upper right panel), 12-18 UTC (middle left panel), 15-21 UTC (middle right panel) and 18-00 UTC (lower panel).

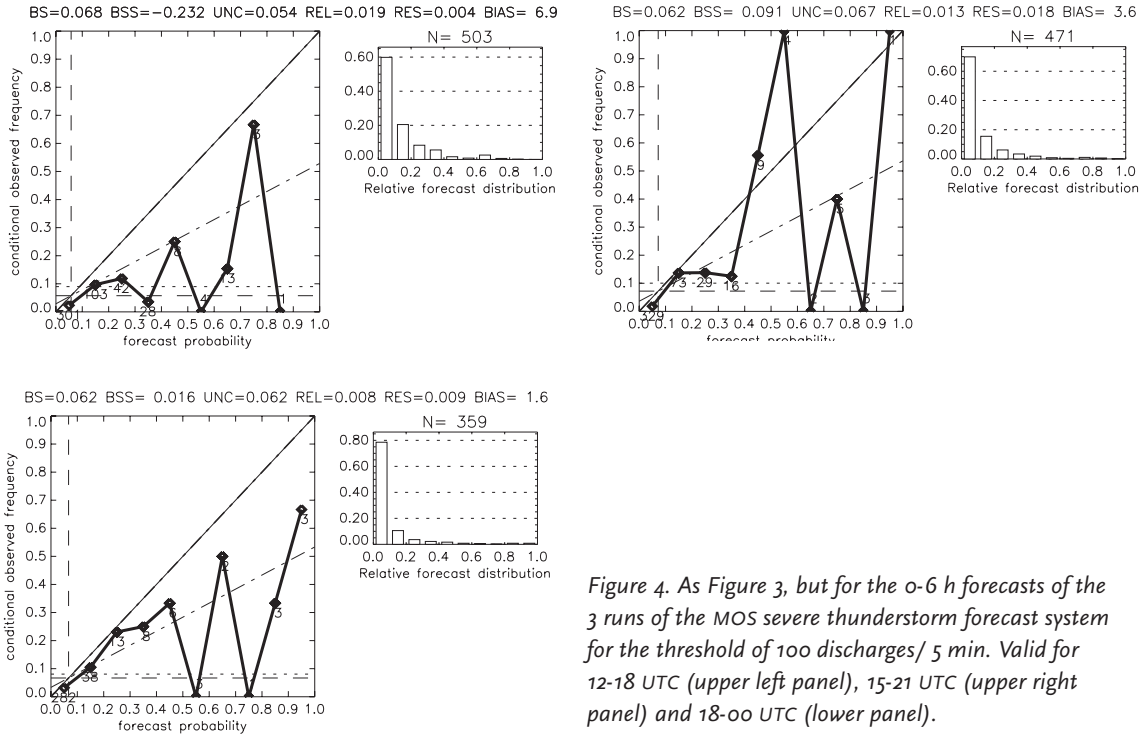

Figure 4. As Figure 3, but for the 0-6 h forecasts of the 3 runs of the MOS severe thunderstorm forecast system for the threshold of 100 discharges/ 5 min. Valid for 12-18 UTC (upper left panel), 15-21 UTC (upper right panel) and 18-00 UTC (lower panel).

Future developments in this MOS system may consist of even more extreme criteria for severe thunderstorms and the inclusion of advected MSG data as a potential predictor source for the 0-6 h projections

of 50 discharges/ 5 min. Figure 4 shows reliability diagrams based on the higher threshold of 100 discharges/ 5 min. The severe thunderstorm forecast system shows the highest skill in the evening (15-21 UTC) with the highest skill for the lowest threshold, as expected. The reliability diagrams for the period July to mid-October 2005 show a better overall skill than the diagrams for the warm half-year of 2006[7]. Factors that may have contributed to the lesser skill in the warm half-year of 2006 are sampling effects, the increased ECMWF model resolution starting February 2006 and/or the low frequencies of severe thunderstorms. Nevertheless, the evaluation of the system by forecasters during the period May 24 2006 to mid-October 2006 was positive[7]. Apparently, a forecast system can be much more useful in practice than the (harsh) objective verification results might suggest. We conclude from the verification results shown here (Figures 3 and 4) that the overall skill of the severe thunderstorm forecast system is reasonable compared to the 2000-2004 climatology, at least for the thresholds of 50 and 100 discharges/ 5 min. Conclusions for the higher threshold of 200 discharges/ 5 min. can only be reached when a dataset with more severe thunderstorm cases will become available. Finally, we would like to stress that the verification results for the independent dataset during the development were good for all thresholds (not shown).

Outlook

The pre-operational KOUW system will be extended to include the 12-48 h projections. Subsequently, this system will replace the operational (severe) thunderstorm forecast system[3]. Future developments in this MOS system may consist of even more extreme criteria for severe thunderstorms[4] and the inclusion of advected MSG data as a potential predictor source for the 0-6 h projections.

1) Siebesma, A.P. and W.C. de Rooy, 2007. *An integral approach for the representation of turbulence, convection and clouds in weather and climate models.* This Biennial Report.
2) Wilks, D.S., 2006. *Statistical methods in the atmospheric sciences, 2nd Ed.*, Academic Press, 627 pp.
3) Schmeits, M.J., C.J. Kok and D.H.P. Vogelezang, 2005. *Probabilistic forecasting of (severe) thunderstorms in the Netherlands using model output statistics.* Weather and Forecasting, **20**, 134-148.
4) Schmeits, M.J., C.J. Kok, D.H.P. Vogelezang and R.M. van Westrhenen. *Probabilistic forecasts of (severe) thunderstorms for the purpose of issuing a weather alarm in the Netherlands.* Submitted to Weather and Forecasting.
5) Wessels, H.R.A., 1998. *Evaluation of a radio interferometry lightning positioning system.* KNMI Scientific Report WR 98-04.
6) Noteboom, S., 2006. *Processing, validatie, en analyse van bliksemdata uit het SAFIR/FLITS systeem.* KNMI Internal Report IR 2006-01 (in Dutch).
7) Schmeits, M.J., C.J. Kok, D.H.P. Vogelezang and R.M. van Westrhenen. *Kansverwachtingen voor onweer ten behoeve van uitgifte weeralarm (KOUW).* KNMI Internal Report IR 2007-03 (in Dutch).

The ESSENCE project – the power of a large model ensemble

Andreas Sterl, Rein Haarsma, Frank Selten, Wilco Hazeleger and Henk Dijkstra (IMAU)

Introduction

The concentration of greenhouse gases in the atmosphere will continue to increase. The resulting trend in climate variables is superimposed on a large natural variability and may be hard to detect. By averaging over an ensemble of model integrations the statistical noise is reduced, and the detection of trends in the noisy weather signal becomes possible even for short time periods (10-20 years) and small regions. At the same time the large amount of data obtained from an ensemble makes it possible to determine weather extremes and their possible change more accurately.

Together with the Institute for Marine and Atmospheric Research of Utrecht University (IMAU) KNMI has performed a follow-up of the successful Challenge project[1] to address these questions. In ESSENCE the ECHAM5/MPI-OM climate model of the Max-Planck-Institute for Meteorology[2] was used because it performed well on a number of criteria during an intercomparison of models[3] that were considered in the IPCC Fourth Assessment Report (AR4). All runs were driven by the A1b scenario of 21st century greenhouse gas concentrations from the IPCC Special Report on Emission Scenarios (SRES). Besides a basic ensemble of 17 runs also three experimental ensembles were performed.

Figure 1 shows the annual-mean 2m-temperature averaged globally (a) and at station De Bilt in the Netherlands (b) for the 17 members of the basic ensemble, together with their mean and the observations (HadCRUT3 dataset[4] for the global-mean, station data for De Bilt). Although the ensemble-spread of the global-mean temperature is fairly small (about 0.4 K), it encompasses the observations very well. Between 1950 and 2005 the observed global-mean temperature increased by 0.65 K, while the ensemble-mean gives an increase of 0.76 K. The discrepancy mainly arises from the period 1950-1965. After that period observed and modelled temperature trends are nearly identical. This gives confidence in the model's sensitivity to changes in GHG concentrations. On the local scale (Figure 1b) the variability is obviously much larger than for global-mean values. This is reflected both in the large spread of the ensemble and in the large year-to-year variability of the observed temperatures. Both spreads are comparable, as are modelled and observed trends.

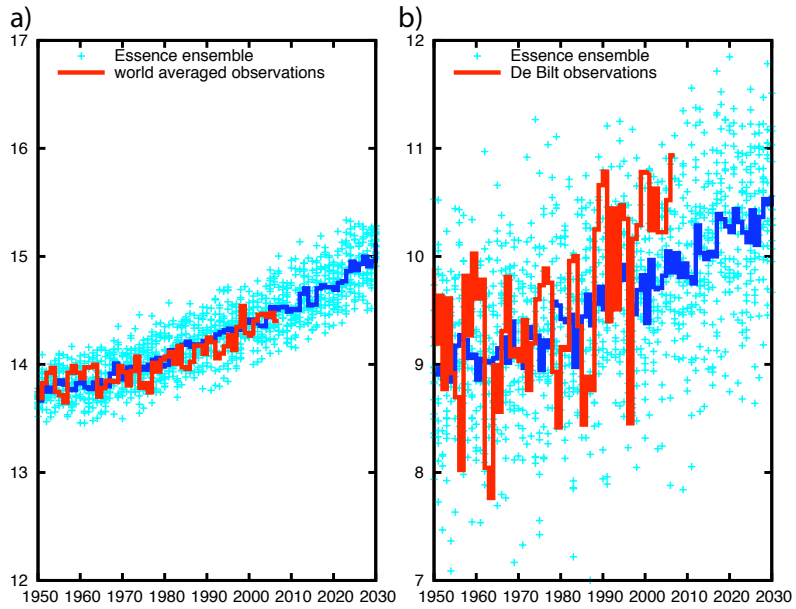

Figure 1. Annual-mean surface temperature for the 17 ensemble members (light blue crosses), their mean (blue line) and observations (red line) for (a) the global average and (b) station De Bilt (the Netherlands).

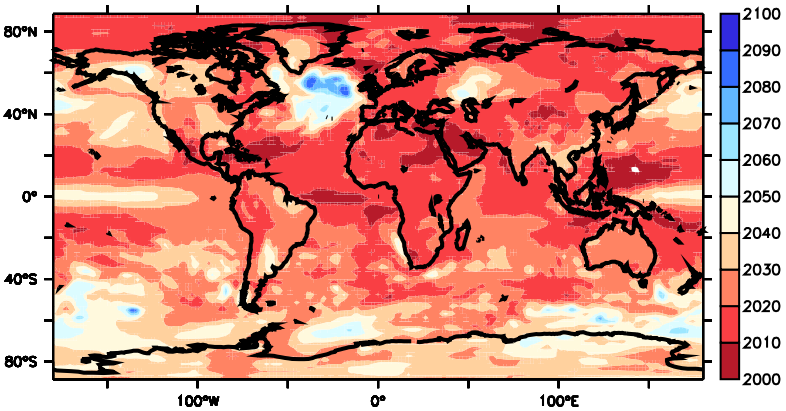

Figure 2. Year in which the trend (measured from 1980 onwards) of the annual-mean 2m-temperature emerges from the weather noise at the 95%-significance level.

Detection of the climate-change signal

The enhanced signal-to-noise ratio that is achieved by averaging over all ensemble members of a large ensemble makes the detection of significant trends over short periods (10-20 years) possible. For near-surface temperature the earliest detection times (Figure 2) are found off the equator in the western

The large amount of data obtained from an ensemble makes it possible to determine weather extremes and their possible change more accurately

parts of the tropical oceans as well as in the Middle East. In these regions the trend is only modest, but the variability is extremely low, so that the signal emerges as early as around 2005 from the noise. A second region with such an early detection time is the Arctic, where the trend is very large due to the decrease of the sea-ice. Over most of Eurasia and Africa detection is possible before 2020. The longest detection times are found in the equatorial Pacific, where, due to El Niño, the variability is very high, as well as in the Southern Ocean and the North Atlantic, where the trend is very small (not shown).
The early detection time of the annual-mean near-surface temperature in the Arctic is mainly due to the decline of the summer sea-ice coverage, which disappears much more rapidly than the winter coverage (Figure 3). During winter it remains cold enough to replace the ice cover that has melted away during summer. While winter ice-cover only reduces in the southernmost parts of the Arctic (like Hudson Bay or Sea of Okhotsk) or at the margins (along East Greenland, Barents Sea), the summer ice cover declines rapidly. About half of the initial volume is already lost around 2020. Sea-ice coverage is halved by about 2050 and declines very rapidly thereafter. The rapid decline in Arctic summer ice-cover is in line with recent model results[5] and observations[6].

Superstorms

Practical questions concerning the construction of river dikes and coastal defence systems require an estimate of the probability of occurrence of extreme high river and sea levels. The coastal defence system should be designed such that the risk of flooding by the sea is once every ten thousand years. Meteorologists are asked what the exact meteorological conditions are that correspond to such a rare flooding event. The problem that meteorologists face is that only relatively short time series of the order of 100 years are available to estimate the one-in-ten-thousand year event from the present climate. Moreover, the probability of this event most likely changes as climate changes.
One therefore has to extrapolate from the relatively few available observations to the one-in-thousand or even one-in-ten-thousand year event. The common approach to solve this problem is to fit a Generalized Extreme Value (GEV) distribution to the observed meteorological extremes (such as wind, precipitation or temperature). The GEV is extrapolated to hitherto unobserved extremes and their return periods are determined. The extrapolation is only allowed if the physical mechanism creating observed and yet unobserved extremes is the same. One way to check this important but in principle improvable assumption is to make use of climate simulations

Over most of Eurasia and Africa detection is possible before 2020

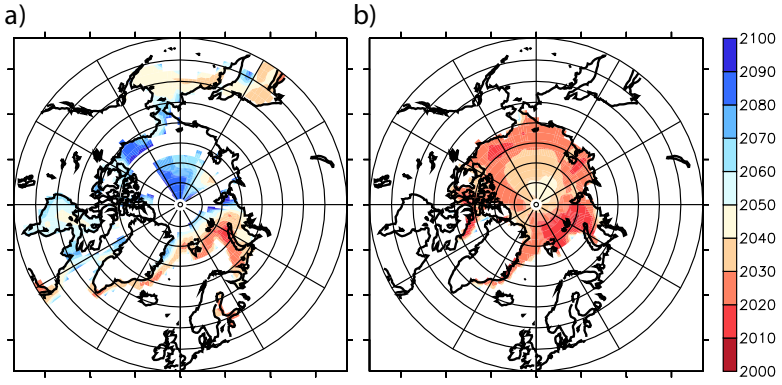

Figure 3. Year in which the trend (measured from 1980 onwards) in (a) March and (b) September sea-ice coverage emerges from the weather noise at the 95%-significance level. In March the trend does not emerge from the noise before 2100 in the white regions in the central Arctic.

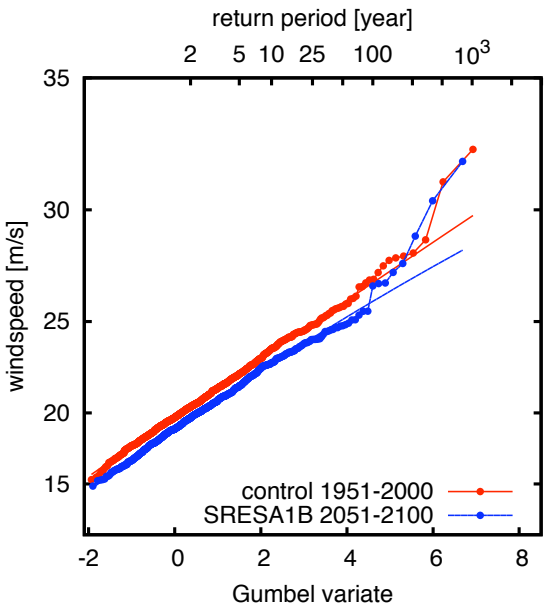

Figure 4. Gumbel plot of the 10m wind extremes for grid point (11°W,36°N), for the current (red) and the future (blue) climate. The thin lines correspond to the fitted GEV distributions.

such as the ESSENCE ensemble. For the period 1951-2000, a total of 37 simulations is available (17 + 20 from a control ensemble), yielding 1850 years of data. For the period 2051-2100, the 17 scenario simulations yield 850 years of data. This is much more than is available from observations.
Figure 4 shows a so-called Gumbel plot for the annual extreme 10-m wind speeds for the grid point (11°W,36°N). The plot shows the annual maxima as a function of the return period; the stronger the extreme, the longer the return period. It shows that the most extreme winds (from return periods of 100 years on) systematically deviate from the theoretical distribution. This suggests that they are formed by a mechanism different from that for the less extreme storms which follow the theoretical distribution. The second mechanism leads to rare, over-extreme winds compared to what we could call 'normal' extremes. While the average of the annual extremes decreases in the future period (the blues curve lies below the red one), the most extreme events do not change, suggesting that the mechanism leading to the over-extreme storms is not affected by climate change.

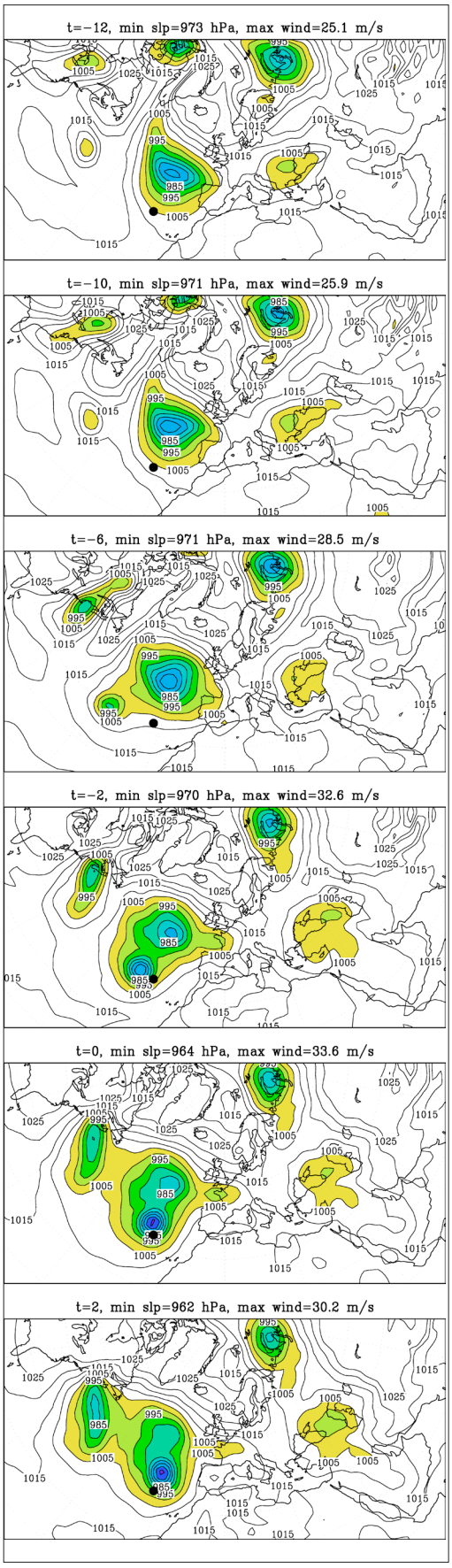

Figure 5. Sea level pressure plots of the storm leading to the most extreme wind speed in the ESSENCE data at the position of the black dot at (11°W,36°N). Values below 1005 hPa are shaded. The time step between the plots is three hours.

Analysis of the over-extreme events suggests an important role for horizontal interaction of cyclones (wave merging). An example is shown in Figure 5. It shows that a cyclone merges with a second one, leading to extremely strong winds, sea-level pressures and deepening rates. Research continues to quantify the effect of merging and detect the geographical regions where this wave merging leads to over-extreme winds. If the interaction is well understood, the mechanism leading to over-extreme storms may be identified in the relatively short record of observational data as well.

Changing wind climate of the Netherlands

In the KNMI Climate Change Scenarios 2006 for The Netherlands[7] a distinction is made between scenarios in which the circulation patterns change (W+ and G+ scenarios) and scenarios with no significant changes in circulation patterns (W and G scenarios). This is based on the observation that the majority of climate models simulate an increase in the westerly flow in winter over Western Europe and an increase in easterly flow during summer[7]. The cautiousness to distinguish between scenarios with and without circulation changes is partly based on the spread in the climate model simulations and partly on the effect of the internal variability of the climate system. Even in an unchanging climate, the atmospheric circulation can vary from decade to decade. This internal climate variability can be estimated from a large ensemble of climate simulations. For the ESSENCE ensemble Figure 6 shows the wind climate in the Netherlands for January and August. For the ensemble mean it shows an increase in westerly flow during winter and an increase in easterly flow during summer, which is in accordance with the conclusions by Van Ulden and Van Oldenborgh[3]. However, the spread between the ensemble members (Figure 6) is so large that for the coming century the climate change signal in the circulation over the Netherlands can be masked by the internal variability of the climate. This underscores the cautiousness being made in the KNMI Climate Change Scenarios 2006 for the Netherlands.

Conclusions and outlook

The examples presented here show the strength of the ensemble approach to distinguish the climate change signal from the weather noise. However, the ESSENCE runs only address one source of uncertainty, namely the one due to internal variability. Another large source of uncertainty stems from the many approximations that are made in the modelling of the physical processes that play a role in the climate system. Examples include the parameterizations of unresolved processes like clouds and small scale turbulent motions and the representation of (biogeo)-chemical processes leading to changes in the atmospheric composition To address these issues we will in the future conduct ensemble experiments with the new EC-EARTH model that is under development, in which we will systematically investigate the impact of uncertainties in the modelling of physical processes on the simulated climate change.

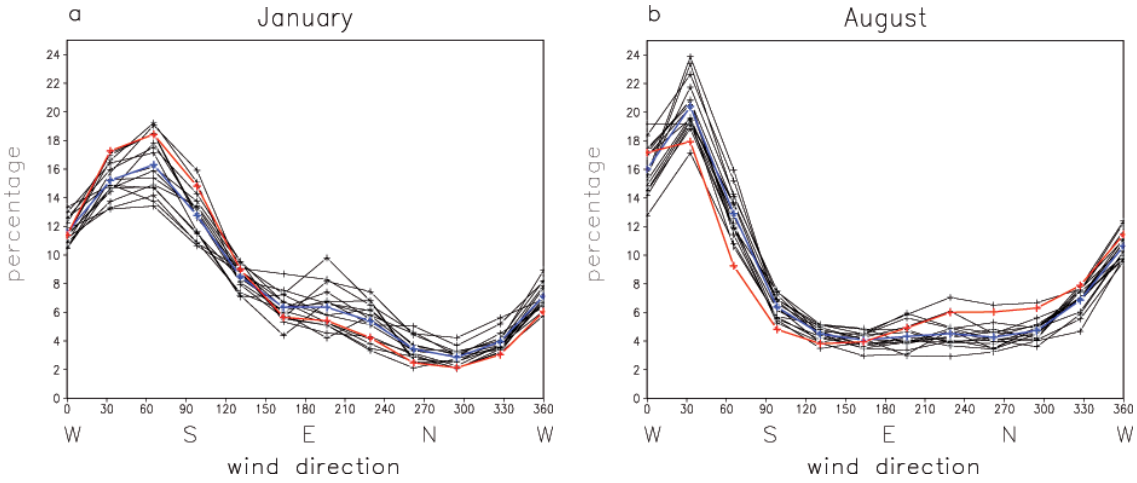

Figure 6. Frequency of the direction of the 10-m-wind in the Netherlands for January (a) and August (b) given as a percentage. The ensemble mean for the period 1971-2000 is indicated by the blue line. The red line gives the ensemble mean for the period 2070-2100. The thin black lines are the individual ensemble members (16) for the period 1971-2000. The results are computed from 3-hourly data.

Acknowledgment: The DEISA-DECI project ESSENCE is lead by Wilco Hazeleger (KNMI) and Henk Dijkstra (UU/IMAU) and was carried out with support of DEISA, HLRS, SARA and NCF (through NCF projects NRG-2006.06, CAVE-06-023 and SG-06-267). The authors thank Camiel Severijns (KNMI), and HLRS and SARA staff for technical support. The Max-Planck-Institute for Meteorology in Hamburg made available their climate model ECHAM5/MPI-OM and provided valuable advice on implementation and use of the model.

1) Selten, F.M., G.W. Branstator, H.A. Dijkstra and M. Kliphuis, 2004. *Tropical origins for recent and future Northern Hemisphere climate change.* Geophys. Res. Lett., **31**, L21205, doi: 10.1029/2004GL020739

2) J. Clim. **19**, 16, *Special Section,* 3769-3987.

3) Ulden, A. van and G.J. van Oldenborgh, 2006. *Large-scale atmospheric circulation biases and changes in global climate model simulations and their importance for climate change in Central Europe.* Atmos. Chem. Phys., **6**, 863-881, SRef-ID: 1680-7324/acp/2006-6-863.

4) Brohan, P., J.J. Kennedy, I. Haris, S.F.B. Tett and P.D. Jones, 2006. *Uncertainty estimates in regional and global observed temperature changes: a new dataset from 1850.* J. Geophys. Res., **111**, D12106. doi:10.1029/2005JD006548

5) Holland, M.M., C.M. Bitz and B. Tremblay , 2006. *Future abrupt reduction in the summer Arctic sea ice.* Geophys. Res. Lett., **33**, L23503. doi: 10.1029/2006GL028024

6) Nghiem, S. V., Y. Chao, G. Neumann, P. Li, D. K. Perovich, T. Street and P. Clemente-Colon, 2006. *Depletion of perennial sea ice in the East Arctic Ocean.* Geophys. Res. Lett., **33**, L17501. doi:10.1029/2006GL027198

7) Hurk, B. van den, A. Klein Tank, G. Lenderink, A. van Ulden, G.J. van Oldenborgh, C. Katsman, H. van den Brink, F. Keller, J. Bessembinder, G. Burgers, G. Komen, W. Hazeleger and S. Drijfhout, 2006. *KNMI Climate Change Scenarios 2006 for The Netherlands.* KNMI Scientific Report WR 2006-01, 82 pp.

Ambient Earth noise and instrumental noise

Reinoud Sleeman

Introduction

The seismic frequency band can be defined from 0.3 mHz to tens or hundreds of Hz, in which the lower limit is defined by the period of the gravest observed free mode of the Earth ($_0S_2$). Digital seismic recordings in this frequency band always contain noise, which essentially can be attributed to ambient Earth noise and instrumental noise, or self-noise, of the recording system. Instrumental noise of today's seismic sensors and high resolution digitizers is usually not considered during the interpretation of seismic data. However, this type of noise may dominate at lower frequencies (e.g. below 0.02 Hz) or at higher frequencies at sites with very low ambient Earth noise levels. In cooperation with Utrecht University (Faculty of Geosciences) KNMI developed a new method to measure instrumental noise in seismic recording systems using ambient Earth noise recordings[1]. This new method extracts self-noise and relative transfer functions of the recording systems from the measurements only, and does not require *a priori* information about the transfer function of each channel. As a consequence the method reveals under which conditions the interpretation of data may be biased by the recording system.

Ambient Earth noise in the Netherlands

Ambient Earth noise, or background noise, is defined as seismic signals in the absence of transient signals from earthquakes. The U.S. Geological Survey New Low Noise Model (NLNM)[2] is often used as reference model for background noise. This model was constructed from a large number of vertical seismograms from many globally distributed seismic stations, and represents the lowermost envelope of a large set of power spectral densities (PSD) of vertical true ground acceleration over the entire seismic frequency band. Essentially, this envelope reflects the minimum seismic noise level which is always expected in seismic recordings. The NLNM model is often used for the purpose of site selection or to compare the quality of seismic sites in terms of noise. Figure 1 displays the probability density functions of the background noise[3] in The Netherlands, recorded at three seismic stations.

New Low Noise Model

Many of the large features of the NLNM are well understood, and the ambient Earth noise sources

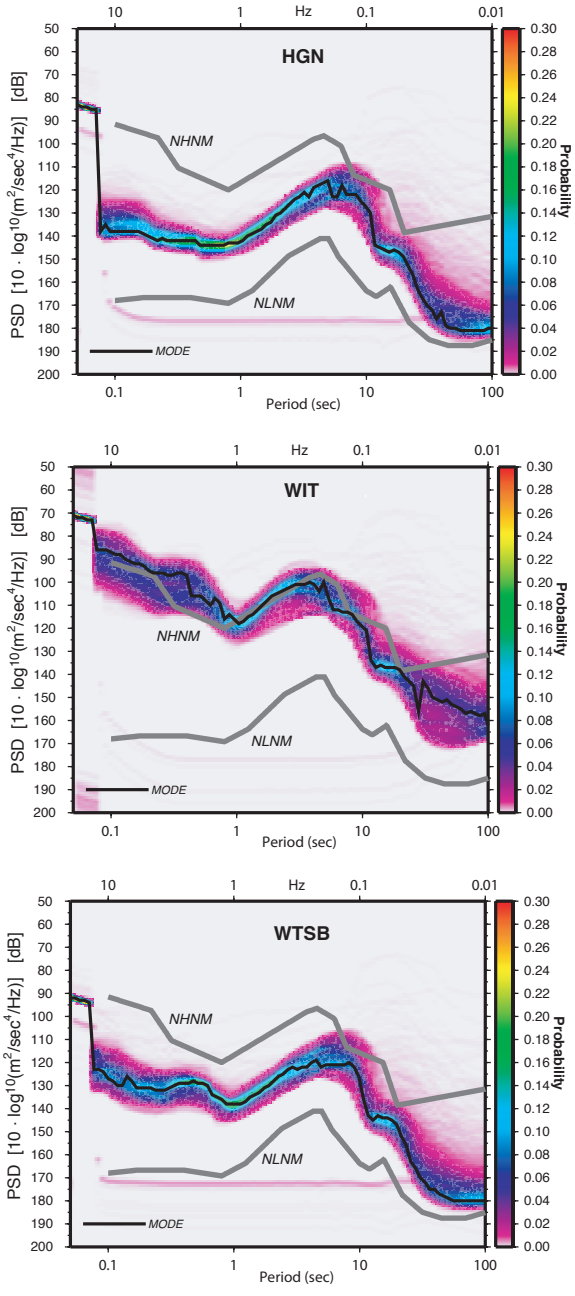

Figure 1. Seismic noise probability density functions at seismic stations Heimansgroeve (HGN), Witteveen (WIT) and Winterswijk (WTSB), measured in 2005. The graphs show the variation of noise at each station as function of frequency, as compared to the USGS low noise model (NLNM) and USGS high noise model (NHNM) with respect to vertical ground acceleration.

may roughly be classified in the frequency domain as follows:

(1) Between 1.10^{-6} and 1.10^{-3} Hz the Newtonian attraction of moving air masses in the local atmosphere above the seismic sensor is the principal source of noise[4]. Tidal frequencies, in particular the tidal constituent M2 due to the Earth rotation relative to the Moon with a period of more than 12 hour, can be measured in this range by very broad band seismic sensors. Also the theoretical, but never observed, Slichter normal mode, which is the translational oscillation of the solid inner core of the Earth around its equilibrium position, has a period in this range.

(2) Between $0{,}3.10^{-3}$ and 30.10^{-3} the noise is not fully understood. In the range between 2 and 7 mHz the noise floor contains spectral peaks whose frequencies coincide with those of the fundamental spheroidal Earth modes. This structure, called 'hum', is a global phenomenon and constitutes a lower bound for observable signals. The 'hum', however, was revealed by stacking the spectra of many seismic recordings as it is slightly below or near the instrumental noise levels of today's seismic sensors[5]. Figure 2 shows that the 'hum' is detected in the Netherlands as well, both in stations HGN and WTSB, which confirms the high quality of these seismic stations in terms of the noise level. The quality has been achieved by careful site selection and installation of the sensors. The origin of the hum is debated but most studies direct towards atmospheric turbulence[6] or ocean waves[7]. Between 7 and 30 mHz the background noise consists of Rayleigh waves, circling around the globe, for which the origin is also not fully understood.

(3) Marine microseisms due to interaction of ocean waves with the ocean floor dominate in the frequency range between 30 mHz and 1 Hz. The sources for these microseisms are recognized in storms at oceans, generating swell- and surf-induced pressure fluctuations at the bottom of the ocean.

(4) Noise at frequencies above 1 Hz is attributed to local random noise (cultural noise) and local atmospheric turbulences. In particular the cultural noise may show strong diurnal variations.

Applications of monitoring of seismic background noise

Not only for site selection purposes the NLNM model is important, but it also has been proven to be useful in seismic network monitoring purposes, e.g. for the Virtual European Broadband Seismograph Network (VEBSN)[8], and in monitoring volcanic activity[9]. Such seismic networks continuously monitor the power spectral density of the background noise and compare these at specific frequencies with the NLNM to detect sudden changes or anomalies. These may, for example, indicate an increase of seismic activity, changes in site conditions or instrumental problems. KNMI seismic stations HGN, WIT and WTSB in The Netherlands, as well as the KNMI seismic stations on the Netherlands Antilles (Saba, St. Eustatius and St. Maarten) are continuously monitored in this way. Figure 3 is an example showing the ambient noise variation in time.

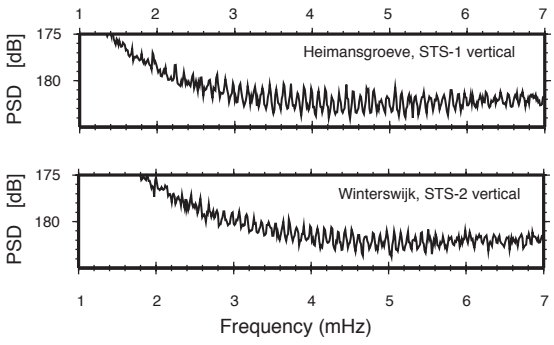

Figure 2. Average power spectral densities of seismic 'noise' at stations HGN and WIT in 2005, after barometric pressure correction. The spectral 'comb' structure is known as the 'hum' and represents the continuous oscillations of the Earth.

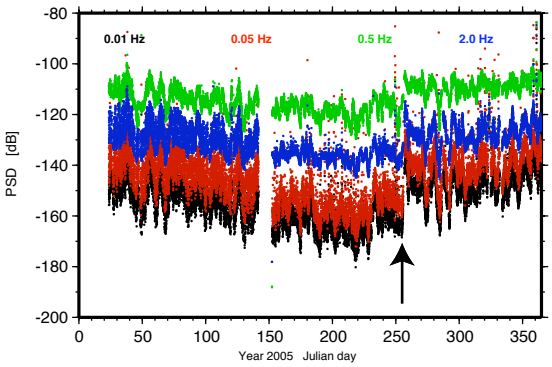

Figure 3. Variation of seismic background noise as function of time at a seismic station. This example illustrates the seasonal variation of the background noise for all frequencies, with lowest noise levels during the northern hemisphere summer. The sudden change in PSD levels around day 250 reflects a change of instrumentation.

Below a few mHz the seismic noise correlates with local barometric pressure variations, mainly due to gravitational attraction by atmospheric masses above the seismic station. Correcting the vertical seismic recordings below a few mHz for atmospheric pressure changes permits the achievement of noise levels even below the NLNM[4,10]), which means that the NLNM may need some minor revision. Also a new analysis technique[11]) applied to recordings from the Global Seismographic Network (GSN) shows noise levels below the NLNM. The interpretation of such low noise data would only makes sense if the noise level of the data is above the noise levels of sensor and digitizer at these low frequencies. It is for these reasons that accurate knowledge or self-noise of the seismic equipment is crucial, and a new technique to estimate instrumental self-noise was developed.

Seismic instrumentation

Broadband and very broadband seismic sensors are used in global, regional and even local seismological studies, because of their wide frequency bandwidth, large dynamic range and low self-noise level. The bandwidth of the sensor specifies the frequency range in which the instrument has a more or less flat response to ground velocity, and may cover more than 4 logarithmic frequency decades. Today's broadband seismometers are of a force balance feedback system to provide a dynamic range up to about 160 dB, to capture signals from ambient Earth noise to earthquakes of magnitude 9.5 at 90 degrees epicentral distance. At low frequencies instrumental noise of today's seismic sensors and dataloggers is of inherent 1/f type of noise, noise whose power spectral density is inversely proportional to frequency. The self-noise for present seismic systems is typically close to the NLNM over an extended bandwidth, from a few hundred seconds to a few Hz, and probably defines the NLNM at low frequencies.

Three-channel correlation analysis

In the conventional approach to estimate the self-noise of linear systems, two systems are used and fed by a common, coherent input signal. This technique has been used in many studies[12]), also to calibrate seismometers[13]), in which two seismometers are placed close together so that it can be assumed they record the same ground motion. The mathematical solution of such a system is very simple, but the practical application is limited because the method assumes that one of the pair of sensors has an accurately known frequency response. Small errors in the transfer functions (or gains) in the two linear systems will cause relatively large errors in the calculated noise levels[14]). Our approach1) uses three linear systems which are also fed by a common input signal. The mathematical solution for this system does not need *a priori* information about the frequency response of each system. The only assumptions are that (1) the self noise between each pair of 2 systems is uncorrelated and (2) the self noise and the input signal are uncorrelated. The mathematical description of the three-channel linear system model shows that we can estimate, solely from the output recordings, (1) the ratio of the transfer functions between the channels and (2) the noise spectrum for each channel. We do not need to know the transfer functions, or its accuracy as is required in the two-channel method.

Digitizer noise level

Figure 4 shows the self-noise of two modern dataloggers, the Quanterra Q4120 and the NARS datalogger. The self-noise was determined with the new technique, using the vertical output of an STS-2 sensor as common input, and compared to the noise level which was measured with closed digitizer inputs. Both digitizers produce some additional noise during the digitizing process of a real input signal, and this disturbance is more pronounced in the NARS datalogger. Both digitizers have a flat noise level at higher frequencies but show a large difference in the dynamic range of about 16 dB. The self-noise levels are above the reference ambient Earth noise level, for frequencies above 1 and 8 Hz respectively, which is too high to record true seismic background noise at the quietest places in the world at high frequencies. Also the frequency at which the 1/f type of noise becomes dominant is different (0.1 Hz for NARS, 0.4 Hz for Q4120), as well as the slope of the 1/f noise. The slope for the Q4120 is modelled with 1/f 1.55 and for the NARS datalogger with 1/f 1.0.

Impact

The new 3-channel correlation technique is a novel, robust and reliable analysis technique to estimate instrumental self-noise, without a priori knowledge of the properties of the instrument. The technique is

The technique is becoming the standard for manufacturers of seismic equipment and major sensor testing projects

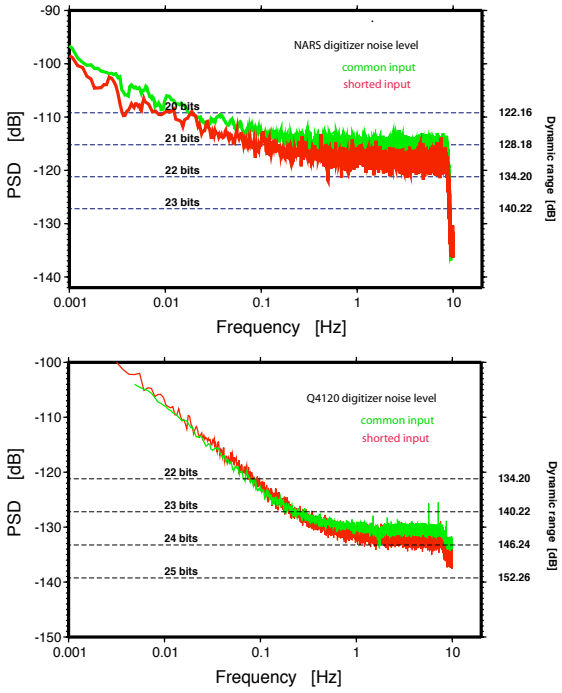

Figure 4. Instrumental noise levels of the NARS data-logger (top) and the Quanterra Q410 datalogger (bottom). The noise floors are measured using short-circuited input recordings (in red) and extracted from recordings of a common input signal from the vertical component of a STS-2 seismic sensor, using the new technique (in green). The left axes represent the resolution of the digitizers in decibels (relative to 1 V²/Hz), and the right axes show the corresponding dynamic range of the system, which has a full-scale input of 40 V. The horizontal, dashed lines show the resolution in bits.

The new method is important as it reveals under which conditions the interpretation of seismic data may be biased by the recording system

becoming the standard for manufacturers of seismic equipment and major sensor testing projects to provide accurate estimates of instrumental self-noise. From a scientific point of view the new method is important as it reveals under which conditions the interpretation of seismic data may be biased by the recording system. It is expected that this technique has to be used in studies towards a revised NLNM as to identify the contribution of instrumental noise to the NLNM.

1) Sleeman, R., A. van Wettum and J. Trampert, 2006. *Three-channel correlation analysis: a new technique to measure instrumental noise of digitizers and seismic sensors.* Bulletin of the Seismological Society of America, **96**, 1, 258-271.
2) Peterson, J., 1993. *Observations and modeling of seismic background noise.* U.S. Geological Survey, Open-File report 93-322, 95 pp.
3) McNamara, D.E. and R.P. Buland, 2004. *Ambient noise levels in the continental United States.* Bulletin of the Seismological Society of America, **94**, 4, 1517-1527.
4) Zürn, W. and R. Widmer, 1995. *On noise reduction in vertical seismic records below 2 mHz using local barometric pressure.* Geophys. Res. Lett., **22**, 3537-3540.
5) Widmer-Schnidrig, R., 2003. *What can superconducting gravimeters contribute to normal-mode seismology?* Bulletin of the Seismological Society of America, **93**, 3, 1370-1380.
6) Rhie, J. and B. Romanowicz, 2004. *Excitation of Earth's continuous free oscillations by atmosphere-ocean-seafloor coupling.* Nature, **431**, 552-555.
7) Webb, S. C., 2007. *The Earth's 'hum' is driven by ocean waves over the continental shelves.* Nature, **445**, 754-756.
8) Sleeman, R and J. Vila, 2007. *Towards an automated quality control manager for the Virtual European Broadband Seismograph Network (VEBSN).* ORFEUS Newsletter, 1. (http://www.orfeus-eu.org/newsletter/vol7no1/ index.htm)

9) Garcia, A., J. Vila, R. Ortiz, R. Macia, R. Sleeman, J.M. Marrero, N. Sanchez, M. Tarraga and A.M. Correig, 2006. *Monitoring the reawakening of Canary Islands' Teide volcano.* EOS, **87**, 6, 61- 65.
10) Beauduin, R, P. Lognonne, J.P. Montagnier, S. Cacho, J.F. Karczewski and M. Morand, 1996. *The effects of the atmospheric pressure changes on seismic signals or how to improve the quality of a station.* Bulletin of the Seismological Society of America, **86**, 6, 1760-1769.
11) Berger, J., P. Davis and G. Ekström, 2004. *Ambient Earth noise: a survey of the global seismographic network.* J. Geophys. Res., **109**, B11307.
12) Holcomb, L. G., 1989. *A direct method for calculating instrument noise levels in side-by-side seismometer evaluations.* U.S. Geological Survey, Open-File report 89-214, 35 pp.
13) Pavlis, G.L. and F.L. Vernon, 1994. *Calibration of seismometers using ground noise.* Bulletin of the Seismological Society of America, **84**, 4, 1243-1255.
14) Holcomb, L.G., 1990. *A numerical study of some potential sources of error in side-by-side seismometer evaluations.* U.S. Geological Survey, Open-File report 90-406, 41 pp.

The Parkfield earthquake prediction experiment

Bernard Dost

Introduction

Earthquake prediction research is based on understanding the long-term behaviour of faults in the earth crust. At this moment, we do have a good knowledge on the location of major active faults in the world, but the time of an event is still hard, if not impossible, to predict. In some cases a fault is showing a series of earthquakes at regular time intervals and similar in size. These are called characteristic earthquakes and are studied in detail.

One example of a characteristic earthquake sequence is a series of earthquakes that happened along the San Andreas fault-system in California, close to the village of Parkfield. In this region three instrumentally recorded earthquakes of magnitude 6 did occur in the 20th century, in 1922, 1934 and 1966, at an average recurrence time of 22 years. Based on these observations and reports of felt earthquakes since 1857, assuming a strictly periodic process and taking the 1934 event as an anomaly, a prediction was issued in 1985 that the next earthquake in this series would occur before 1993[1]. The Parkfield prediction was the only scientific earthquake prediction officially recognized by the United States government[2]. The predicted earthquake finally happened in 2004. Although the timing was wrong, the size of the earthquake was comparable to the earlier event.

The challenge is to find out how well this latest event compares to the previous ones, how characteristic Parkfield events are, and if there are any precursors that can be used in a possible prediction. Local and regional stations, at an epicentral distance < 1000 km, were used to compare the 1934, 1966 and 2004 records. For the 1922 event only very few records can be used. A distinct difference in waveform was observed between the 1934/1966 recordings and the 2004 record[5]. The differences can be explained by details in the rupture process: in the older events it developed from north-west to south-east, in the 2004 event in the opposite direction. Recordings from stations at larger, teleseismic distances are not hampered by these details and are more suitable to compare the general features of the individual earthquakes.

Station DBN

A comparison of the source mechanism and location of the latest event in the Parkfield series with earlier earthquakes requires a well calibrated seismograph station that has continuous recordings over a long period. Preferably, the same type of seismometer should be in operation all the time. Seismograph station DBN (De Bilt, the Netherlands) appears to be the only station outside the US that did record events from 1922, 1934 and 1966 on the same instrument and therefore plays an important role in the Parkfield experiment[1]. The 2004 event was recorded at the same site, but with a different digital instrument.

Seismograph station DBN is in operation since 1908. Most of the analogue data collected since that time are archived and made available on request. Scans of DBN records for selected events are on-line available through the SISMOS project[6]. Different seismographs were in operation over the years, but the most important DBN dataset consists of the continuous archive of seismograms from a set of long period Galitzin seismometers. Two horizontal seismometers are in operation since 1914, the vertical component since 1922. Recording is on photographic paper, three records per day. At the end of 1994, the seismometer was replaced by a digital long period instrument, operating in a broad frequency range that includes the frequency band of the Galitzin.

Waveform comparison

Station DBN recorded on the horizontal components of the Galitzin seismograph the Parkfield earthquakes of 1922, 1934 and 1966. Unfortunately, the vertical component was added a few months after the first event. These recordings, at an epicentral distance of 8900 km, show a striking resemblance, suggesting that the sources should have ruptured the same part of the fault-system. In order to quantify this

These recordings, at an epicentral distance of 8900 km, show a striking resemblance, suggesting that the sources should have ruptured the same part of the fault-system

resemblance, the analogue records were scanned and digitized and the resulting waveforms, including the digital records from the latest 2004 event, were correlated[4]. Since the records show no clear body waves, due to the focal mechanism and shallow depth, but instead well developed surface waves, a new digitization procedure was developed to allow long time series to be accurately sampled. Corrections were made for e.g. the uneven rotation of the recording drum.

The recordings of the 2004 Parkfield earthquake were made on a different type of instrument. Therefore a simulation of the original Galitzin seismometer was required in order to compare waveforms. This process includes a removal of the response of the new seismometer from the recorded time series, followed by a convolution of the resulting signal with the response of the Galitzin seismometer. A set of recursive time-domain filters were designed to implement the simulation.

For a successful simulation we need to have an adequate knowledge of the amplitude and phase characteristics of both the new and old systems. The Galitzin sensor was calibrated on a regular basis between 1914 and 1932 and less regular in the period until 1945. These measurements allow an estimate of the error in the amplitude and phase information. Most important for this study was an estimate of an error of 10% in magnification of the Galitzin. Both old and new seismographs have been described in detail by Dost and Haak[3]. The new seismograph was calibrated a few days after the 2004 earthquake.

Apart from the four Parkfield earthquakes, three additional earthquakes were digitized (Figure 1). These events were selected based on two criteria: a) epicentre from the same region, but with different source characteristics and b) epicentre from the same fault system with the same source characteristics, but outside the Parkfield section. Correlations of the surface wave trains of all these recordings (4 Parkfield and 3 non-Parkfield) show that the horizontal components of the Parkfield events have a normalized correlation coefficient (NCC) > 0.8 and these events can be distinguished from the others that show 0.3<NCC< 0.5[4].

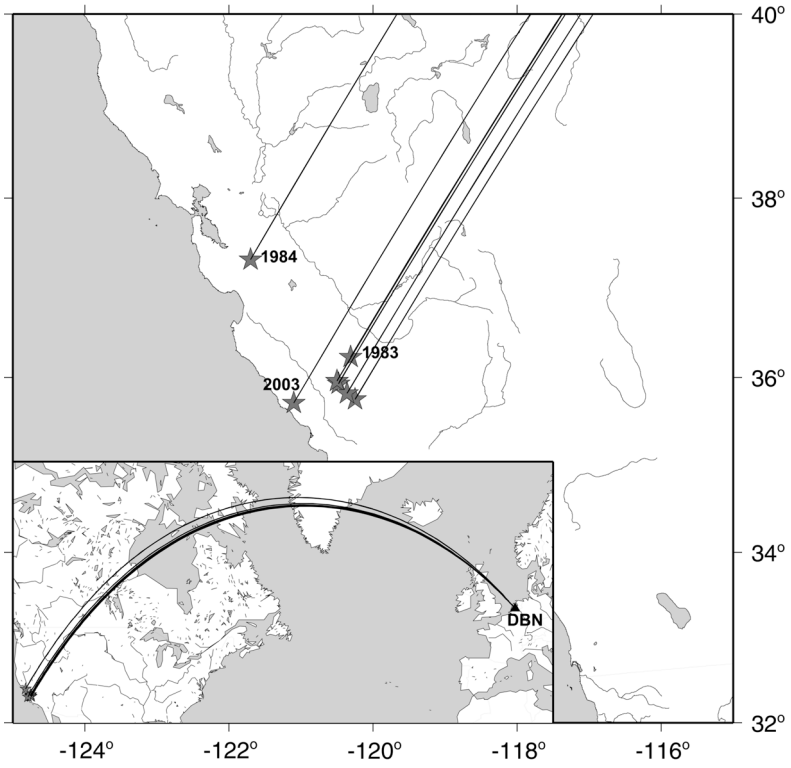

Figure 1. Overview of earthquakes used in the Parkfield study, where non-Parkfield events are marked with their year of occurrence. Great circle paths to station DBN are indicated. (Courtesy Bulletin of the Seismological Society of America)

High normalized correlations imply that the recorded phase information of the surface waves from Parkfield events is similar and therefore that the sources are co-located. From an evaluation of the dominant frequency of the surface waves, a maximum source separation of 10-25km was estimated. Looking at the amplitudes of the events, the conclusion is that the events are similar in size within the accuracy of the calibration (Figure 2). These observations further support the idea of a characteristic earthquake that occurs along the San-Andreas fault-system near Parkfield.

As a spin-off from this research we can better reconstruct the origin time from the oldest 1922 Parkfield event, which is poorly known, due to the high correlation of the recorded waveforms with more recent events. The waveforms we correlate have an average delay of 40 minutes and 1 s with respect to their origin time. For the 1922 event a deviation of 12 s was found and it is suggested to correct the published origin time by the same amount.

Discussion

Understanding the behaviour of seismic activity along an active fault like the San Andreas fault system is a first step towards prediction. The Parkfield experiment shows that even in a situation where a characteristic earthquake occurs around a limited section of a well studied fault, the prediction in time is cumbersome.

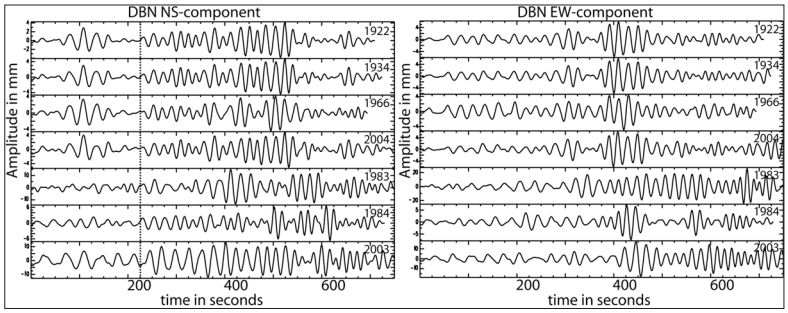

Figure 2. Surface wave records for, from top to bottom, the four Parkfield earthquakes and the three non-Parkfield earthquakes. North-south and east-west components are shown in separate panels. (Courtesy Bulletin of the Seismological Society of America)

Historical archives thus contain valuable information for the assessment of seismic hazard

Speculations on the reasons for this unsuccessful prediction include the effect of several large earthquakes in the neighbourhood, influencing the stress pattern around Parkfield, and the assumptions on the models behind the repeat times[5].

Although the area was intensely monitored, no significant precursors were detected for the 2004 event. Since both the earthquakes of 1934 and 1966 were preceded by a magnitude 5 foreshock at 17 minutes before the mainshock, this is apparently not a characteristic feature of the Parkfield earthquakes.

Conclusion

Since the recurrence times of moderate and large earthquakes along an active fault are usually in the order of at least decades, the use of historical data is essential in unravelling the long term fault behaviour. Digital seismology really started only in the 1980's, while analogue seismic records are available since the end of the 19th century. Historical archives thus contain valuable information for the assessment of seismic hazard. Only recently efforts are taken to coordinate access to these data through the scanning and digitization of the analogue data[6]. Continued long-term monitoring in combination with further development of seismicity models allows the testing of hypotheses and provides further insight into the earthquake generation process.

1) Bakun, W.H. and T.V. McEvilly, 1984. *Recurrence Models and Parkfield, California, Earthquakes.* J. Geophys. Res., **89**, 3051-3058.
2) Bakun, W.H., B. Aagaard, B. Dost, W.L. Ellsworth, J.L. Hardebeck, R.A. Harris, C. Li, M.J.S. Johnston, J. Langbein, J.J. Lienkaemper, A.J. Michael, J.R. Murray, R.M. Nadeau, P.A. Reasenberg, M.S. Reichle, E.A. Roeloffs, A. Shakal, R.W. Simpson and F. Waldhauser, 2005. *Implications for prediction and hazard assessment from the 2004 Parkfield earthquake.* Nature, **437**, 969-974. doi 10.1038/nature04067
3) Dost, B. and H.W. Haak, 2002. *A comprehensive description of the KNMI seismological instrumentation.* KNMI Technical Report TR-245, 60pp.
4) Dost, B. and H.W. Haak, 2006. *Comparing Waveforms by Digitization and Simulation of Waveforms for Four Parkfield Earthquakes Observed in Station DBN, The Netherlands.* Bulletin of the Seismological Society of America, **96**, S50-S55. doi: 10.1785/0120050813
5) Langbein, J., R. Borcherdt, D. Dreger, J. Fletcher, J.L. Hardebeck, M. Hellweg, C. Ji, M. Johnston, J.R. Murray, R. Nadeau, M. J. Rymer and J.A. Treiman, 2005. *Preliminary report on the 28 September 2004, M 6.0 Parkfield, California Earthquake.* Seismol. Res. Lett., **76**, 10-26.
6) Michelini, A., B. De Simoni, A. Amato and E. Boschi, 2005. *Collecting, digitizing, and distributing historical seismological data.* EOS Transactions American Geophysical Union, **86**, 261-266.